Assessing mass change and surface velocity of the debris-covered tongue of the Lirung Glacier, Nepal, over the winter period between October 2013 and May 2014 by means of Unmanned Airborne Vehicle imagery

Name: Fionna Heuff
Student number: 3714861
e-mail address: faw.heuff@gmail.com
Date: February 2015
First supervisor: Dr. Walter Immerzeel
Second supervisor: Prof. Dr. Steven de Jong
Utrecht University,
Faculty of Geosciences,
Department Physical Geography.

Summary

Himalayan glaciers often feature a mantle of supra-glacial debris which greatly influences their dynamics in terms of flow and mass balance. The glaciers are an important source of fresh water, and data on the response of these glaciers to climate change is very valuable (Brown et al., 2010). However in situ research is hampered by inaccessibility of the glaciers due to their remoteness and difficult circumstances for field work caused by the rugged debris covered terrain. Space born remote sensing methods cannot supplement the scarce field data due to generally coarse resolutions or otherwise high monetary costs (Vincent et al., 2013). This provides opportunities for the novel technique using images acquired by Unmanned Aerial Vehicles (UAVs). UAVs can obtain images at a high spatial and temporal resolution, and are therefore very well suited to fill the gap left by field work and space born remote sensing. For this thesis this new method has been applied the debris-covered tongue of the Lirung Glacier, located in the Nepalese Himalaya. Using UAV images acquired in May 2014, an orthorectified mosaic image and Digital Elevation Model (DEM) of part of the glacier tongue were constructed, by means of stereo-imagery and the Structure from Motion algorithm. During processing it became clear that the image dataset was not of optimal condition, but valuable information could still be extracted. Surface feature evolution, surface elevation change, surface velocity, melting and mass balance have been assessed for the winter monsoon period between October 2013 and May 2014. The ortho-mosaic and DEM have been compared to those of May 2013 and October 2013, created by Immerzeel et al. (2014). A difference DEM computed for the period between October 2013 and May 2014 indicated that surface elevation decrease and melt continues during winter, but less than during summer. Supra-glacial ice cliffs were visible as regions of enhanced melt, due to large backwasting rates. By means of manual feature tracking between the ortho-mosaics of May 2014 and October 2013 the surface velocity of the glacier was assessed. This showed homogeneous, slow velocities across mainly the middle and lower part of the glacier tongue. This in contrast to the summer period, which showed a more heterogeneous surface velocity field.

The main finding of this research is that during the winter period the debris-covered tongue of the Lirung Glacier continuous downwasting, but far less change occurs than during the summer period. This is most likely due to the higher temperature and larger amounts of precipitation in the form of rain that occur during the summer monsoon period. It has been shown that UAVs can contribute greatly to the research concerning these type of glaciers, due to their high spatial and temporal scale possibilities. Future research, and obtaining a longer time data set thing can prove of great value to the research into the dynamics of debris-covered glaciers.

Keywords

Unmanned Aerial Vehicle (UAV), debris-covered glacier, Structure from Motion (SfM), ortho-mosaic, Digital Elevation Model (DEM), difference DEM, supra-glacial ice cliff, supra-glacial lake, remote sensing.

Acknowledgements
This thesis has been a very impressive experience for me. It has allowed me to work with new methods of research into glaciers, and remote sensing in general. Also, I have been granted the great opportunity to travel to the research area in Nepal, which has been one of the most impressive experiences in my life. This great venture would not have been possible without Dr. Walter Immerzeel and Prof. Dr. Steven de Jong, my supervisors, and I am very thankful to them. However, I would also like to thank Phd. Candidate Philip Kraaijenbrink, for advice during my thesis research, Dr. Joe Shea and Sander Meijer, for making the field work in Nepal…awesome.

Contents

List of figures, tables and equations

Figures

Tables

Equations

Figures Appendix

I: Difference DEM between October 2013 and May 2013 showing only regions of surface rise or decrease within 1 m *Adapted from Immerzeel et al., 2014).*

J: Difference DEM between October 2013 and May 2013 showing only regions of surface rise or decrease between -1.75m and 1.25 m *(Adapted from: Immerzeel et al. (2014)*

K: Winter difference DEM of entire glacier. Outline of sub-debris ice is outlined in black.

List of acronyms and abbreviations

Amsl	Above mean sea level
ASTER	Advanced Spaceborne Thermal Emission and Reflection Radiometer
BBA	Bundle Block Adjustment
DEM	Digital Elevation Model
ELA	Equilibrium Line Altitude
ENVISAT	Environmental Satellite
InSAR	Interferometric Synthetic Aperture Radar
LANDSAT TM/ETM+	Landsat Thematic Mapper/Enhanced Thematic Mapper +
LiDAR	Light Detection And Ranging
m.w.e	Mean water equivalent
M13	May 2013
M14	May 2014
O13	October 2013
Ortho-mosaic	Orthorectified mosaic image
RaDAR	Radio Detection And Ranging
SAR	Synthetic Aperture Radar
SEB	Surface Energy Balance
SLA	Snow Line Altitude
SPOT	Satellite Pour l'Observation de la Terre
SRTM	Shuttle Radar Topography Mission
UAV	Unmanned Airborne Vehicle

1. Introduction

Glaciers are an important aspect of the world's hydrological cycle. Together with the ice caps they are the largest freshwater reservoir on Earth, supporting one third of the world's population (Brown et al., 2010). In addition, they influence Earth's dynamics both climatologically and hydrologically. Ice and snow cover can exert a substantial influence on climate by interacting with the atmosphere through a range of feedback mechanisms (Hock, 2005).Also, because the glacier mass balance is affected by long term climate changes (in e.g. precipitation or mean temperature) they are considered to be one of the most sensitive climate indicators (Tangborn and Rana, 2000). Hydrologically speaking, glaciers are essential for catchment hydrology; they act as water sources and (temporary) sinks by accumulating freshwater in winter and releasing it in summer and early autumn (Hock, 2005; Bolch et al., 2012). In addition to the influence on freshwater, glacier dynamics can greatly affect sea level. Gardner et al. (2013) computed that meltwater from glaciers worldwide (excluding the Greenland and Antarctic Ice Sheets) accounted for 29±13% of the observed global sea level rise in the period between 2003 and 2009.

About 99% of the world's glacial ice is located in the polar ice caps. However, mountain glaciers are still a key feature of many regions. Especially in the High Asia region glaciers are an important source of freshwater, as this area form the headwaters of the continent's largest rivers (Schaner et al., 2012). The 'High Asia' region includes the Himalayan, Hindu Kush, Karakoram, Pamir and Tien Shan mountain ranges, which all contain extensive glacier areas (figure. 1) (Armstrong, 2010).

The Karakoram-Himalaya is the largest glacierized area besides the Alaska and the Arctic, with a total of about ~40800 km^2 of glaciers (Bolch et al,. 2012), functioning as a freshwater reservoir for 1.3 billion people (Brown et al., 2010). Thus, any change in glaciers dynamics can greatly impact human livelihoods, food security and hydropower potential in this region (Immerzeel et al., 2014). Monitoring of the glaciers in order to assess the condition of this reservoir and its response to climate change is therefore of vital importance (Immerzeel et al., 2010). Already, temperature increase since the Little Ice Age has influenced glaciers greatly, causing a decrease of glacial area and

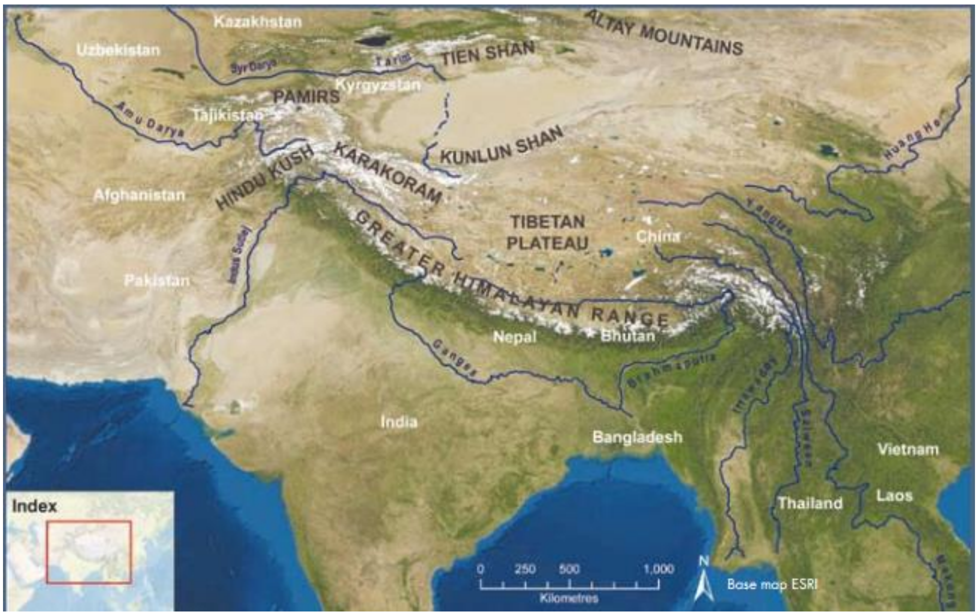

Figure 1: The High Asia region, with concomitant mountain ranges. *Source: Armstrong et al (2010).*

volume. This is particularly true for the glaciers in the monsoon regions of High Asia (Yao et al., 2006). Glaciers in this region appear ideal climate change proxies, since meteorological observations are rather sparse due to the difficulty in acquiring them (Vincent et al., 2013), and these high-altitude, low-latitude glaciers seem to be very sensitive to small temperature changes (Tangborn and Rana, 2000).

Temperature is projected to increase throughout the coming century (Shrestha et al,. 2011). However, there is no consensus about the extent, or how the spatial variability of this temperature increase and indeed any climate change will be (Lutz et al., 2012; Fujita et al., 2011). It was claimed in the AR4 of the IPCC (IPCC, 2007) that Himalayan glaciers would disappear by 2035, but this claim has been proven to be erroneous (Nuimura et al., 2012; Cogley, 2011). There even are indications that certain glaciers in the Karakoram are actually stagnating or even gaining mass (Gardelle et al., 2012; Gardelle et al., 2013). Still, on average, the mass balance of the glaciers in the entire Karakoram-Himalaya region is negative (Gardelle et al., 2013), though the rate at which all the glaciers are retreating is unknown, except for a few exceptions (Nuimura et al., 2012). This debate has exposed major deficiencies in the knowledge of the dynamics of the High Asian glaciers (Bolch et al,. 2012). Annual ice and snow melt, in addition to its seasonal and spatial variability, as well as the contributions of precipitation to discharge are all uncertain (Immerzeel et al., 2010, Bolch et al,. 2012). This knowledge deficiency is mainly caused by lack of in situ (meteorological and glaciological) measurements due to the remoteness of the area and the ruggedness of the terrain (Racoviteanu et al., 2008). Vincent et al. (2013) provided a thorough compilation of all in-situ mass balance series available in western Himalaya. He showed that these series are short-term (usually spanning less than ten years) and discontinuous and are therefore not truly representative of the mass balance of this region (Wagnon et al., 2013; Vincent et al., 2013).

Recent observations to glaciers concern mostly length and area. Unfortunately, these records cannot be used as climate indicator for several reasons, including a time lag in the response of glaciers to climate change (Vincent et al., 2013). Instead, a good way to determine the status of glaciers is by calculating their mass balance. Regrettably this method still suffers from problems in data acquisition. An additional problem is posed by the layer of debris which are a feature of many Himalayan glaciers (Sakai et al., 1998). It covers much of the ablation area, influencing the melt process, while making it difficult to delineate glacier boundaries on remote sensing images. Debris cover influences the radiation balance at the surface; when thick enough, debris can act as an insulating layer that inhibits glacier melt. However, thin layers of debris may actually speed up melting due to its relatively low albedo, causing the debris to absorb heat which is subsequently transported to the sub-debris ice. Since debris is often not uniformly distributed over the glacier surface, heterogeneous patterns of melt rates are produced. In addition, debris covered glaciers often feature supra-glacial ponds and cliffs, which greatly influence ablation and thus melt (Sakai et al., 2002).

There are several methods, including field measurements and remote sensing, to determine glacier dynamics, all with their own advantages and disadvantages (Immerzeel et al., 2014). Remote sensing has the advantage of being a relatively cheap way to cover large areas which might be inaccessible to field campaigns. The images can provide expansive views, in more than just the visible part of the electromagnetic spectrum. However, a major downside is the generally coarse resolution of the obtained imagery, which complicates the study of glacier surface features. In addition, obtaining airborne or spaceborne imagery at high resolution requires thorough planning and might be hindered by bad weather or higher priority missions (Lucieer et al., 2013).

Unmanned Aerial Vehicles (UAVs) may form a solution to these problems. They are cheap, lightweight and easy to deploy and are able to acquire high resolution imagery (1-20 cm), they can fly on demand and can carry multiple sensors (Lucieer et al., 2013). Also, recent advantages in image processing software allows for the generation of highly detailed 3D models of the landscape (Snavely et al., 2008). Immerzeel et al. (2014) have shown that it is indeed possible to monitor large stretches of Himalayan glaciers, relatively quickly and cheaply, with an UAV. They performed two field campaigns on the debris covered Lirung Glacier, located about 100 km north of Kathmandu, Nepal, in May and October 2013. Using the high resolution UAV obtained images they created ortho-mosaics and high resolution digital elevation models (DEMs) of the glacier. These then facilitated accurate assessments of glacier dynamics and surface height changes (Immerzeel et al., 2014). The high-resolution imagery also allowed for studying of the movement of debris and the dynamics of the supra-glacial lakes and ice cliffs (Immerzeel et al., 2014). In May 2014 another field campaign was performed and a new set of images was obtained.

This thesis will continue the study on the debris covered tongue of the Lirung glacier, using the images obtained in May 2014. The goal of this research is two-fold, namely:

- Examine surface features and quantify melt, mass change and surface velocity of part of the glacier tongue over the (winter)monsoon period between October 2013 and May 2014,
- By means of the relatively novel method using images acquired by an UAV.

The evolution of surface features such as supra-glacial ponds and cliffs and their contribution to downwasting will be evaluated. The effects of pre-monsoon (May images) and post-monsoon (October images) conditions on these features will also be assessed.

The findings of this research shall be compared to those from Immerzeel et al. (2014), which covered the summer monsoon between May and October 2013. Any obtained insights will prove to be valuable in future research involving debris-covered glaciers and the use of UAVs in glacier research.

The outline of this thesis will be as follows. First a general introduction into glacier dynamics will provided in chapter 2, followed by a discussion of features and processes that are of general import to Himalayan glaciers. In chapter 3 a summary of the methods (both in situ and remote sensing) employed in past and current research will be provided. Chapter 4 will present the research area and the methods used in this study. Results shall be presented in chapter 5, followed by the discussion and conclusion in chapters 6 and 7 respectively.

2. Glaciers

As stated, glaciers are an important aspect of the world’s hydrological cycle. They provide feedbacks with Earth’s climate and form Earth’s largest exploitable freshwater source.

Glaciers form when there is net accumulation of snow or ice over time (meaning an on-average positive mass-balance). This requires circumstances that allow more snow to accumulate than is able to subsequently melt again. The last time these conditions were met was during the Little Ice Age between the 16^{th} and 19^{th} centuries, and alpine glaciers today are still remnants of that cold period (Sakai et al., 2009). Since then, on average glaciers all around the world are losing mass (Lutz et al., 2012; Gardelle et al., 2013). In this chapter, the theory related to key glaciological processes will be summarized. Firstly, the formation mechanisms and flow dynamics will be discussed. This will be followed by a discussion about glacier mass balance.

2.1 Glacier formation

A glacier is a hard, thick and compact mass of ice on the land surface and moves forward under the influence of gravity and is contained by internal stresses and friction and the base and the sides (Singh et al., 2011; Zemp et al., 2013). Glaciers form over many years through the recrystallization of snow, in areas where more snow accumulates than it melts. They are maintained by this accumulation at high altitudes, and balanced by melting at low altitudes, or calving into lakes or the sea (Singh et al., 2011; Zemp et al., 2013).

The formation of a glacier depends on the transformation of snow into ice. How, and how fast, it occurs depends mainly on temperature (Cuffey and Paterson, 2010). In temperate climates, snow develops into ice much more rapidly than in e.g. the Antarctic, where temperature is subzero throughout the year, because warmer climates allow alternation of periods with melt and refreezing. This temperature induced difference in transformation does not only occur regionally, but also within and on the same glacier itself. So, there can be different formation mechanisms in the same glacier (Cuffey and Paterson, 2010).

The transformation from snow to ice, also called sintering (figure 2.1), depends on the relation between density versus depth. This is controlled by temperature and snow accumulation rate. Temperature controls melting, while accumulation rate influences the amount snow at the surface and hence the pressure on sub-surface material. Generally a division is made between snow, firn and ice. This division is mainly based on density (table 2.1). Snow is the material that has been reasonably unchanged since it fell (Cuffey and Paterson, 2010). Firn is in-between snow and ice; there is no clear division, which only emphasizes the continuous nature of snow transformation. This transformation results from overlying pressure causing the snow crystals to displace, deform and become welded to other particles. The increase in density is a consequence of the disappearance of pore space. The division between firn and ice is obvious; when the interconnecting pores between grains are closed off, around a density of 830 kgm^{-3} , firn has transformed into glacier ice (table 2.1) (Cuffey and Paterson, 2010). A glacier can be subdivided into three main zones (figure 2.2); the accumulation zone, where snow and ice accumulate, the ablation zone, where ice and snow are lost, and the equilibrium line, located on the transition between the former two zones (Marshak, 2008). Accumulation mainly occurs due to snowfall and avalanching from adjacent mountain sides, but also refreezing of meltwater accumulates mass (Cuffey and Paterson, 2010). Ablation occurs due to melting, sublimation, evaporation or calving of ice in a proglacial lake or supra-glacial ponds or lakes (Marshak, 2008). Usually, the equilibrium line is not a distinct “line” but a transition zone where the glacier surface grades from snow, to snow patches, to bare ice(Cuffey and Paterson, 2010). In addition, the equilibrium line altitude (ELA) shifts throughout the season and due to climate change (Benn and Lehmkuhl, 2000).

Table 2.1: Typical densities for snow and ice. *Adapted from: Cuffey and Paterson (2010).*

Material	Density (kgm^{-3})
New snow (immediately after falling in calm conditions)	50-70
Damp new snow	100-200
Settled snow	200-300
Depth hoar	100-300
Wind packed snow	350-400
Firn	400-830
Very wet snow and firn	700-800
Glacier ice	830-923

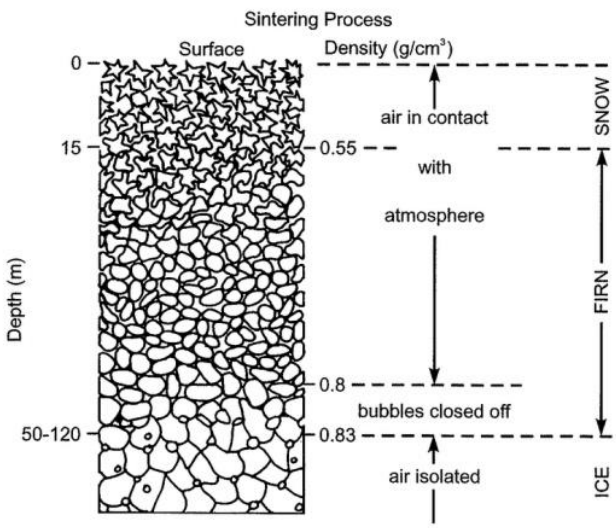

Figure 2.1: The sintering process. *Source: http://www.csa.com/discoveryguides/icecore/ review.php*

The development of glaciers strongly depends on altitude and latitude, for these determine climate and thus temperature, amount and timing of precipitation, humidity, and so on. The timing of precipitation determines whether a glacier accumulates mainly in winter or in summer. In the case of the Hindu Kush-Karakoram-Himalaya region there is great variability in accumulation regimes. In the east the Indian monsoon determines the timing of accumulation. There, the wet period of the monsoon often occurs during summer so these types of glaciers are called summer-accumulation type glaciers (Ageta and Higuchi, 1984). This type of glacier appears most sensitive to climate warming, since an increase in summer-air temperature not only promotes glacier melt, but also considerably reduces accumulation by shifting snowfall to rain (Kääb et al., 2005). In contrast, in the west accumulation occurs mostly in winter due to westerly atmospheric circulations (Kääb et al., 2012).

A more precise description of the features that determine accumulation and ablation processes, and how the interplay between these and accumulation influences mass-balance will be discussed in section 2.3.

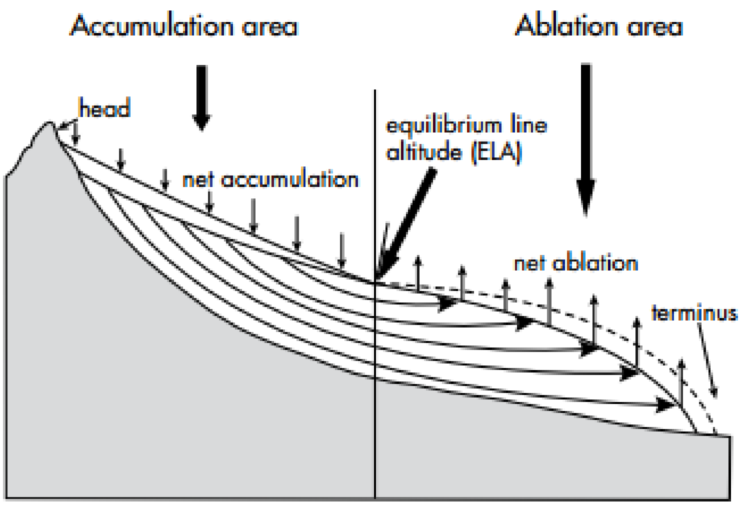

Figure 2.2: Zones of a glacier. Internal flow lines also shown. *Source: Armstrong (2010).*

2.2 Glacier flow

Glacier flow is an important aspect of glaciers, it can 'stretch' a glaciers surface, increasing its surface area or it can cause a piling up of glacier ice. The interplay between glacier flow, accumulation and ablation and therefore glacier mass balance is an important but complicated feature of glaciers. For instance, flow determines distribution of mass over the glacier area, while differences in flow speed may cause extension or compression, leading to surface lowering or elevation.

Glaciers flow due to gravity; they slowly flow down a mountain due to their own weight (figure 2.3). How the glacier subsequently flows is determined by factors influencing the equilibrium of forces within the glacier, such as ablation processes and bed surface slope (Van der Veen, 2013).

Flow can occur in two ways; by basal sliding and/or internal flow (figure 2.4) (Marshak, 2008). Basal sliding is caused by the formation of meltwater at the base, decreasing friction between the bed and the base of the ice and allowing the bottom of the glacier to slide across the surface on the small layer of water. This meltwater may form due to pressure-induced melting of ice, warm air temperatures, or because heat from the Earth below is trapped beneath the insulating ice. Internal flow (or 'creep') entails the movement of a glacier due the mass of ice slowly changing shape internally without breaking apart or completely melting (Marshak, 2008). This flow consists of two processes. The first is the plastic deformation of ice crystals due to the rearrangement of water molecules within the crystal lattice. This process causes ice crystals to change shape or disappear, and new crystals to form. The second process involves the formation of a very thin layer of water on the surface of the ice crystals so they can slide past each other (figure 2.5) (Marshak, 2008). This slow viscous flow not only contributes to overall movement of the glacier, but can also cause closure of tunnels within the ice.

Glaciers generally have flow speeds between 10 and 300 m per year. Yet, not all parts of the glacier move at the same rate (figure 2.6). Basically, the flow velocity at some point of the glacier is controlled by various processes acting from a large region around and within the glacier. Stresses (due to e.g. gravity), ice mass geometry, ice creep properties, bed properties (roughness, slope, etc.) and the amount of meltwater at the base all play a role (Cuffey and Patterson, 2010). Flow lines through a glacier generally follow a concave profile (figure 2.2), and flow usually occurs in a downslope horizontal direction. However vertical flow also occurs (figure 2.4), mainly by internal deformation of the ice, but also by horizontal flow components (Cuffey and Paterson, 2010).

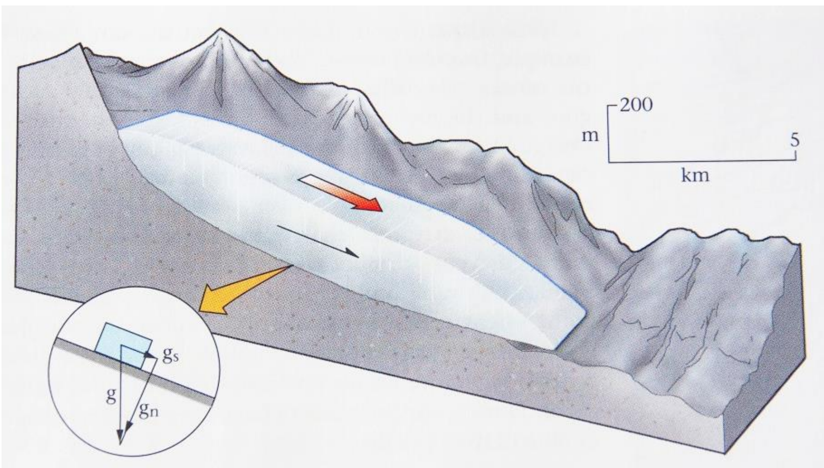

Figure 2.3: Illustration of glacier movement due to gravity. *Source: Marshak (2008).*

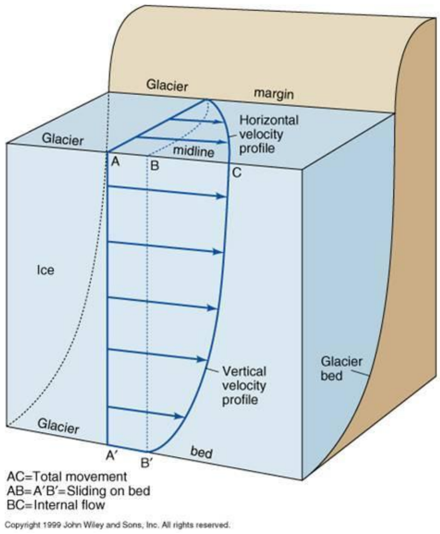

Figure 2.4: Glacier movement due to basal sliding and internal flow. *Source: Marshak (2008).*

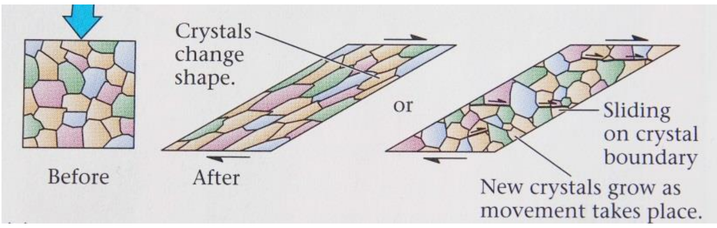

Figure 2.5: Illustration of internal deformation. *Source: Marshak (2008).*

Glaciers may sometimes even flow upslope, since glacier flow direction is chiefly determined by the surface slope of the glacier, and not by the slope of the bed (Van der Veen, 2013). Thus even if the bed slopes upward a glacier can flow across it if the glacier surface slopes downward.

Besides gravity, flow of a glacier is largely caused by the strive for a steady state equilibrium. This is the main cause of an important property of glacier flow, called submergence and emergence velocity (figure 2.7). This refers to the downward or upward flow of ice relative to the glacier surface at a fixed point, due to extension or compression (Cuffey and Paterson, 2010). Where extensive flow causes a decrease in glacier thickness ('stretching'), compressive flow causes a thickness increase. Whether flow is extensive or compressive further depends on flow velocity. In the accumulation zone velocity increases due to steady state equilibrium; the new snow must be transported away, leading to 'extension' in the along-glacier direction. In turn, velocity decreases in the ablation zone to compensate for the ice lost by ablation, which leads to compression and stagnation. The extension in the accumulation zone combined with the strive for steady state equilibrium cause a lowering of the glacier's surface.

Conversely, compression in the ablation zone causes a surface elevation increase (Cuffey and Paterson, 2010). Compression has also been observed in the bend of a glacier, where the flow changes direction and magnitude, compressing the ice which is subsequently pushed upward (Immerzeel et al., 2014). The effect of this upward emergence is that even though a glacier might be losing mass on average, this is not discernable from a corresponding surface lowering. This phenomenon causes difficulties in mass balances estimates which rely on surface elevation differences (Naito et al., 1998; Immerzeel et al., 2014).

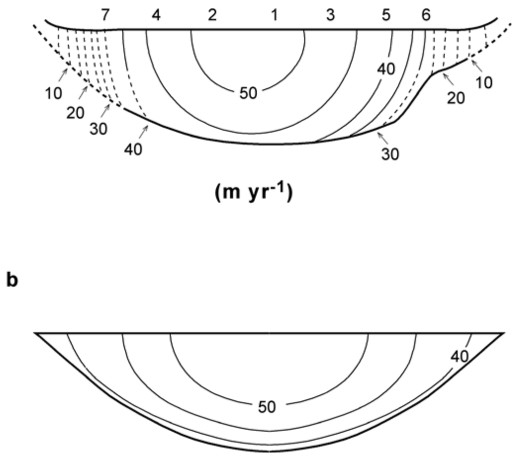

Figure 2.6: Flow velocities within a glacier. *Source: Cuffey and Paterson (2010).*

Climate change can considerably affect glacier flow. Precisely how a glacier responds to climate change is a complicated process, depending on a multitude of factors that all interact and cause positive and negative feedbacks. On top of this, these relationships are non-linear, so small changes in some properties can have large 'runaway' effects (Singh et al., 2011). Changes in mass balance cause volume and thickness changes, which in turn affect glacier flow via internal deformation and basal sliding. This dynamic reaction ultimately leads to alterations in glacier length and area and thickening or thinning of ice (Zemp et al., 2013), which in turn are part of processes influencing mass balance. These processes are not instantaneous: glaciers may lag behind climate change for years. Adjustments in glacier geometry can continue through periods of zero average mass change. Or, conversely, in periods of constant climate glaciers may still experience varying mass balances due to changes in their size and shape (Cuffey and Paterson, 2010).

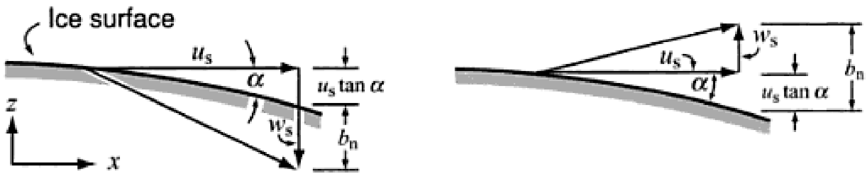

Figure 2.7: Left: submergence velocity. Right: emergence velocity. *Source: Hooke (2005).*

2.3 Glacier mass balance

The relationships between glacier flow, mass and other factors are particularly complicated, making monitoring the response of glaciers to climate change extremely difficult. A commonly employed method in glacier monitoring is to measure glacier length and surface area over a certain span of time. However this is not truly a good indication of the status of a glacier, since glacier tongues often stagnate, especially when they are debris covered, and downwasting (thinning) instead of retreat occurs. This leads to loss of mass without a visible retreat of the glacier (Nuimura et al., 2012; Quincey et al., 2009b). In addition, should one want to asses climate change by observing glacier retreat, length and area are not adequate for direct assessments due to the response time lag to climate, as stated above (Vincent et al., 2013; Cuffey and Patterson, 2010). Instead of length and area, glacier volume and mass balance are more appropriate indicators of glacier status and response to climate change (Bolch et al,. 2011, Vincent et al., 2013).

A glacier's mass balance is defined as the change in total mass of a glacier over time, or the net gain of mass (mass gain minus mass loss). In order to provide some order of magnitude; Gardner et al. (2013) calculated that the average mass budget of the High Asian glaciers, with a total area of around 118200 km^2 is around -220 ± 100 $kgm^{-2}yr^{-1}$, while the global average mass budget (area 506600 km^2) is around -420 ± 50 $kgm^{-2}yr^{-1}$. As was briefly mentioned in section 2.2, glacier mass balance is not something in itself, but a factor in a complex chain of processes that determine glacier dynamics. It is controlled by so called mass exchange processes that either cause the glacier to gain or lose mass, causing periods of positive or negative mass balance respectively. They include interaction with the glacier's environment (the atmosphere, groundwater and the land surface) or interaction between ice and liquid water within the glacier (Cuffey and Paterson, 2010). Common mass gain processes are snowfall and avalanching, and common mass loss processes include melt, sublimation and calving. Mass exchange processes vary with altitude, and the ratio between these processes determines the overall mass balance of the glacier (Cuffey and Paterson, 2010). Mass exchange processes also vary with season, causing mass balance to vary accordingly (Cuffey and Paterson, 2010).

A glacier's mass balance is not the same across the entire glacier, but an average of all mass balances of specific locations on the glacier. These are the specific mass balances, defined as mass change per unit area (kgm^{-2}) (Cuffey and Paterson, 2010). Consider figure 2.8. Ice flows from location A to location B. X is a vertical column of mass between these two zones. The mass balance of this column is the specific mass balance, and it is determined by mass exchange processes at the surface, bottom and within the glacier (the surface, subglacial and englacial balances), and by flow through the column. In a glacier many of these columns may be pictured and each likely has a slightly different specific mass balance, the clearest difference occurring between the accumulation and ablation zones, with average positive and negative balances respectively (Cuffey and Paterson, 2010).

The total mass balance of the glacier is then the summation of mass balances, integrated over the surface area of the glacier Should the total mass of a glacier be M ($kgm^{-2}yr^{-1}$), the mass change rate is given by:

$$\frac{dM}{dt} = \int_A (b_s + b_b + b_e)dA - B_c \qquad (1)$$

Here, b_s, b_b and b_e ($kgm^{-2}yr^{-1}$) represent the surface, basal and englacial balance respectively. The plan view area (top view of a horizontal section) of the glacier is given by dA, and B_c is the addition of mass loss per unit time due to calving. When integrated over an interval of time, Equation 1 gives the glacier mass balance (ΔM) (Cuffey and Paterson, 2010). In many cases, the surface balance

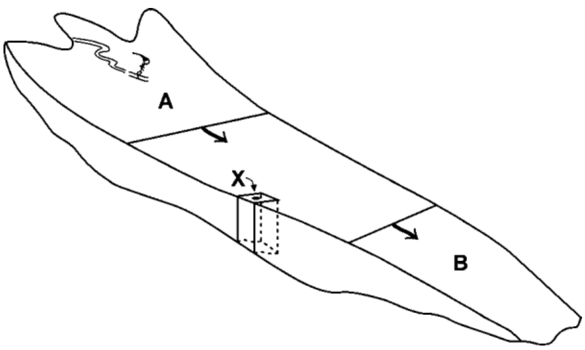

Figure 2.8: Specific mass balance illustration. *Source: Cuffey and Paterson (2010).*

component so dominant that the englacial and basal balances may be neglected, considerably simplifying equation 1 (Cuffey and Paterson, 2010).

The interaction between specific balances determines the overall dynamics of the glacier, (Cuffey and Paterson, 2010). As stated in section 1, mass balance calculations are important tools in climate research concerning glaciers. The relations and feedbacks between climate and a glacier are summarized in figure 2.9 (Cuffey and Paterson, 2010). For clarity the figure is split into an upper and lower part. The average conditions over a large area (such as a mountain range) make up the regional climate and the local climate applies to the glacier itself and its immediate surroundings. Local climate controls supply and loss of mass and heat at the glacier surface, thereby determining specific balance. Total mass balance is then determined by the summed total of specific balances relative to the surface area of the glacier, in addition to calving effects at the margin of the glacier. The mass balance, glacier area and climate continuously interact during these processes. Clearly these feedback effects are very important in the glacier mass balance processes (Cuffey and Paterson, 2010). The lower panel signifies the effect of ice flow, featuring another important feedback; the interplay between the specific balances controls and glaciers shape and size. Changes in thickness and size ultimately determine whether a glacier advances or retreats (Cuffey and Paterson, 2010).

Specific or total mass balances are not a constant, fixed figure but often fluctuate with an annual cycle (Cuffey and Paterson, 2010). In figure 2.10 the seasonal cycle as it is present on most glaciers is depicted. As stated in section 2.1, glaciers usually gain mass in winter and lose it in summer, due to the variations in temperature and (type of) precipitation. However, in the Himalaya region the annual variation in mass balance is due to the alternation of wet and dry (monsoonal) seasons. Still, the trend in figure 2.10 will basically be the same.

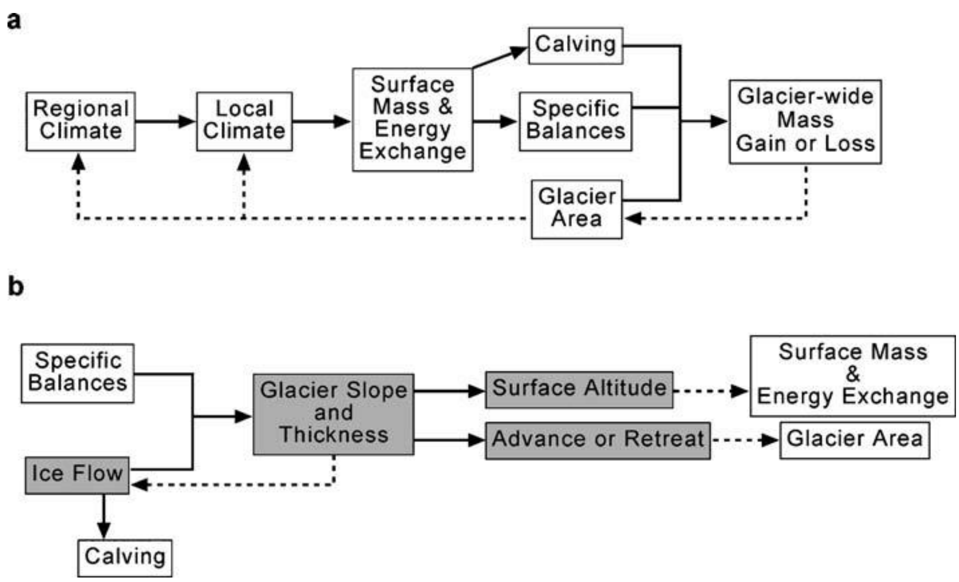

Figure 2.9: Schematic representation of the relation between climate, (a) glaciers and (b) glacier flow. Feedbacks are denoted by dotted lines. *Source: Cuffey and Patterson (2010).*

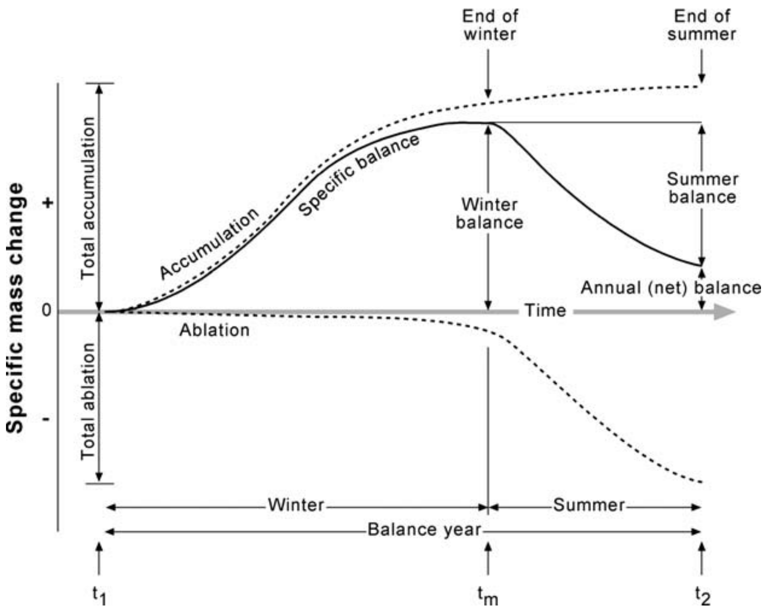

Figure 2.10: Accumulation and ablation during one year, thus constituting the annual balance. Note that the curves have idealized smoothness for clarity. *Source: Cuffey and Patterson (2010).*

Of course, climate change on long timescales also affect glaciers and mass balance, but with a delayed response (Vincent et al., 2013; Cuffey and Paterson, 2010). Basically, a glacier's mass balance at a point is the direct and undelayed signal of annual atmospheric conditions, while glacier advance or retreat composes the indirect, delayed and integrated response to climate change (Zemp et al., 2013).

2.3.1 Surface mass balance

As stated above, often the dominant mass exchange processes occur at glacier surface. The main processes that constitute the surface balance (b_s) are snowfall (a_s), avalanche deposition (a_a) , melt (m_s), refreezing of water (a_r), sublimation (s) and wind deposition (a_w) (Equation 2) (Cuffey and Paterson, 2010). The latter two may be positive or negative.

$$b_s = a_s + a_a - m_s + a_r - s + a_w \quad (2)$$

Snowfall and melt, which depend on climate and radiation effects, are commonly the dominant processes determining the balance. Climate determines air temperature and the amount and type of precipitation, while radiation determines the glacier surface energy balance (SEB) (Cuffey and Paterson, 2010). The radiation balance is likely the most influential of all factors involved: it largely determines the temperature anywhere near and on the glacier's surface.

Accumulation

As stated, accumulation mainly occurs due to snowfall. This in turn is governed by climate, atmospheric circulation and orographic effects. For some mountain glaciers avalanches from cirque headwalls or steep valley slopes can also be an important source for accumulation. These avalanches can cause very localized region of positive mass balance along the sides and head of the glacier (Benn and Lehmkuhl, 2000). The exact contributions are unknown due to the dangers involved in researching avalanches (Benn and Lehmkuhl, 2000). Specific mass balances are also influenced by the (re)deposition of wind. The removal of mass at one location and deposition at another may alter specific balances, while a glacier´s total mass balance remains the same. In addition, wind can cause turbulent fluxes at the glacier's surface, affecting the fluxes of heat and vapor between the surface and the air (Hagg et al., 2008). This will be further discussed below.

Surface ablation

Mass loss of a glacier primarily occurs due to four processes: 1) melting of clean ice, 2) melting of ice beneath a debris cover, 3) melting of ice cliffs and calving around margins of supra-glacial ponds and 4) calving into deep proglacial lakes (Benn et al., 2012).

Mountain glaciers ablate mostly by melt and evaporation. However, in dry conditions, sublimation can also play a substantial role (Hagg et al., 2008). These processes are basically controlled by sunlight and the atmosphere's heat content, which determine the net flux of energy from the atmosphere to the surface (the SEB) (Cuffey and Paterson, 2010). The general form of a glacier (elevation, aspect, slope), its surface characteristics (e.g. albedo) and the climatic and meteorological conditions all play a role in glacier ablation. Not only do they directly affect it, but they also affect the sensitivity of ablation to warming (Cuffey and Paterson, 2010). A debris cover complicates the surface balance even more by introducing factors such as its thickness, surface temperature and thermal conductivity, which in turn are influenced by the albedo, density and moisture conditions of the debris layer (Hagg et al., 2008). All these aspects will be considered in section 4. Energy from geothermal fluxes could have some influence on ablation, but this effect is minimal and is not considered here in detail (Hagg et al., 2008).

Important processes of energy transfer between the surface and the atmosphere are fluxes of radiation and of sensible and latent heat. The latter two are controlled by turbulent mixing of heat and vapor occurring in the air close to the glacier's surface (figure 2.11) (Hagg et al., 2008; Cuffey and Paterson, 2010).

The SEB per unit area (or the net energy flux into the surface, E_n) can be depicted as follows;

$$E_N = \underbrace{E_{Si} + E_{So} + E_{Li} + E_{lo}}_{E_R} + E_g + E_H + E_E + E_P \tag{3}$$

Here, E_r is the net radiation flux, with incoming and outgoing shortwave and longwave radiation ($E_{si,}$ E_{So}, E_{Li} and E_{lo}) as its components. E_p and E_g are the precipitation and geothermal heat flux respectively. As stated, the latter usually is not significant. E_h and E_e are sensible and latent heat transfers (Cuffey and Paterson, 2010). These transfers occur due to vertical mixing of air adjacent to the glacier's surface, with that of overlying, often warmer, air. This causes a sensible heat transfer towards the surface. In addition, if overlying air is drier than the surface air (which is saturated with respect to vapor), moisture is transferred to the overlying air. To maintain saturation the glacier surface must evaporate or sublimate, which consumes latent heat. In general, these fluxes can be positive or negative. The latent heat flux in equation 3 only refers to heat associated with vapor. This means heat consumption by evaporation and sublimation and release by condensation and deposition. Latent heat associated with melt and refreeze of water is already incorporated in the factor E_n (Cuffey and Paterson, 2010).

Of the above factors, shortwave radiation is the major energy source and thus a key factor for glacier melt (Hagg et al., 2008). It is mainly controlled by surface albedo, for this determines the reflectivity of the surface. Albedo can vary greatly across the surface of the glacier (Cuffey and Paterson, 2010). It may decrease by debris or by a small layer of meltwater, but a fresh layer of snow

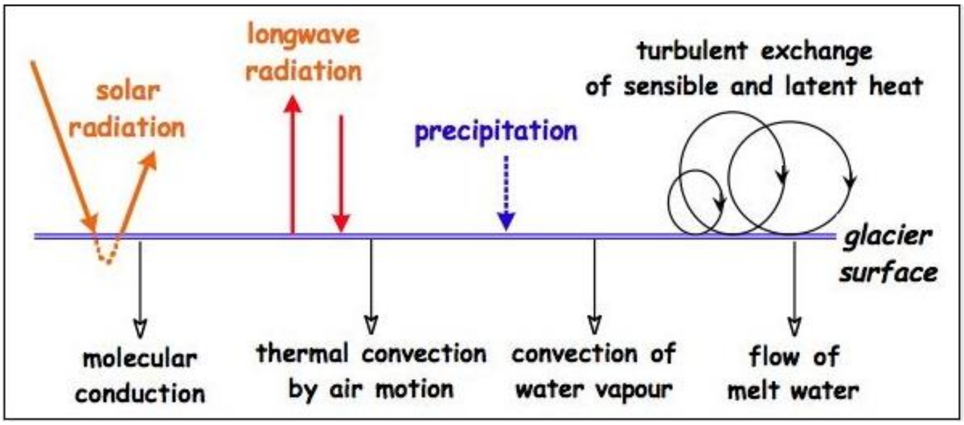

Figure 2.11: Surface energy balance processes. *Source: http://www.staff.science.uu.nl/~oerle102/site_Mort/menu_4.html*

can cause a considerable increase. Absorption or reflection of (shortwave) radiation also depends on the angle of incidence. So, glacier aspect and slope but also the time of day have a substantial influence. The latter means that reflectivity of the surface may change during the course of the day. This is especially important for supra-glacial cliffs, since their surfaces are oriented in one general direction (Sakai et al., 2002). Shortwave radiation incidence is also influenced by altitude and latitude; it increases with decreasing latitude, but increasing altitude. So, the low-latitude, high-altitude Himalayan glaciers receive relatively much shortwave radiation. Also meteorological conditions and surrounding topography can play a substantial role, as clouds and mountaintops can block incoming radiation and create substantial shadow effects. Shortwave radiation then reaches the surface of the glacier only diffusely (Han et al., 2010).

The outgoing longwave and sensible and latent heat fluxes are dependent on temperature (Reid and Brock, 2010). Longwave radiation flux is mainly determined by the temperature of the surface, while the sensible and latent heat fluxes are also driven air temperature (Cuffey and Paterson, 2010). Sublimation is promoted by three factors; dry air, a warm surface and strong winds. It can be a large energy sink because in dry periods it consumes most of the energy supplied by net radiation and sensible heat, but is a very ineffective ablation mechanism. The latent heat of sublimation is 8.5 times greater than that of melting (Cuffey and Paterson, 2010), meaning 8.5 times less ice can be ablated with the same amount of energy input. Evaporation can also considerably reduce ablation rates. Firstly, it favors the formation of small ice needles, thereby increasing the albedo of the surface relative to situations where condensation occurs (Hagg et al., 2008). In addition, the energy that is used for evaporation is no longer available to melt ice. Moreover, like sublimation, this is a very ineffective use of energy because evaporation consumes seven times as much energy as melting (Hagg et al., 2008).

In summary, mainly two factors provide energy for a melting glacier: sunlight and the atmosphere's heat content (Cuffey and Paterson, 2010). The latter is made up of downward longwave radiation and the sensible heat flux, while the former constitutes downward shortwave radiation. While the energy flow towards the glacier keeps the surface at the same 'warm' temperature as the overlying atmosphere, at the same time the glacier is constantly returning energy back to its surroundings (Cuffey and Paterson, 2010). The amount of longwave radiation emitted depends on the temperature of the surface, while albedo determines the reflected shortwave radiation. In addition to these main fluxes, heat (and thus energy) is lot from the glacier by evaporation and sublimation into dry air and sometimes by an actual sensible heat transfer into cold air by turbulent fluxes. Lastly, there is some heat flow from the surface into the ice or back by conduction (Cuffey and Paterson, 2010).

2.4 Debris covered glaciers

In the Everest region, defined to include all peaks and ridges on the border between Nepal and Tibet, between the Tama Kosi basin, the Dudh Kosi basin and the Arun river basin (figure 2.12), contains 1930 km^2 of glacier ice and permanent snow, of which about 23% is covered by debris (Benn et al., 2012). Due to the various effects of debris cover, it's impact on glacier response to climate change can also vary and thus is subject of much research (Benn et al., 2012; Bolch et al., 2012). It is stated by several authors that supra-glacial debris causes glaciers to respond differently to climate change than clean glaciers, by changing surface ablation rates and spatial patterns of mass loss (Benn et al., 2012; Bolch et al., 2012; Juen et al., 2013). For instance, debris-covered glaciers have a melt rate sensitivity to temperature of about four times less than clean-ice glaciers (Brock et al. 2010). Due to varying debris thickness and distributions, debris covers can also cause different dynamics between glaciers in the same region, or even between different parts of the same glacier (Fujita and Nuimura, 2011).

Supra-glacial debris comes in various shapes and sizes (figure 2.13). It can originate from various sources, such as sporadic rock falls or landslides, melt-out of englacial debris bands, meltwater bursts through the crevasse and conduit system or aeolian deposition directly on top of the glacier's surface (Juen et al,. 2013). The debris subsequently is transported along with glacier flow (Vincent et al., 2013).

The effect that a layer of supra-glacial debris has on ablation depends on various factors, compounded on those that determine ablation on clean ice (section 2.3.1). The primary reason that supra-glacial debris has such an influence on ablation is because of its impact on the SEB (figure 2.14) (Benn et al., 2012). Due to its (relatively) low albedo it absorbs much more shortwave radiation than ice, allowing higher surface temperatures than on clean ice. Debris surface temperature therefore is

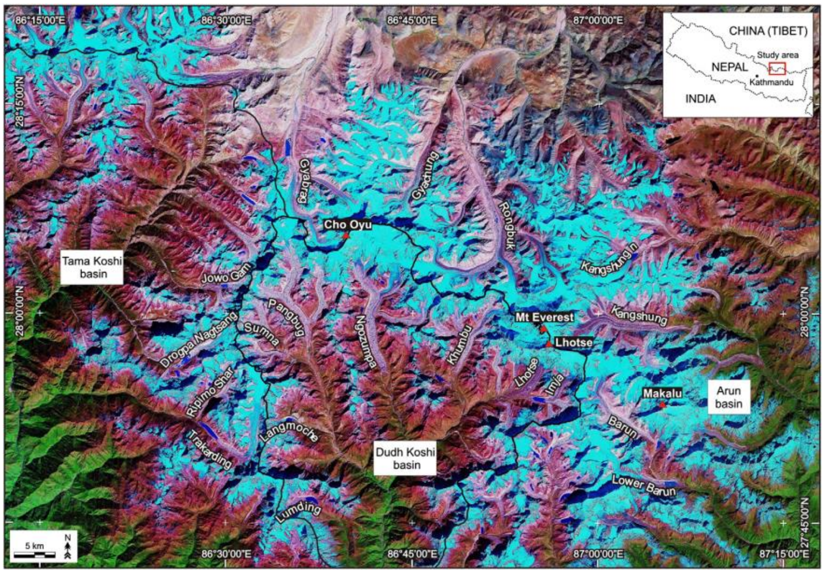

Figure 2.12: The Everest Region. *Source: Benn et al. (2012).*

an important factor to consider in glacier studies. It determines the heat loss by longwave radiation, influences sensible heat and conduction through the layer and it affects latent heat through its influence on surface vapor pressure (Benn et al., 2012). This excess heat has to be transported to the ice before it can affect ablation.

Heat absorption and conduction through the ice-debris interface are mainly controlled by physical properties of the debris (e.g. lithology) and the thickness of the layer (Mihalcea et al., 2006: Vincent et al., 2013). Often a debris layer consists of different types of lithology, sometimes in a patchy distribution, causing complex patterns of melting on the glacier's surface. Thermal conductivity determines the heat flux through the debris layer. According to Mihalcea et al. (2006) and Kayastha et al. (2000), this flux is proportional to the inverse thermal resistance(m^2°CW^{-1}) of this layer for a given surface temperature:

$$Q_C = \frac{T_S}{R} \tag{4}$$

With Q_C the heat flux through the debris layer (Wm^{-2}), T_s debris surface temperature relative to 0°C and R the effective thermal resistance (m^2°CW^{-1}) through the layer. Effective thermal resistance is controlled by lithology, but also by the porosity of the debris layer, moisture content within the cover and especially debris thickness (Kayastha et al., 2000; Sakai et al., 2004; Mihalcea et al., 2006).

The amount of sub-debris ice ablation using the energy available from the heat flux is given by:

$$a = \frac{Q_C}{L\rho} \tag{5}$$

With a the rate of ablation in thickness (m/s), L the latent heat of phase change of ice (334 x10^3 J/kg) and ρ the density of ice (~900 kg/m^3) (Kayastha et al., 2000).

Figure 2.13: Supra-glacial debris of various sizes, around a supra-glacial pond. *Source: http://www.swisseduc.ch/glaciers/glossary/ supra-glacial-debris-en.html*

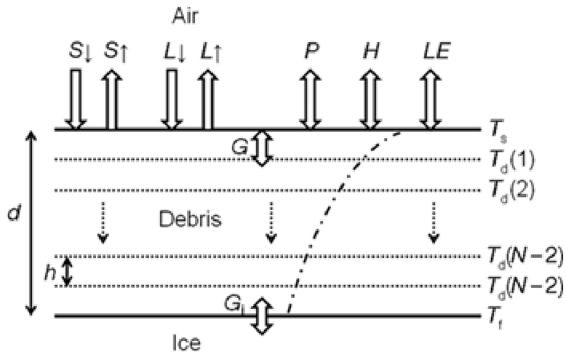

Figure 2.14: Debris surface energy balance processes. S=shortwave radiation, L= longwave radiation, P= heat flux due to precipitation, H= sensible heat flux, LE= latent heat flux, G= geothermal heat flux. T=temperature. Dotted line represents temperature profile, with decreasing temperature from right to left. *Source: Benn et al.(2012).*

Effective thermal resistance of a debris layer increases with increasing layer thickness (Mihalcea et al., 2006), since any incoming energy is first used to heat the debris and only afterwards becomes available for sub-debris melt by convection (Rana et al., 1996). Since the debris cools down at night, this lag occurs every day and ultimately causes a great reduction of total ablation compared to clean-ice glaciers (Reznichenko et al., 2010). However, in the case of a very thin layer of debris or small single grains, extra heat provided by the debris is transferred to the underlying ice rapidly enough, increasing ablation rates. Thus, there is a 'critical thickness' of debris, defined as the thickness at which sub-debris ablation of ice equals that of adjacent bare ice and above which sub-debris melt rates are reduced (figure 2.15) (Östrem, 1959; Reznichenko et al., 2010). In addition, debris layer thickness plays a part in the outgoing longwave radiation and sensible heat fluxes. Debris temperature rise causes a corresponding increase in outgoing longwave radiation and sensible heat fluxes, up to a point that for a certain thickness (the critical thickness) they cancel out the incoming shortwave radiation flux and thereby also suppress sub-debris ablation (figure 2.16) (Reid et al., 2012).Critical thickness varies with location and time, for it is dependent on the diurnal cyclicity of incoming radiation and temperature, in turn determined by altitude and latitude, and season (Reznichenko et al., 2010). Basically, critical thickness increases linearly with increasing average solar radiation input rate. Amplitudes of diurnal cycles decreases with increasing latitude, and also daily average temperature. However, with increasing elevation the diurnal amplitude increases due to enhanced outward radiation, and corresponding lower temperatures at night. These lower nightly temperatures enhance the lag-insulation effect explained above, leading to an increase in energy needed to commence heat percolation through the debris layer, and thus the onset of ablation, the next day (Reznichenko et al., 2010).

Maximum ablation does not occur at the thinnest possible layer of debris, for then the sub-debris ice can reflect more shortwave radiation which is then unavailable for melt. So, in addition to a critical thickness, there is an 'effective' debris thickness, at which maximum ablation occurs (Rana et al., 1996). Reid et al. (2012) state that very thin layers of debris are unlikely to cover large surfaces. Instead thin layers are likely to occur in a patchy way, only locally affecting melt.

The above well illustrates the importance of radiation on sub-debris ablation. However, as stated, also the moisture conditions within the debris can influence heat conduction and melt. Any percolating water can affect the heat flux through the debris layer itself and thus modify the melt rate at the ice-surface (Reznichenko et al., 2010). Melt can by directly impacted by the heat flux accompanying the water, but also by the latent heat flux associated with evaporation (Sakai et al.,

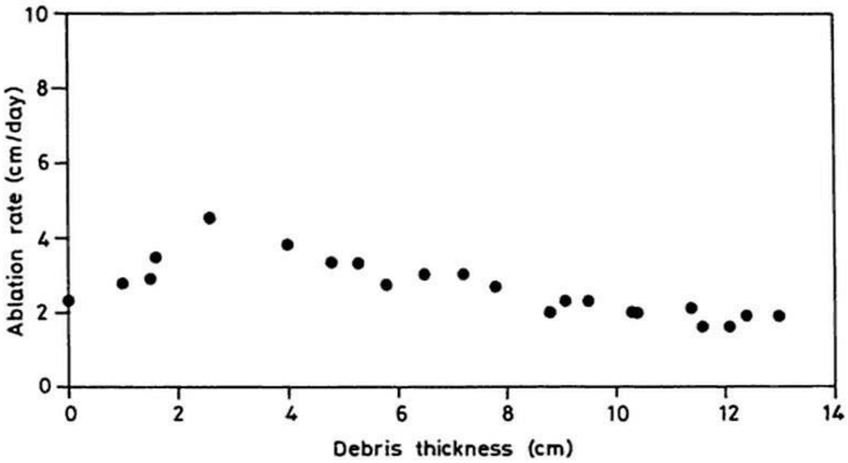

Figure 2.15: Illustration of Östrem-curve; ablation rates under different debris cover thicknesses. *Source: Singh and Singh (2001).*

2004). Sakai et al. (2004) state that if rain is taken into consideration in ablation calculations, one should also include the heat flux due to evaporation, which takes up heat. If one does not, melt amounts under the debris layer will be estimated twice as high as they actually are (Sakai et al., 2004).

2.4.1 Supra-glacial lakes and cliffs

In addition to the mass-balance complexities presented by the debris layer itself, the often accompanying supra-glacial lakes and ice cliffs add even more to the equation (figure 2.17). As stated, they are widely recognized as spots of enhanced melting (Sakai et al., 2002). The steeply inclined ice cliffs are often covered by a very thin layer of dust or sand, increasing absorption of shortwave radiation due the relatively low albedo (Juen et al., 2013, Sakai et al., 2002). Supra-glacial lakes contribute to glacier ablation by uncovering ice, thereby enlarging the area that is susceptible to rapid melting (Röhl, 2008). Also, since water absorbs relatively much heat, it greatly enhances ablation on the glacier surface (figure 2.18).

Figure 2.17: Supra-glacial lake and accompanying (low-albedo) ice cliff on Lirung Glacier.

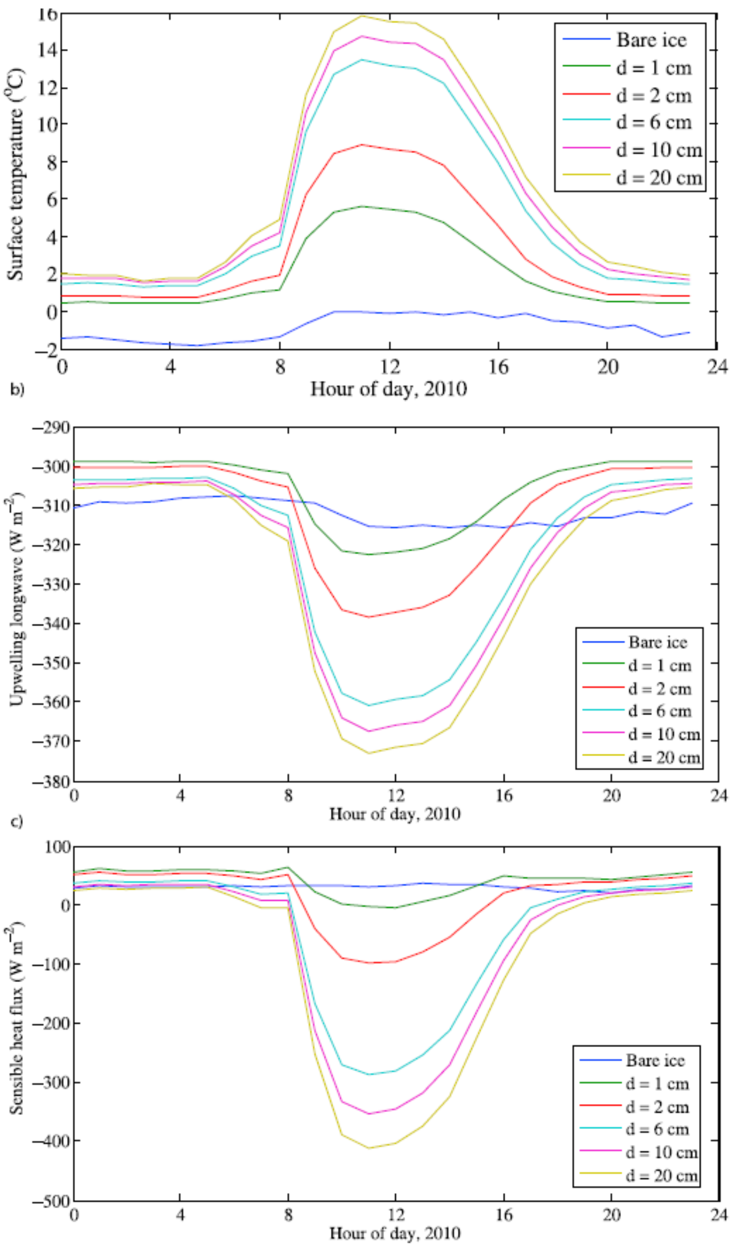

Figure 2.16: Illustration of effect of debris cover on longwave and sensible heat fluxes. Negative fluxes correspond to energy lost to the atmosphere *Source: Reid et al. (2012).*

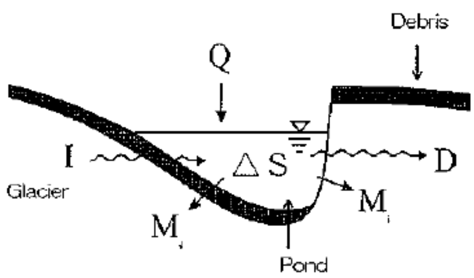

Figure 2.18: Schematic representation of the heat balance at a supra-glacial pond. Q= net heat input at water surface, ΔS= the change in heat storage of the pond, I= heat by meltwater inflow, Md= latent heat of fusion for ice melt under the debris layer at the pond bottom, Mi= latent heat of fusion for subaqueous ice melt at the cliff, and D= the heat released by outflow. *Source: Sakai et al. (2000).*

Lakes

Lakes may form in depression occurring on low sloped glacier tongues that experience rapid lowering of their surface and have enough meltwater available to form water bodies (Sakai and Fujita, 2010: Reynolds, 2000). When water pools in such a depression it may begin to thaw the ice beneath, eventually creating ponds or ultimately lakes. There are two types of lakes possible: perched lakes and so-called base level lakes (figure 2.19). Perched lakes have no connection with the sub-glacial drainage system, while base level lakes do. Also, perched lakes can only grow to a limited extent, while base-level lakes may grow progressively (Röhl, 2008). Even though perched lakes have no connection with the englacial drainage system, they can still occasionally drain, when a connection does form (Reynolds, 2000) (figure 2.20). This may occur due to continued subaqeous melting eventually leading to a breach of the lake bottom. Alternatively, glacier dynamics can cause opening of crevasses through which the lake water can flow away (Röhl, 2008). Himalayan glaciers feature complex flow dynamics, thus surface structures are likely to open and close intermittently, allowing drainage of surface water into the glacier (Reynolds, 2000). This leads to internal ablation in the englacial conduit system, causing a positive feedback process, as the collapse of the water channels creates new lakes and ice cliffs (Sakai et al., 2000). Further sustainment of the lakes depends on the hydraulic connection to the englacial drainage system, which is in turn influenced by the position of englacial conduits and supra-glacial topography (Röhl, 2008). Many lakes in the Himalayas are perched lakes, and therefore ephemeral features, periodically draining (Reynolds, 2000).

Supra-glacial water bodies can grow by means of several processes: 1) subaerial melting, 2) water-line melting and 3) calving from the lake-cliff (Benn et al., 2001). Subaerial melting occurs on the exposed ice slopes around the lake margin. In the initial evolution of lakes, this may be the most dominant process (Röhl, 2008). Water-line melting occurs due to the advection of warm surface water by wind-generated currents. Calving may occur due to thermal erosion, or due to stresses induced by glacier flow (Röhl, 2008). Commonly small chips of ice flake from the cliff, but large blocks can also be detached due to pre-existing fractures or due to undercutting of the cliff by water line melting (Benn et al., 2001). A more rare form of calving is subaqueous calving, entailing the detachment and buoyant rise of blocks of ice from the lake bottom (Benn et al., 2001).

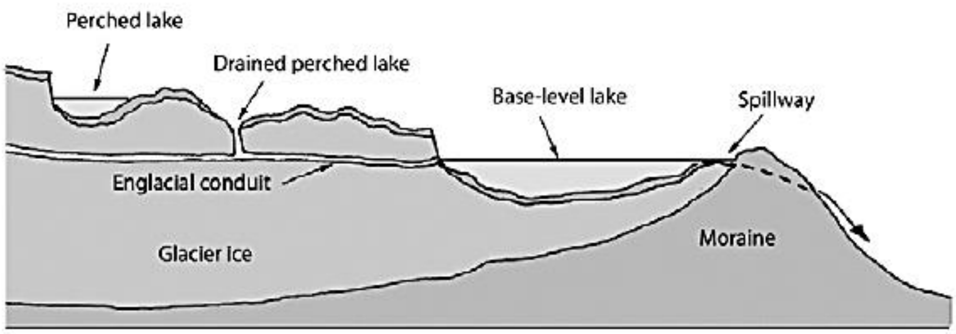

Figure 2.19: Schematic representation of perched and base-level lakes. *Source: Benn et al. (2012).*

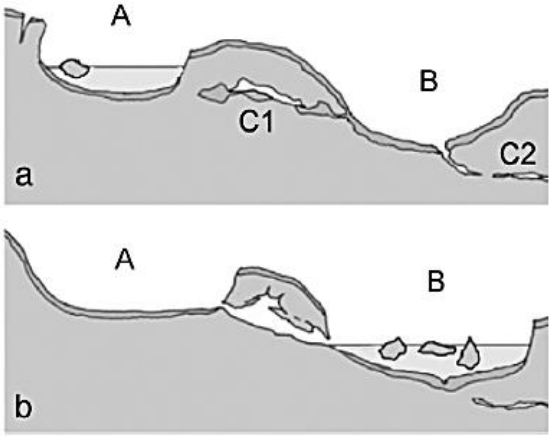

Figure 2.20: Schematic representation of perched lake drainage. a) Lake B is drained through conduit C2 while lake A is underlain by intact ice. b) Ice-cliff retreat (towards the right) has brought Lake A into contact with Lake B through reactivated conduit C1. Conduit C2 has been become blocked, thus retaining water in Lake B, where ice-cliff retreat is now occurring instead of in Lake A. *Source: Benn et al. (2012****).***

Cliffs

The cliffs surrounding supra-glacial lakes also have a considerable influence on surface ablation (Sakai et al., 2000; Reid et al., 2013; Juen et al., 2013). A study on Lirung Glacier (Sakai et al., 1998) indicates that while they only constitute 2% of the total area, 69% of total melt originates from ice cliffs. Also on Lirung Glacier, Immerzeel et al. (2014) observed that 24% of the total melt was generated by lakes and associated cliffs, while it constituted only 8% of the total monitored area. When estimating ablation on the glacier, ignoring the contribution of ice cliff erosion would result in a 20% underestimation of total debris area ablation (Sakai et al., 2002).

Bare ice cliffs form where the surface slope exceeds the angle of friction of the debris (Reid et al,. 2013). There are three ways in which cliffs can form. Firstly, ice may become exposed by the slumping of debris of slopes. Second, englacial voids may collapse, creating a cliff. Thirdly, calving into a supra-glacial lake due to thermal erosion at the side-walls may form cliffs (Benn et al., 2012; Reid et al., 2013; Sakai et al., 2002)

Once they are formed, the development of an ice cliff mainly depends on its initial slope and aspect angles, the backslope (i.e. the glacier surface slope behind the cliff), and the surrounding topography (Reid et al., 2013). The backslope determines whether a cliff will grow or shrink during backwasting while topography, slope and aspect control the patterns of energy received across, and thereby ablation on, the face of the cliff (Reid et al., 2013). This has important consequences for the further evolution of ice cliffs, for they change their slope angle based on the heat available for melting (Sakai et al., 2002).

The main ice loss process from cliffs is melt, in addition to the occasional calving (Röhl, 2008). Melt is in turn influenced by the energy balance at the face of the cliff. Haidong et al. (2010) found that the net shortwave radiation is the main contributor of energy, constituting 76% of total heat available for ice melt. This radiation consist of direct sunlight, and diffuse radiation from the atmosphere and surrounding topography. The secondary contributor to melting is the sensible heat flux (24%). The latent heat and longwave radiation fluxes are not as important, but on cold days heat loss due to longwave radiation may be substantial (Haidong et al., 2010). Diffusive atmospheric radiation contributes considerably to total shortwave radiation incident on the ice cliff, making up around half of the total incident radiation (Haidong et al., 2010). Still, direct shortwave radiation (sunlight) is crucial, as it not just drives melt, but also influences cliff development. Since northward facing cliffs receive almost no direct shortwave radiation, they suffer far less ablation than southward facing cliffs. Also, north facing cliffs have a larger area and a steeper slope than the angle of repose (figure 2.21) (Sakai et al., 2002). Therefore these cliffs cannot be covered by melt-enhancing debris, and they tend to stay stable. In contrast, southward facing cliffs are small in area and have low slope angles and hence are covered by debris, and tend to disappear (Sakai et al., 2002). The slope a cliff has depends on the difference in melt rate between the upper and lower parts of the cliff: gentle slopes form when the top-part melt rate is higher than the bottom part (Sakai et al., 2002). Since southward facing cliffs receive direct sunlight at the top part while the bottom part is partly shaded by the opposite cliff top and debris (figure 2.22), they experience most melt at their top, leading to 'gentling' slopes. These gentler slopes receive even more shortwave radiation, continuing this positive feedback loop until ultimately the cliff disappears (Sakai et al., 2002). The debris on this slope emits longwave radiation to the bottom of the opposite (northward facing) cliff. Since these cliffs receive relatively little shortwave radiation at their top most melt occurs at the bottom portion of the slope. Thus, these cliffs become steep and may persist (Sakai et al., 2002). Still, southward facing cliffs may also be maintained should the debris cover become a protective, insulating cover (Reid et al., 2013).

Even though ice cliff albedo and slope are the most important factors, meteorological conditions can also affect cliff ablation. For instance, during the monsoon season, the weather is always cloudy during the afternoon (Sakai, 1998), blocking radiation incident on northwestern cliffs. Also, wind (especially when combined with thermal undercutting due to water convection in lakes) can be of influence (Reid et al., 2013; Sakai et al., 2009). Additionally, the fact that sun-warmed debris raises ambient air temperature through convection means that the more southward facing cliffs are present, the higher the air temperature and thus the more melt occurs (Reid et al., 2013). The exact contribution of all these factors to ice cliff evolution and therefore glacier ablation is unknown, requiring more research, preferably at high spatial resolution and over long timescales (Reid et al., 2013).

In conclusion, ice cliff melt contributes to total melt and is mainly determined pattern of incident radiation. This is chiefly determined by cliff orientation and albedo, but also by surrounding topography and meteorological conditions.

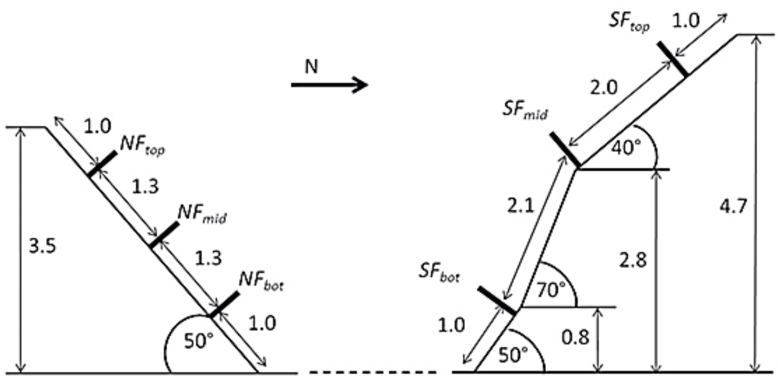

Figure 2.21: Difference between northward (left) and southward facing cliffs. *Source: Reid et al. (2013).*

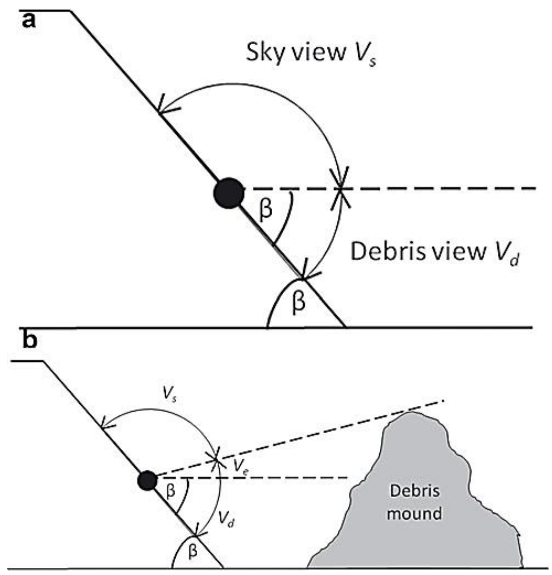

Figure 2.22: Effect of debris shading on incident radiation. *Source: Reid et al. (2013).*

Based on the above, it is clear that debris introduces many complications in an already complex ablation process (Reid et al., 2010). The effects of debris are only compounded on the 'normal' factors determining melt. Any effects that it has in turn depend on more variables, such as its lithology, thickness and pattern across the glacier's surface. Therefore the exact contribution of debris to ablation varies between glaciers and different parts of the same glacier. This is further complicated by the presence of lakes and cliffs. It is known that they cause an increase in glacier ablation, but research with higher spatial resolution and longer timescales is needed to better understand the exact nature of this process (Reid et al., 2013).

An additional aspect of debris, noticed by Reid et al. (2012), is the effect of sparse debris cover with scattered rocks and pebbles. Large boulders create shadow effects and thus suppress ablation. Small rocks on the other hand do not, and are simply heated up by shortwave radiation which causes them to melt into the underlying ice. The exact effects of this sparse debris cover are unsure (Reid et al., 2012). A debris cover also influences the entire shape of a glacier. Stagnation of the tongue occurs while the upper part of the glacier still flows. This leads to a concave-upward profile, with sometimes even the toe of the glacier having a higher elevation than somewhere up-glacier, causing the debris tongue to be partly disconnected from the accumulation area (Quincey et al., 2009b, Shea et al., 2013). Consequently, the glacier loses mass by surface lowering instead of horizontal retreat (Quincey et al., 2009b). Additional complications arise due to emergence (or submergence) velocity. For instance, if a glacier is losing mass on average, emergence might cause an increase in the glacier's surface. This will hinder any geodetic measurements of mass balance, which use surface elevation change as a measure for mass loss or gain (Immerzeel et al., 2014).

2.5 Conclusion

From the above it has become clear that glaciers and their associated features are very complex features of any (mountainous) environment. A glacier's ice ablation, mass balance and flow are influenced by many environmental factors, and are connected through various feedbacks. The above described energy balance processes are very intricate and difficult to study in any research concerning glacier dynamics. Therefore, the exact workings of the processes are still largely unknown. Supra-glacial debris with it accompanying lakes and cliffs add even more complexities to the energy and mass balances. When thick enough, the debris itself suppresses ablation rates. However the existence of supra-glacial lakes and cliffs in turn increase ablation. Gardelle et al. (2013) state that perhaps the decrease in ablation due to debris is actually partly offset by the increased melt by lakes and cliffs. This all causes research concerning the dynamics of debris-covered glaciers to be very difficult.

Still, general information about glacier dynamics can still be inferred, such as total mass balance and glacier flow velocity. There are various ways to approach this, mainly involving remote sensing, which will be discussed in the following chapter.

3. Researching glacier dynamics

Several techniques have been and are employed in research concerning glacier dynamics. These methods may be subdivided into field methods and remote sensing. Field methods include hydrological and glaciological measurements, while remote sensing methods include geodetic research and glacier mapping. In the following sections these field and remote sensing methods shall be discussed.

3.1 Field methods

Hydrological methods use precipitation and outlet discharge measurements that are corrected for runoff and evaporation to estimate the mass balance (Immerzeel et al., 2014). This technique is difficult to employ in remote areas such as the Himalaya because of the lack of accurate precipitation and runoff measurements (Bolch et al., 2012; Immerzeel et al., 2012; Gardelle, 2013).

Glaciological measurement techniques use readings from a network of ablation stakes that have been drilled into the glacier and of which the distance between the top and bottom is repeatedly measured. In addition, accumulation amounts are measured in accumulation pits and snow pillows in order to determine the mass loss or gain of the glacier surface (Immerzeel et al., 2014). The local mass balance can subsequently be calculated and interpolated over the glacier surface by using measured or estimated snow and ice densities (Immerzeel et al., 2014). Data of the surface velocity field of the glacier is collected by quantifying the displacement of the stakes, using differential GPS. Field measurement techniques often generate high-resolution data, but on a small scale. Thus they are best used for examining local effects. The inaccessibility of glaciers makes the acquiring the data a very time consuming and expensive effort in remote areas (Immerzeel et al., 2014). This causes field measurements to often be relatively short term (Gardelle et al., 2013). Additionally, supra-glacial debris hinders field measurement techniques due to the roughness of the terrain, leading to only a few locations with melt information. Melt rates vary considerably across a glacier, making it virtually impossible to generate a high enough drilling density to capture this heterogeneity in melt rates (Immerzeel et al., 2014). Also, field based mass balances of several years have to be available for this method, making it difficult to apply in remote areas such as the Himalaya.

Due to the abovementioned issues, glaciological research by means of remote sensing is a good alternative to increase the amount and type of monitored glaciers (Gardelle et al., 2013).

3.2 Remote sensing

Surface velocity, mass balance or its components (accumulation and ablation) cannot be directly measured from space. In contrast, parameters which may be used to estimate these can be obtained by means of remote sensing (Racoviteanu et al., 2008). Remote sensing methods applied to infer information about velocity or glacier dimension changes use data sets, obtained from at least two points in time, of either active or passive spaceborne or airborne remote sensing systems (Immerzeel et al. 2014). There are two general approaches: glacier mapping and geodetic techniques. Glacier mapping is basically the determining of areal extent (in particular terminus advance or retreat) and other surface characteristics of a glacier and is perhaps the most common method to obtain (indirect) estimates of glacier dynamics. Data about the surface of glaciers may be obtained by means of optical imagery, using algorithms and band ratios based on the spectral differences between snow, ice and other glacial features (figure 3.1).

The geodetic approach can be used to determine glacier mass balance and glacier surface velocity. It is based on topographic differencing of data obtained by altimetry techniques (e.g. LiDAR), microwave techniques (e.g. InSAR) or three dimensional elevation models generated by photogrammetric processing of stereo-imagery (e.g. ASTER or multi-imagery obtained by UAVs) (Immerzeel et al., 2014). For velocity measurements, manual or automated feature tracking is applied. In the case of 'conventional' remote sensing such as ASTER imagery, for both velocity and mass balance measurements, the resolution of the spatial extent of the surface velocity is large and the image resolution generally coarse. In addition, at certain locations the accuracy of elevation change or surface velocity can be considerably reduced by artifacts such as shadows (Immerzeel et al., 2014). Techniques using images acquired by UAVs do not suffer from these issues, thereby providing a promising alternative.

According to (Bamber and Rivera, 2007), the geodetic approach to determining mass balance is the most successful. Strictly speaking it is not a direct measurement of mass balance: it assumes that a measured change in elevation can be translated into an according change of mass. This is only true if there is no change in elevation due to tectonic activity or post glacial rebound, and if the density of the ice has not changed. Since both of these processes likely occur at an insignificant pace compared to mass changes, they may be neglected (Bamber and Rivera, 2007). Still, care should be taken in the case of geodetic measurements, since local surface elevation change may also occur through emergence/submergence velocity as described in section 2.2. Averaged over the entire glacier the effect of submergence/emergence on determining mass balance using the geodetic approach will be negligible. However locally it can be significant, especially in the case of dynamic and fast flowing glaciers (Immerzeel et al., 2014). In this case it is recommended that the emergence velocity is quantified based on estimates of ice thickness (e.g. by means of ground penetrating radar data) and flow velocity and direction (Immerzeel et al., 2014).

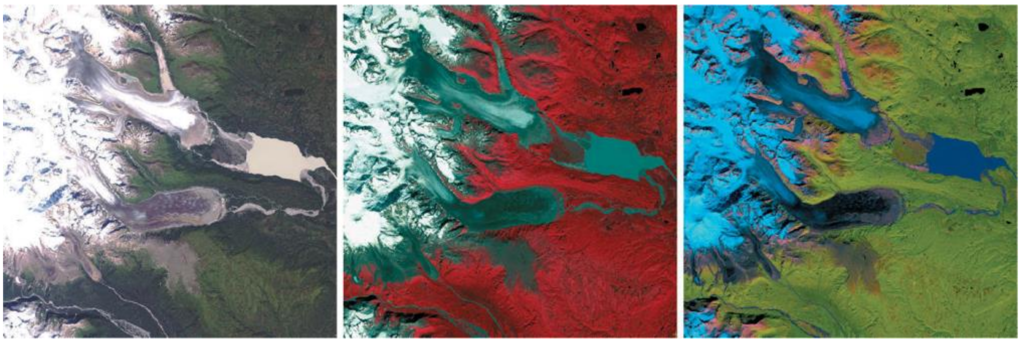

Figure 3.1: Landsat TM color composites of the Tordrillo Mountains in Alaska. Left: true color composite. Middle and Right: false color composites using different band combinations. *Source: Kääb et al. (2014).*

Geodetic methods and glacier mapping techniques will be further discussed below, following a review of the remote sensing systems available. Remote sensing sensors and techniques have been subdivided into conventional types (e.g. ASTER or LiDAR) and the relatively novel technique using UAVs, which has been applied for this thesis and shall be discussed separately.

3.2.1 Conventional sensors and techniques

Both active and passive remote sensing systems are used in glaciological research. Active systems include Radar and LiDAR. Passive sensors acquire images in the visible up to the thermal range of the electromagnetic spectrum (figure 3.2), and include Landsat TM/ETM+, SPOT V, ASTER, QuickBird and IKONOS (figure 3.3) (Singh et al., 2011; Kääb et al., 2014). The main differences between these sensors are their spatial and spectral resolution. Spatial resolution refers to the pixel size of the acquired image, while spectral resolution refers to the range of wavelengths which is captured by a band of a sensor, and thus its ability to resolve various features within the electromagnetic spectrum (ESRI). ASTER (Advanced Spaceborne Thermal Emission and Reflection Radiometer) images are used most often, mainly due to its high multispectral resolution, adjustable sensor settings (allowing for increased contrast over snow and ice), and short revisit times (16 days (Bamber and Rivera, 2007). As of 1995, Corona spy satellite data was declassified. This high resolution (<10m) panchromatic imagery provides valuable historical data, but often requires heavy manual processing (Quincey et al., 2014). Aster, SPOT5, CORONA, QuickBird and IKONOS are capable of providing the stereoscopic images needed to derive elevation data by means of stereo-photogrammetry (Racoviteanu et al., 2008). IKONOS and QuickBird have high (<1m) spatial resolution and would therefore be suitable for detailed glacier studies at basin scale. However they are costly, have a narrow swath size and revisit intervals of months, limiting their use at high spatial scales. Thermal imagery can also be used to infer information about a glacier's extent, by making use of temperature differences caused by the presence of ice (Racoviteanu et al., 2008).

The drawback of optical imagery is mainly the limitation to daylight and cloud-free conditions, which is difficult to obtain over extensive glacierized regions such as the Himalaya (Racoviteanu et al. 2008). Also, images are ideally obtained and the end of ablation season for minimal fresh snow cover. RaDAR (Radio Detection and Ranging), does not have that specific

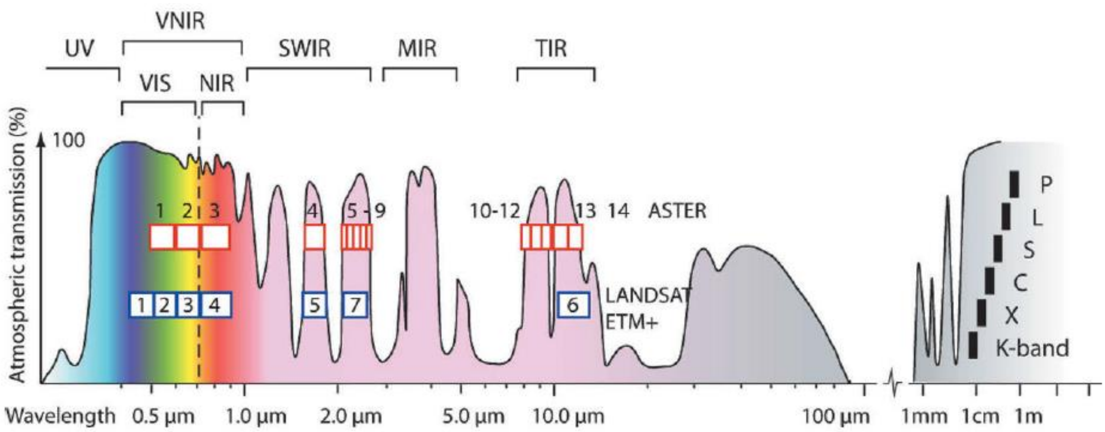

Figure 3.2: Atmospheric transmission, sections of the optical and microwave spectrum and spectral band widths of Landsat ETM+, ASTER and active microwave system (e.g. RaDAR) sensor bands. VIS: visible, NIR: near infrared, SWIR: shortwave infrared, MIR: middle infrared, TIR: thermal infrared, P-K: radar bands. *Source: Kääb et al. (2014).*

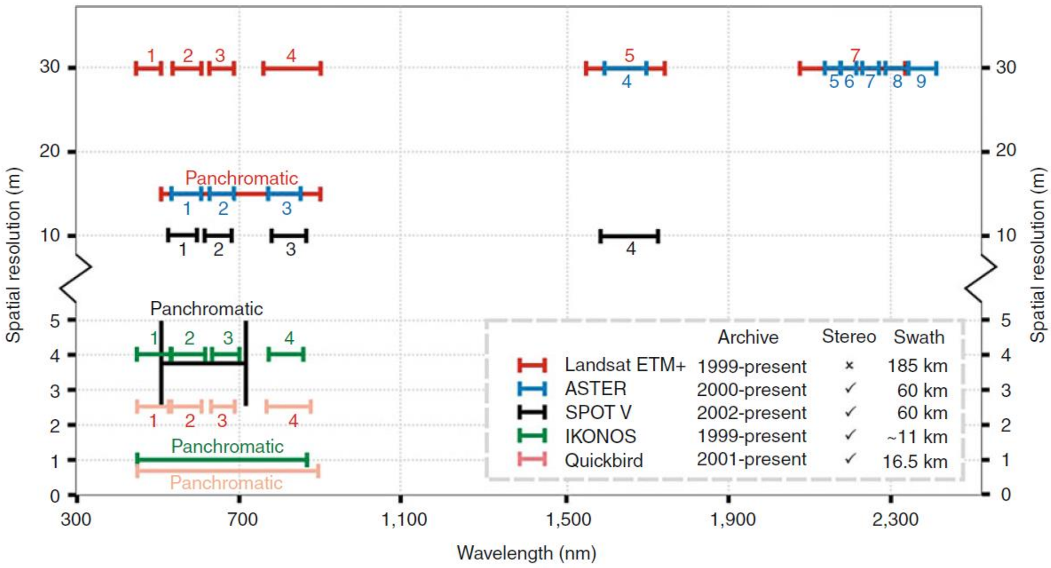

Figure 3.3: Specifications of some optical sensors. Note the high spectral resolution of ASTER in the Mid-IR. Not shown here are ASTER's TIR bands, with 90m resolution. *Source: Singh et al. (2011).*

problem, it being an active microwave system and thus independent of cloud conditions or solar illumination. This also means radar observations can be done on a more regular basis (Kääb et al., 2014). Basically, a radar system sends out a beam of electromagnetic radiation and registers the time it takes for the beam to return to the sensor after being reflected of an object. In this way, objects can be detected, located and/or tracked, altitude can be measured and terrain images may be acquired (figure 3.4) (ESA). Unfortunately, image creation may be hampered by the fact that the backscatter of ice and snow and surrounding terrain can be similar and temporally unstable (Kääb et al., 2014). Hence, mapping of glacier extent with microwave sensors has rarely been employed and so their glaciological applications are different than those of optical sensors (Kääb et al., 2014).

Radar can also be used for altimetry measurements. However this is not often done over mountain glaciers due to a large footprint (sampling area) of several kilometers and the fact that slopes greater than about 1° cannot be accurately recorded. Moreover, microwaves can penetrate dry snowpacks, sending a dual return signal (Bamber, 2006). SAR (Synthetic Aperture Radar) is a form of radar where a higher resolution is reached than with conventional radar, due to the creation of a virtual long antenna. SAR imagery employed in glacier research often is acquired from the Shuttle Radar Topography Mission (SRTM) or the European Remote Sensing satellites (ERS).

LiDAR (Light Detection and Ranging) is basically the same as RaDAR, only it uses pulses of light instead of electromagnetic waves. The advantage of LiDAR over radar is that it overcomes the limitations for radar described above (Singh et al., 2011). If a high enough point measurement density is reached, surface features such as meltwater channels may be mapped. However, LiDAR does have a new set of problems. Atmospheric interference can prevent observation of the surface (Bamber, 2006), processing the data can be time-consuming (Quincey et al., 2014), and LiDAR flights are expensive (Singh et al., 2011).

In the following sections geodetic and glacial mapping techniques and their application using the sensors described above shall be discussed. This will be followed by a review of the application of UAVs in this area of research.

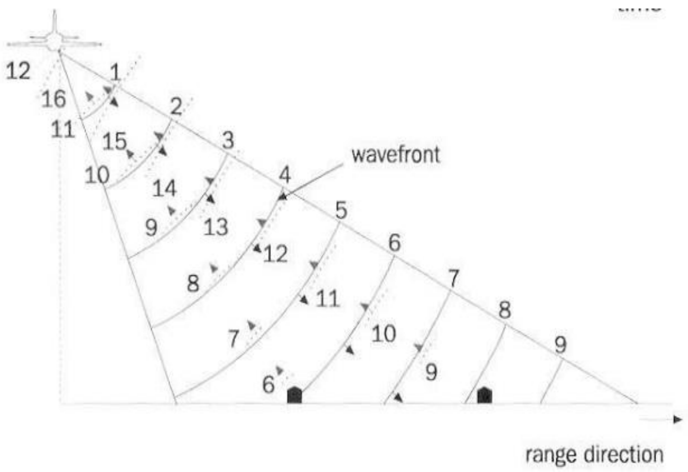

Figure 3.4: Schematic diagram showing the basic principle of RaDAR. Numbers denote points in time. *Source: Lillesand et al. (2008).*

Geodetic methods

The geodetic method to researching glaciers may be subdivided into two data types: raster DEMs, derived from stereo photogrammetry or interferometry, and point measurements (Bamber and Rivera, 2007). When glacier elevation models are created for different moments in time, their difference in volume can be quantified, subsequently converted to mass change and a mass balance can be computed.

Raster DEMs can be created by several techniques, of which aerial (stereo) photogrammetry is perhaps most often employed. This method uses overlapping images (e.g. stereo from ASTER, or multi-imagery from UAVs), to create 3D models of the glacier (figure 3.5). It relies on the recreation of the geometry between the terrain and sensor at the moment of image acquirement. This is done by means of user input of GCPs, aircraft location, geometry and image dimensions in photogrammetric software which subsequently matches the overlapping images. The result is a stereo-model of the scene at the time of image acquisition (Quincey et al., 2014). The accuracy of this method is about equal to the pixel size of the sensor, provided adequate GCPs are taken. In the case of ASTER imagery this is about 15 m. Ideally the GCPs have decimeter accuracy, which requires in situ GPS observations. This limits spaceborne photogrammetry to those glaciers that have that information available (Bamber and Rivera, 2007). UAV imagery can obtain much higher resolution results, which will be discussed in section 3.5.

Since photogrammetry makes use of optical imagery it is subject to atmospheric disturbance of the images. Also, photogrammetry requires enough albedo difference between corresponding images in order to match them. In the case of glacier surfaces snow covered parts do not have sufficient contrast for matching to be possible. This results in large areas for which no elevation data can be extracted by means of ASTER data (Bamber and Rivera, 2007). This problem can be solved by using higher resolution data, such as costly IKONOS or SPOT5 images, or UAV imagery.

Raster DEM generation by means of interferometry makes use of InSAR, which stands for SAR interferometry. This technique makes use of two or more SAR images taken at different times or (slightly) different locations or view angles (Singh et al., 2011). InSAR can be used to extract topography information, and in the case of differential InSAR (DInSAR) to map ice surface motion (velocity and strain rate) with centimeter accuracy (Bamber and Rivera, 2007). This is only relative elevation information and pre-existing DEMs or GPS data are required to obtain absolute height data.

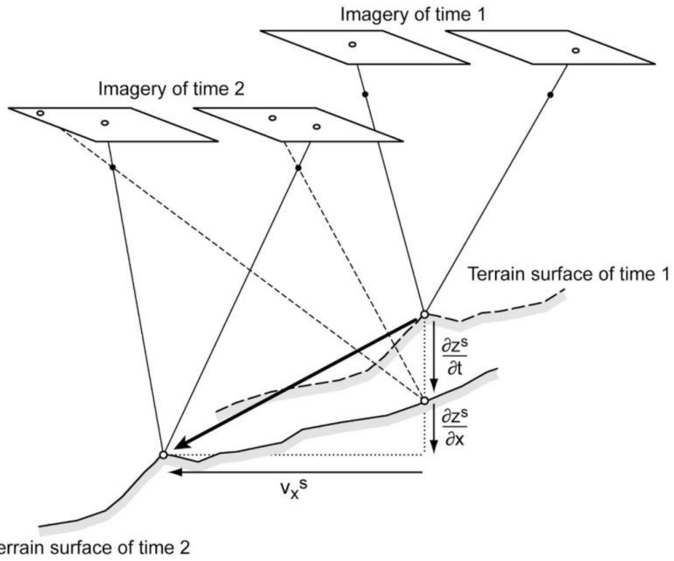

Figure 3.5. Illustration of stereo-photogrammetry. Using imagery of 1 time only, elevation data can be acquired. When using images of time 1 and 2, calculation of surface elevation change are possible. *Source: Quincey et al. (2014).*

Elevation data can also be extracted by means of altimetry. This form of geodetic measurement uses spot height obtained from RaDAR or LiDAR, or in situ GPS measurements. These point measurements tend to be of high (decimeter) accuracy, but have relatively meager spatial coverage. This method is therefore limited by the fact that results needed to be interpolated and extrapolated to provide estimates of elevation differences for an entire glacier (Bamber and Rivera, 2007). DEMs created from LiDAR measurements can be viewed as a 3D point cloud, and are of very high quality. However before such a high quality DEM is acquired, the data must be heavily processed (Quincey et al., 2014).

Photogrammetry, interferometry and point measurement techniques each have their advantages and disadvantages, related to e.g. the accuracy of the measurements or the possibility repetitive measurements (Quincey et al., 2014). They are therefore complementary and are often used as such in glacier mass balance or velocity studies. For instance, Kääb et al. (2012) determine a region wide mass balance of the Hindu Kush-Karakoram-Himalaya, using LiDAR altimetry and a SRTM DEM. In addition topographically corrected, cloud-free Landsat TM and ETM+ scenes with minimal snow cover were used to be able to differentiate between clean ice, debris covered ice, firn and snow, open water and off-glacier area at the LiDAR footprint locations. Bajracharya et al. (2011) created an inventory of glaciers in the Himalaya by means of Landsat ETM+ and SRTM. They used de Landsat images to delineate glacier outlines, and combined these outlines with a DEM from the SRTM to derive parameters such as hypsometry, slope and elevation of the head and snout of the glacier. Subsequently they compared the thus obtained glacier volume and surface with an older inventory in order to determine glacier wastage.

The accuracy of these geodetic mass balance estimations is highly dependent on a number of factors (Racoviteanu et al., 2008). The errors that are introduced during processing propagate further with each step, leading to large errors in output mass balance approximations and therefore needing careful evaluation or validation. After some major post-processing, ASTER DEMs can provide topography of moderate relief glaciers with an accuracy of 15-30 m (68% confidence level), but only 60m (68% confidence) in glacierized areas with steep rock headwalls and large low-contrast accumulation areas. The problem is increased even further in high-relief mountain areas due to slope-aspect error dependence which causes elevation data derived from equator facing slopes to be of better quality due to favorable illumination and sensor-terrain viewing angle (Racoviteanu et al., 2008). The uncertainties involved in the elevation data and the errors introduced during processing mean that satellite derived DEMs of high relief areas cannot be created with sufficient accuracy to detect any change over less than decadal timescales (unless (expensive) ultra-high resolution imagery is used) to make sure the observed change exceeds the uncertainty in the approach (Quincey et al., 2014, Racoviteanu et al., 2008).

Glacier velocity can be also be quantified using remote sensing. Displacement or glacier shape change can be detected by either manually tracking features or by means of algorithms (e.g. CosiCorr) from SAR images or orthorectified images. This, combined with multitemporal DEMs provides horizontal displacement and vertical elevation changes. This vertical change can be converted into a (approximation of) vertical component of glacier velocity (Quincey et al., 2014).

Surface velocity can also be computed by means of SAR, either using differential InSAR or radar offset tracking. In the case of DInSAR, InSAR images are processed in a specific way and differenced, after which displacement can be inferred (figure 3.6) (Quincey et al., 2014). Radar offset tracking is fairly similar to optical image matching. It uses image-matching techniques to track backscatter intensity or radar phase texture between multitemporal SAR images, in order to infer surface velocity.

Which method is best to quantify glacier movement can vary over one scene at one moment in time (Kääb et al., 2014). Thus, like the different techniques to determine mass balance, the methods are used concomitantly. For instance, Kääb (2005) uses a combination of SRTM radar and ASTER DEMs to determine glacier flow velocities of glaciers in the Bhutan Himalayas. After the DEMs were generated they performed image matching and feature tracking software to derive flow velocities. Quincey et al. (2009a) also determined flow velocities, this time by means of a combination of ERS radar and ENVISAT's A(advanced) SAR, supplemented by differential GPS measurements. Using cross-correlation feature tracking they could determine the gradual acceleration of a glacier.

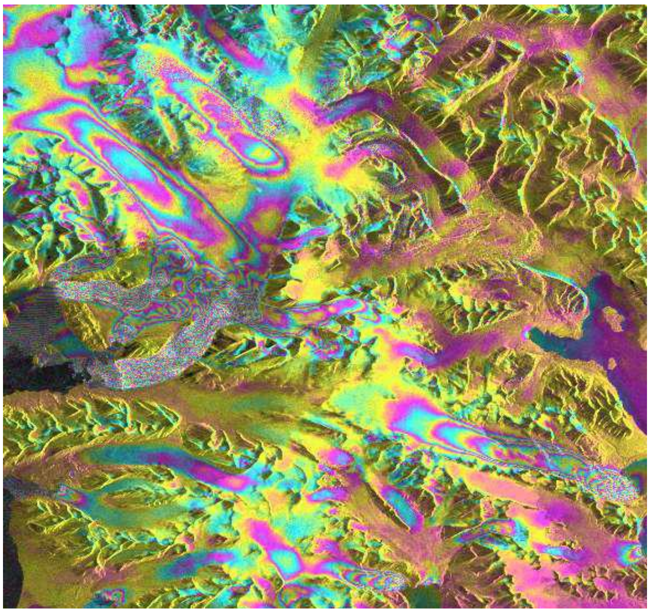

Figure 3.6 Radar interferogram between ERS images of the area around Kronebreen glacier, Svalbard. Color fringes indicate coherence loss due to movement. The Kronebreen glacier (middle left) shows much coherence loss due to large flow velocities. *Source: Kääb et al. (2014).*

(Surface) Mapping

Glacier evolution can be assessed using mapping and detection only. For instance Scherler (2011) uses glacier edge detection from based on ASTER and SPOT images, in order to determine frontal changes of various glaciers between the Hindu Kush and Bhutan. Landsat TM/ETM+ or ASTER images can be used to determine the end of summer snowline by differentiating between the (wet) snow and ice. This transient snowline altitude (SLA) may in turn be used as a reasonable proxy for the equilibrium line altitude (ELA) which can be used to infer information about the glacier (Bamber and Rivera, 2007). This needs accurate determination of the glacier extent, which is not necessarily straightforward for debris-covered glacier margins. Landsat ETM+ and Aster data can also be used to determine surface albedo, which, in addition to in situ meteorological information, can be applied in surface energy balance calculations.

A different application of remote sensing is the use of thermal imagery to delineate the glacier (Racoviteanu et al., 2008), or to determine characteristics of supra-glacial debris layers. If the debris layer is thin enough (<2 cm) then debris overlying the ice is generally colder than surrounding moraine ridges. This difference can then be seen as brightness variations on thermal images. Debris surface temperature can also be derived. This can in turn be used to estimate debris thickness, and so infer sub-debris melt rates (Nakawo et al., 1999, Racoviteanu et al., 2008). The applicability of the thermal approach alone is currently limited to thin debris cover (Racoviteanu et al., 2007). The main shortcoming of mapping debris covered glaciers from thermal data is that recorded thermal emission is not only dependent on the underlying ice, but actually on a number of factors contributing energy balance, such as incoming shortwave radiation, thermal emissivity and meteorological conditions. Also, extraction of reliable surface temperature and actual capability to resolve thermal features is difficult due to the coarse spatial resolution of thermal imagery (Kääb et al. 2014).

In all approaches using optical imagery regions with shadow, clouds, seasonal (fresh) snow, pro- and supra-glacial lakes and debris cover pose problems. Snow covered areas have very little contrast, debris cover has a similar spectral signature to the surrounding moraines and the liquid water in lakes have similar bulk optical properties as ice. This all causes difficulties for automated image processing algorithms. In the Himalaya problems are posed in particular by difficulties with obtaining cloud-free, end of ablation season (ASTER) scenes, and by restrictions on use and export of topographic maps together with the trigonometric and gravity data needed to interpret aerial photography (Racoviteanu et al., 2008). Additional difficulties arise due to 1) lack of standardized image analysis methods to delineate debris-covered ice, 2) limited field validation data (GPS measurements and specific mass balance measurements), 3) lack of accurate elevation data for remote regions and 4) algorithms that can automatically discern debris-covered ice from ice-free areas with debris. This means snowlines or glacier limits have to be manually defined, which is a very time-consuming effort since it is difficult to even locate the edges of a debris-covered glacier in the field, let alone from satellite (even high resolution) imagery (Racoviteanu et al.(2009). Also, what might be a glacier spectrally speaking might not be equivalent to what is a glacier in an ice-dynamical or mass balance system sense (e.g. snowy patches attached to a glacier (Kääb et al., 2014). Marking the limit between debris covered ice and non-debris ice, or distinguishing between stagnant ice and active glacier ice is therefore very difficult (Racoviteanu et al., 2008). While image analysis methods often result in sharp boundaries between different classes, nature mostly contains gradual transitions that are therefore not correctly represented in the digital data (e.g. gradual changes in debris-cover) (Kääb et al., 2014).

Some of the issues with optical remote sensing may be solved by the use of radar or LiDAR.

These techniques have their own set of drawbacks, such as the limitation to large spatial scales or a large price tag. Thus, no matter what spaceborne remote sensing technique is used, uncertainties in glacier mapping will be large (Racoviteanu et al., 2009).

3.2.2 Unmanned Airborne Vehicles

The above section illustrates the difficulties in accurately observing glaciers, be it velocity, glacier mapping or elevation modeling. Often it is a trade-off between resolution, scale, frequency of the monitoring and the price (Whitehead et al., 2013). A major downside is the generally coarse resolution of the remotely sensed imagery, which complicates studies of the glacier surface (Immerzeel et al., 2014). High-resolution images are available (e.g. aerial surveys or IKONOS imagery), but are expensive and require thorough planning. Also, any spectral imagery may be hampered by bad weather or other atmospheric effects (Lucieer et al., 2013). As stated, radar does not suffer from cloud interference, but instead is hindered by geometric distortions, noise and slope effects. Also, in the case of debris-covered glaciers, even if ultra-high resolution imagery is used, uncertainties in debris covered glacier mapping will be large for it is difficult to even locate a glacier boundary in the field. Any algorithms that exist to automatically delineate glacier boundaries and save valuable time often lack the high-resolution DEM needed to apply this algorithm (Racoviteanu et al., 2009). Therefore, glaciological research by means of remote sensing necessarily has often covered large areas and decadal time spans.

While the aforementioned problems cannot be overcome by one single technique, recent advances in photogrammetry and Unmanned Aerial Vehicles (UAVs) may open new possibilities in glaciological research. UAVs are able to acquire high resolution imagery (1-20 cm), are cheap and easy to deploy and can carry multiple sensors. The number of sensors available to mount on small UAVs is increasing rapidly, including SAR, LiDAR and hyperspectral sensors (Whitehead et al., 2013). Besides the development of low-cost drones, new advances in photogrammetric software have driven down the costs considerably and allow high-resolution DEMs and ortho-mosaic images to be generated from the UAV imagery (Whitehead et al., 2013). Also, a major advantage is the flexibility in acquiring of the imagery, both in timing and location, allowing for repeat surveys fairly easily. This high temporal resolution allows ongoing processes such as ice flow, glacier advance, retreat, ablation and lake development to be virtually continuously monitored. Pre-programmed flight paths ensure that the areas of interest are covered fully, by multiple stereo image combinations (Whitehead et al., 2013). Integrated navigation systems and inertial measurement units provide x, y, z positions within 10 m and values for the roll, pith and yaw of the UAV within 2°. This information can subsequently be used as input for the photogrammetry process. The resulting high precision ortho-mosaics can then be used to derive surface motions by feature tracking, either by using software or by visual comparison.

The merits of UAVs has already been shown (Immerzeel et al., 2014; Whitehead et al., 2013). Immerzeel et al. (2014) have employed a UAV to monitor a debris-covered glacier in the Himalaya, in order to quantify surface velocity and mass loss (figure 3.7). Using the high resolution UAV obtained images they created ortho-mosaics and high resolution DEMs of the glacier. These then facilitated accurate assessments of glacier dynamics and surface height changes, at a resolution and accuracy which currently cannot be reached by satellite derived imagery. The high-resolution imagery also allowed for studying of the movement of debris and the behavior of the supra-glacial lakes and ice cliffs (Immerzeel et al., 2014). The data acquisition lasted only two and a half days, but differencing

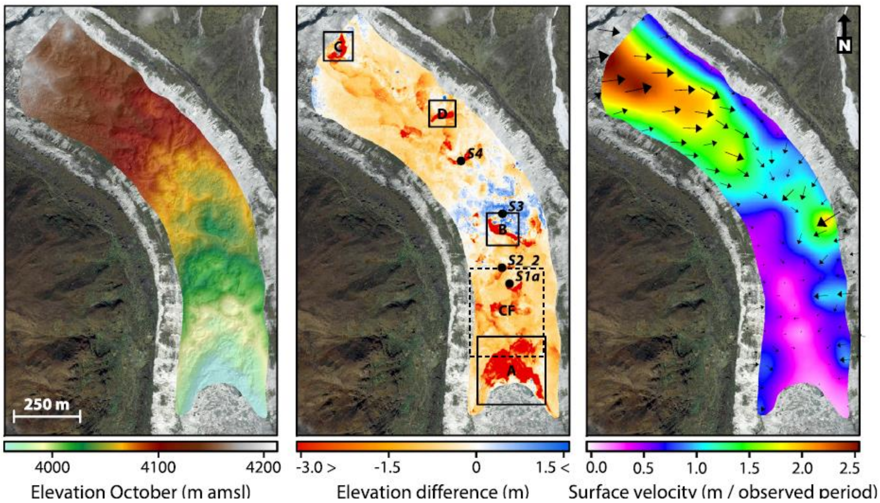

Figure 3.7: Photogrammetically derived DEM (left), elevation differences (middle) and surface velocity (right) of the Lirung Glacier, Nepal, as computed from UAV imagery. *Source: Immerzeel et al., 2014).*

based on the high-resolution DEMs provided the equivalent of millions of stakes at a sufficiently high accuracy (Immerzeel et al., 2014). Vertical errors of a photogrammetically derived DEM can be equivalent to airborne LiDAR, being lower than 0.2 m, while the horizontal accuracies are between 0.3 and 0.4 m (Whitehead et al., 2013). Immerzeel et al. (2014) report a DEM accuracy of about 0.25 m for the vertical and horizontal.

Ryan et al. (2015) have applied UAV stereo-photogrammetry to investigate calving dynamics at a major marine-terminating outlet glacier at the western side of the Greenland ice sheet. They created high-resolution DEMs with vertical accuracies of ±1.9 m, which were used to quantify glaciological processes over a period of two months. They found that by using this technique dynamics of this glacier on a daily and seasonal timescale could be observed.

Clearly UAVs will be particularly useful for glacier research the Himalayas, due to the issues with snow, clouds and limit to large spatial scales with the other methods. A very important feature of glaciers in this region is the layer of supra-glacial debris that often covers the ablation area. It hampers field and geodetic measurements of glaciers, while it greatly influences the surface energy balance of glaciers. UAVs can acquire images with the required resolution to study this feature, providing new opportunities in this field of research.

3.3 Conclusion

In the former chapters it has become clear that glacier dynamics, including mass balance and velocity, are intricate processes which are difficult to research, directly or by means of conventional remote sensing methods. Resolution, scale, frequency of the monitoring and the price are all complicating factors (Whitehead et al., 2013). Supra-glacial debris with it accompanying lakes and cliffs add even more complexities to computing glacier dynamics, as they often act on very small spatial scales. This causes glacier dynamics to not be easily discernible from the glaciers. Glacier mapping is hampered due to stagnation and due to the fact that the spectral signature of debris is similar to surrounding moraine material (Racoviteanu et al, 2008). This can be solved by using geodetic techniques, but these are in turn generally not suitable for studies on small spatial and time scales. Especially any research concerning lakes and cliffs requires high resolution imagery. Lakes and cliffs cannot be discerned by ASTER, which confounds much research concerning these features. For instance, Suzuki et al. (2007) assessed the spatial distribution of thermal resistances of debris using thermal IR ASTER data. The results were satisfactory, but problems arose due to cloud cover or shadow effects, and the fact that ponds and cliffs could not be distinguished. Mixed pixels with debris and ponds occur, hampering any inferences of debris thickness based on thermal resistances (Suzuki et al., 2007).

Thus, computing mass balances or velocity for debris-covered glaciers is challenging. UAVs can provide great progress in this topic of research due to the fact that they can acquire the high resolution imagery required to research these features. This novel technique has been used for this thesis, focused on the debris-covered tongue of the Lirung Glacier in the Nepalese Himalaya. By means of high resolution UAV imagery, differences of the surface of the glacier tongue between October 2013 and May 2014 were determined, in order to gain information about mass loss and surface velocity. The evolution of supra-glacial ponds and cliffs, their contribution to the ablation and the effects of pre-monsoon (May images) and post-monsoon (October images) conditions on these features were also assessed.

4. Methods and Area

4.1 Area

The Lirung Glacier in the Nepal Himalaya (86°E, 28°N), is located in the Langtang catchment, roughly 100 km north of Kathmandu (figure 4.1). The climate in the catchment is dominated by the Indian Monsoon. During the summer monsoon from June to September, heavy orographic rainfall occurs when moisture originating from the Bay of Bengal collides with the Eastern and Central Himalayan mountain front (Wagnon et al, 2013). In the dry season (November to May), the monsoon circulation weakens, allowing the (in the case of Nepal) dry upper-tropospheric westerlies to be dominant (Wagnon et al, 2013). Thus, precipitation (mainly snow) is limited for it is produced by the sporadic passage of westerly troughs (relatively low atmospheric pressure areas) (Immerzeel et al., 2014). Of the total annual precipitation (~800 $mmyr^{-1}$), about 70% falls during the summer monsoon. Therefore, the Lirung Glacier experiences simultaneous accumulation and ablation during the summer monsoon, which makes it hard to separate their individual contributions (Immerzeel et al., 2014; Ageta and Higuchi, 1984). Generally, the amount of precipitation increases with altitude during both the wet and the dry season. The Lirung basin covers 13.8 km^2 (Sakai et al., 2002) and the glacier stretches between about 4000 m above means sea level (amsl) at its terminus and 7234 m amsl at the summit of Langtang Lirung (Immerzeel et al., 2014). The accumulation zone is separated from the glacier tongue, which is about 3.5 km long and on average about 500 m wide. The tongue is covered by debris, features several cliffs and lakes (figure 4.2), and is fed only by avalanches from the steep slopes and the intermittent snowfall on the tongue itself (Immerzeel et al., 2014). The debris is regularly thicker than 50 cm and thus has a strong insulating and shading effect on the ice (Immerzeel et al., 2014). By means of the high resolution imagery and subsequent high resolution ortho-mosaics and DEMs capable of being provided by UAVs, Immerzeel et al. (2014) found that the Lirung Glacier is decaying. On average the melt loss is limited, but its spatial variability was very high during the observed period between May and October 2013. The accumulation area is separated from the tongue, where down-wastage is limited due to the insulating effect of the debris layer. Substantial amounts of melt likely occur in the transition zone between the upper part of the tongue (±4400 m) and the steep accumulation area. Here the debris cover is thin or non-existent, exposing the ice. Ice is also exposed at glacial lakes and associated cliffs. As described in 2.4, these supra-glacial features promote enhanced localized melt. Immerzeel et al. (2014) indeed observed that

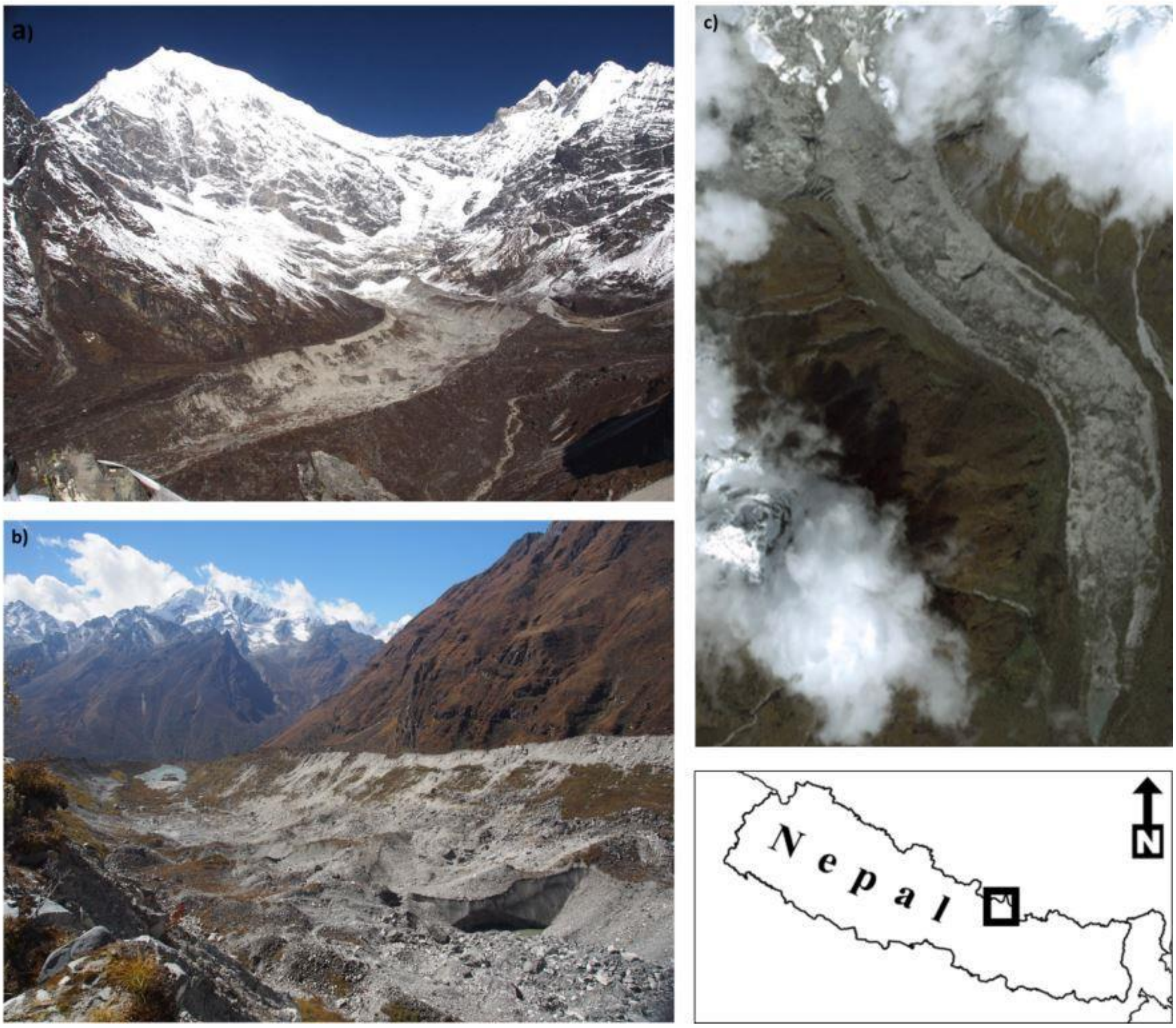

Figure 4.1: The Lirung Glacier and its location. a) View of the glacier tongue and accumulation area, disconnected from the tongue, b) glacier tongue and pro-glacial valley, c) top view of the glacier*. **Source: Bingmaps, Microsoft (2014).*

while supra-glacial lakes and cliffs only cover 8% of the (monitored) area, they generated 24% of the total melt. This could be mostly explained by the backwasting of the ice cliffs (Immerzeel et al., 2014). Sakai et al. (2002) also observed the importance of ice cliff melt on the Lirung Glacier: melt at ice cliffs was ten times higher than at the rest of the glacier surface. Surface velocity of the Lirung was very small and variable: during the period between May and October 2013 it was 2.5 m in the upper part of the monitored area while near the terminus the glacier was virtually stagnant. These figures showed that the glacier had slowed relative to 1994-1996, where the surface velocities over the observed periods were reported to vary between 2.8 and 7.5 m for the middle part of the glacier and between 1.9 and 2.5 m for the lower part, over periods between June and October (Naito et al., 1998; Immerzeel et al., 2014). An important feature observed by Immerzeel et al. (2014) was emergence occurring in the outer bend of the glacier tongue. Uplift occurs at certain locations, due to vertical emergence velocity. In the bend ice is compressed and subsequently pushed upwards. As a result of this emergence and compressive flow, ice loss quantifications (by means of DEM differencing) will suffer from errors. However, since the flow velocity of the Lirung Glacier is very small the error will be limited on the whole. Since the tongue of the glacier has been completely separated from the accumulation area, emergence velocity will likely also have decreased along with

Figure 4.2: Supra-glacial ice cliff (also visible in figure 4.1b) and corresponding small lake on the surface of the Lirung Glacier.

'normal' velocity since 1996. On the whole, the Lirung Glacier is likely in a final phase. It has a thick debris layer, low melt rate and slow flow. The tongue is separated from the accumulation zone, has stagnated almost to a standstill and is losing mass (Immerzeel et al., 2014).

4.2 Methods

The methods used in this study follow those proposed by Immerzeel et al. (2014). Orthorectified imagery and three dimensional information were derived from the Lirung Glacier, its lateral moraines and direct surroundings by means of stereo-imaging and the structure from motion (SfM) workflow (Immerzeel et al., 2014; Lucieer et al., 2013), using images obtained with an UAV. By comparing the thus constructed grid-based DEM to the ones from Immerzeel et al. (2014), information about the dynamics of the glacier between October 2013 and May 2014 was extracted. In this section, a description of the workflow used shall be provided. Firstly image data and reference point acquisition shall be discussed. This will be followed by the applied image pre- and post-processing steps. Finally the method to assess the uncertainty in the results shall be discussed.

4.1 Field collection of UAV images

All images used in this research were obtained from the Lirung Glacier at three different points in time. Field campaigns were performed in May 2013 (M13), October 2013 (O13) and May 2014 (M14). The May and October 2013 flights were performed using the senseFly swinglet CAM. The May 2014 survey was performed with the eBee (also by senseFly), which has slightly better specifications (table 4.1) (www.sensefly.com/drones/overview.html).

The UAVs were flown using the autopilot function, tracing waypoints of a flight route created using the eMotion software included with the UAVs. Inflight monitoring and control were possible through a constant radio link between the UAV and the computer software. The UAVs were mounted with a GPS receiver, an altimeter, a wind meter and a Canon IXUS 125 HS digital compact camera during the 2013 flights, and an IXUS 127 HS for the May 2014 flight. Image acquisition occurred through electronic triggering of the camera by the autopilot system, which should ensure image

Table 4.2: Specifications of the swinglet CAM and eBee UAVs by senseFly. *Adapted from: sensefly.com.*

	Material	swinglet CAM	eBee
Hardware	Wingspan	80 cm	96 cm
	Weight (included camera and battery)	±0.5 kg	±0.69 kg
	Electric motor	Yes	Yes
	Detachable wings	Up to 1km	Up to 3km
	Camera (supplied)	No	Yes
	Cameras (optional)		400-830
Operation	Automatic 3D flight planning	Yes	Yes
	Nominal cruise speed	36 kmh^{-1}	40-90 kmh^{-1}
	Wind resistance	Up to 25 kmh^{-1}	Up to 45 kmh^{-1}
	Maximum flight time	30 minutes	50 minutes
	Maximum coverage (single flight)*	6 km^2	12 km^2
	Linear landing with ±5m accuracy	No	Yes
Results	Ground Sampling Distance (GSD)	Down to 1.5 cm/pixel	Down to 1.5 cm/pixel

** Calculated based on the following test conditions: GSD of 30 cm per pixel, no wind, moderate weather, temp 8°C, new fully charged battery, flight altitude of 1000 m above ground and take off at ±sea level, take off point in center of desired coverage area*

capture at the correct positions (Immerzeel et al., 2014). Both cameras have a 16 megapixel (4608x3456) sensor and lenses capable of focal lengths between 4.3 and 21.5 mm. Focal length determines how much of the scene will be captured, and the magnification of the scene: longer focal length results in narrower scenes and larger magnifications. For all flights the focal length was fixed at 4.3 mm in order to minimize potential motion blur and allow for faster shutter speeds by maximizing the amount of sensed light (Immerzeel et al., 2014). During surveys the appropriate combination of aperture, ISO and shutter speed was automatically chosen by setting the camera in full auto mode. Aperture determines depth of view, or the range of distances at which object appear sharp. ISO determines light sensitivity and shutter speed determines the duration of the image capture. In the full auto mode the camera autofocusses based on the prevailing light conditions. In adequately light conditions this mostly results in images captured with relatively large apertures, ISO values ranging between 100 and 250 and shutter speeds between 1/320 and 1/1250 s.

The details concerning the image acquisition and processing of the M13 and O13 flights are described in Immerzeel et al. (2014). The M14 images were acquired in 3 flights on May 1 starting at around 8 a.m. in the morning. The flights were performed in the morning since then any influence by wind would be minimal and flight stability and thus image quality would be maximized (Immerzeel et al., 2014). The UAV was launched from the same place each time: a boulder on the ridge of the eastern moraine. The desired image overlap was set to 60% in lateral and 70% in longitudinal direction for each flight. The flying height was around 250 m above the surface, and about 0.45 km^2 of the glacier tongue's surface was covered (figure 4.3) (table 4.2).

4.2 Reference point acquisition

In order to georeference the 3D model of the glacier into a real world coordinate system, ground control points (GCPs) and/or camera GPS location data from the time of acquisition have to be introduced into the SfM procedure (Lucieer et al., 2013). During the May 2014 field campaign no new GCPs were taken. For this research, 47 points sampled from the O13 ortho-mosaic and DEM were used (figure 4.5) (Immerzeel et al., 2014). In turn, the O13 ortho-mosaic was georeferenced using 19 GCPs. These were collected using differential GPS (Topcon GB1000 antenna with a PG-A1 receiver) along the eastern and western lateral moraines (Immerzeel et al., 2014). Two identical GPSs were used; a base station and a rover. The base station was installed close to the outlet of the glacier, while the rover was used to measure the 19 GCPs (Immerzeel et al., 2014). The GPS locations were

Table 4.2: Details of image acquisition of the three image datasets. **Source: Immerzeel et al. (2014) (unpublished).*

Project		M13*	O13*	M14
UAV	Type	swinglet CAM	swinglet CAM	eBee
Settings	Average flying height (m above surface)	250	300	250
	Image overlap (%)	60-70	60-70	60-70
Camera	Type	Canon IXUS 125 HS	Canon IXUS 125 HS	Canon IXUS 127 HS
Settings	Focal Length (mm)	4.3	4.3	4.3
	ISO	100-250	100-250	100-250
	Shutter Speed (s)	1/320 – 1-1250	1/320 – 1-1250	1/320 – 1-1250
	Aperture	f2/7 – f8	f2/7 – f8	f2/7 – f8
Images	Moment(s) of image capture	Morning, May 18 and 19	Morning, October 22	Morning, May 1
	Area of glacier tongue covered (km^2)	0.5	0.5	0.45
	# of flights	5	3	3
	# of images taken	776	456	301
	# images used	284	307	301

measured in the center of a bright red cloth of 1.0 by 1.2 m, in order to ensure visibility on the UAV images. Each GCP was taken over a 30 second interval, in which a measurement was taken every second. This was done in order to avoid errors due to antenna rod inclination changes (Immerzeel et al., 2014). The data from the base station and the rover were subsequently processed using Topcon tools software (Topcon Positioning Systems, 2009). The tie-points used for the georeferencing of the M14 campaign were sampled from the O13 results by Immerzeel et al. (2014). These points were selected from stationary off-glacier locations, thus having no changing elevation or flow. The x and y coordinates were sampled from the O13 ortho-mosaic and the corresponding elevation data were sampled from the O13 DEM. Since there was an insufficient amount of off-glacier image coverage from the M14 campaign images from the O13 campaign were added to the M14 dataset in order to adequately georeference the results. All images were subsequently processed into ortho-mosaics and grid based DEMs, using the SfM workflow as implemented in the commercial software package Agisoft PhotoScan Professional Version 1.0.4 (www.agisoft.com).

4.3 Image processing

SfM is a method to reconstruct three-dimensional scene geometry and camera motion from a sequence of two-dimensional images acquired by a camera moving over the scene and thus taken from different viewpoints (Verhoeven, 2011) (figure 4.4). Geometry reconstruction is performed by using algorithms to detect image feature points (e.g. geometrical similarities such as object corners) and by subsequently tracking the movement of these points through the sequence of images (Verhoeven, 2011). SfM differs from classic photogrammetry in that the new generation of image matching algorithms, such as scale invariant feature transform (SIFT) (Lowe, 2004), allow for unstructured image acquisition. This in contrast to the parallel flight lines required by classic photogrammetry (Fonstad et al., 2013). An essential property of these new algorithms is the capacity to recognize thousands of key features in multiple images despite changes in viewpoint or image scale (resolution) (Fonstad et al., 2013).

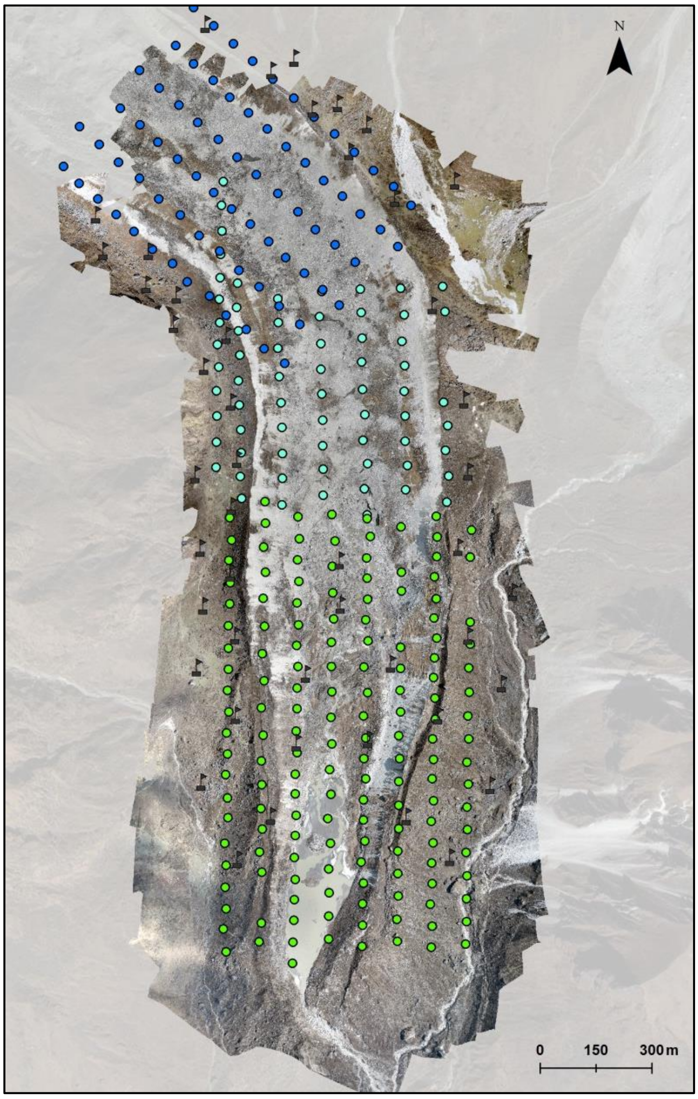

Figure 4.3: Image acquisition (dots) and tie-point (flags) locations. Green: Flight 1, Light blue: Flight 2, Dark blue: Flight 3.

The 3D location and orientation of the cameras and the x, y, z location of these feature points can subsequently be estimated by means of a bundle block adjustment (BBA). According to Triggs et al. (2000) a bundle adjustment is "any refinement method for visual reconstructions that aims to produce jointly optimal structure and camera estimates", with a block making up the sequence of overlapping photos (Triggs et al., 2000). Bundle refers to the fact that structure and camera parameters are all adjusted together 'in one bundle' (Triggs et al., 2000). The bundle block adjustment results in in a three-dimensional sparse point cloud consisting of these identifying features present in the input photographs (Verhoeven, 2011; Fonstad et al., 2013).

Subsequent to the bundle block adjustment, a densification technique can be applied to derive very dense 3D models. This is done by multi-view stereopsis (MVS) algorithms or depth mapping techniques, which allow the computation of surface geometry of the scene (Plets et al., 2012; Lucieer et al., 2013; Furukawa and Ponce, 2009).

The model can then be georeferenced into a real world coordinate system by introducing the GCPs and/or camera GPS location data from the time of acquisition (Lucieer et al., 2013). This georeferenced dense point cloud can next be used to create digital elevation models and

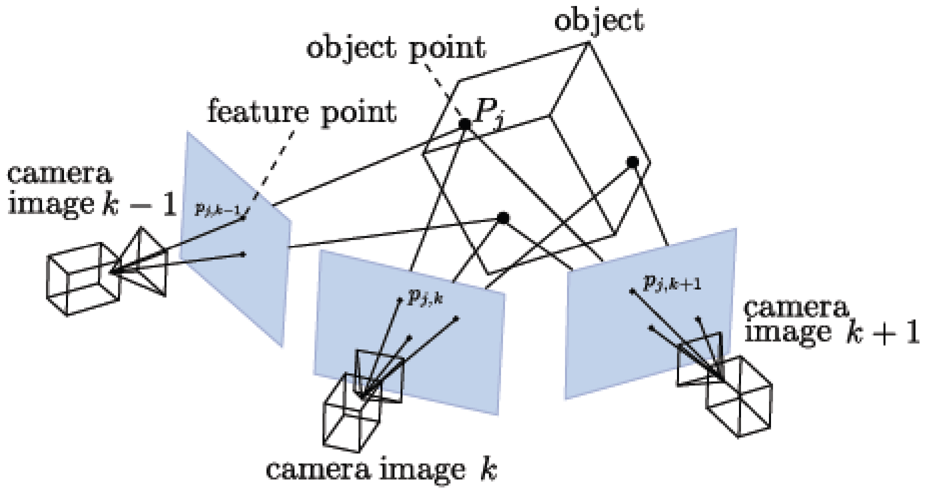

Figure 4.4: 3D structure estimation using different camera viewpoints and motion of the camera. *Source: http://openmvg.readthedocs.org*

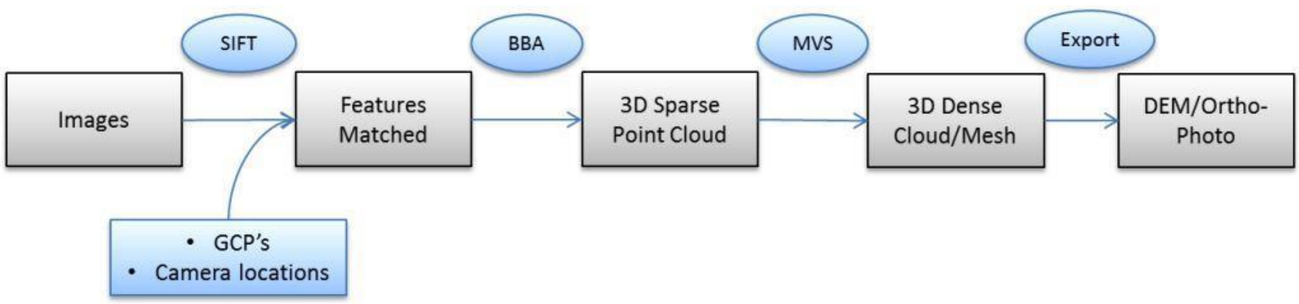

Figure 4.5: Schematic representation of the SfM-workflow. Here, GCP's and Camera Locations are introduced together with the acquired images. Ovals represent processes, squares represent features or products. SIFT, BBA and MVS stand for Scale Invariant Feature Transform, Bundle Block Adjustment and Multi-View Stereopsis respectively.

orthorectified mosaic images (ortho-mosaics) of the scene (figure 4.5) (Immerzeel et al., 2014; Fonstad et al., 2013).

In this study, the SfM workflow as implemented Agisoft PhotoScan (www.agisoft.com) was used. The exact algorithms Photoscan uses are not detailed in the manual, but it largely follows the SfM procedure outlined above and explained by Verhoeven (2011). The processing is divided into three stages (figure 4.6): alignment, dense cloud construction and geometry reconstruction.

1. **Camera alignment** resulting in a sparse point cloud and a set of camera positions. In classical photogrammetry camera interior and exterior orientation have to be determined manually, in order to correct for any lens distortion effects. In contrast, PhotoScan performs an auto-calibration based on only the image data alone during the BBA process. During BBA appropriate calibration parameters and the relative positions of the camera and of the feature points on the objects are estimated. Several iterations are run where the algorithm, using the camera focal length provided with the images, uses the relative 2D positions of the feature points in two images to derive rough 3D coordinate estimates of these points relative to the camera positions. Then the camera parameters and the 3D point coordinates are

iteratively refined until a certain threshold in the variance of point positions has been reached, or until a certain number of iterations are performed.
Subsequently, another image is added, the matched feature points of that image are fit into the existing 3D model and its parameters are iteratively refined. This process is followed for all images, and after the last image has been added another bundle adjustment is done to refine the entire model. This step has been combined with the addition of GCPs, tie-points and camera locations, resulting in a georeferenced point cloud.

2. **Dense cloud construction**. Based on the images, the sparse point cloud and the camera positions, orientation and calibration depth maps can be created by computing the distance between camera and pixel, for every pixel in each image. The dense cloud is subsequently constructed from these depth maps. Prior to the construction of the dense point cloud, the sparse cloud can be edited to remove e.g. outliers or noise.
3. **Reconstructing geometry**. Based on the dense point cloud PhotoScan reconstructs a 3D polygonal mesh that represents the scene's surface. This mesh can also be manually edited. Detached components or clear anomalies of the surface can be removed, holes in the mesh can be closed, etc.

When the mesh has been constructed, the scene can be exported as an ortho-mosaic and/or DEM. These products can subsequently be loaded into GIS software packages to be viewed, edited and/or analyzed. The resolution of the product can be set manually, based on a suggested resolution by PhotoScan.

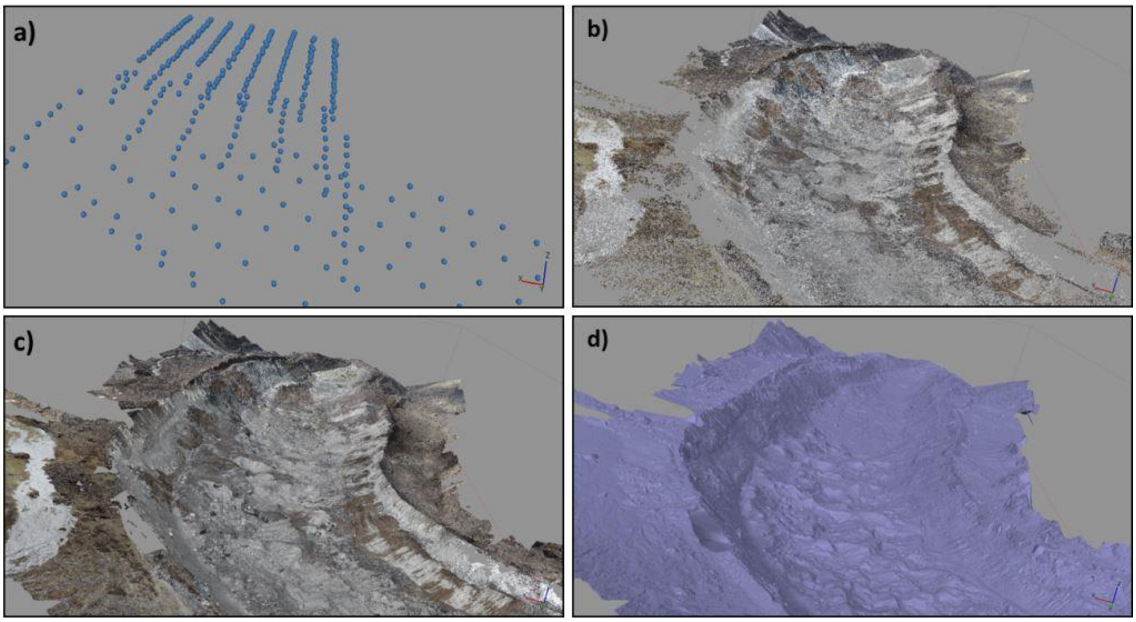

Figure 4.6: Steps in the 3D model construction process. a) Representation of the image locations, b) Sparse point cloud, c) Dense cloud, d) Mesh.

4.4 Ortho-mosaic, DEM and difference DEM analysis

In this research ArcMap, a subpart of the ArcGIS software package (version 10.2.1) by ESRI, Inc. was used to further process the resulting mosaic and DEM. The results were examined based on visual interpretation and differencing the DEMs of the three image datasets.

- **Visual interpretation.** Both mosaic and DEM were visually evaluated based on distinct surface characteristics (e.g. cliffs and lakes). The M14 ortho-mosaic was compared to the mosaics of M13 and O13 in order to assess any surface changes that occurred over this time. The melt and retreat of cliffs between the O13 and M14 campaign was evaluated, together with growth or shrinkage of lakes. This was done by measuring the distance between corresponding points on the edges of the features in the two ortho-mosaics, and by calculating the surface areas of the features for both image dates. Surface velocity was computed, also by manually tracking features on the surface. Distinct objects (i.e. boulders) were selected on both the O13 and M14 ortho-mosaics and the distance between congruent features was subsequently measured. The length and bearing of these lines then resulted in a measure for surface velocity at that point over the period between O13 and M14 (i.e. 190 days). A surface velocity field was subsequently interpolated from the velocity vectors by means of kriging.
- **DEM differencing.** Downwasting was assessed by differencing the DEMs of O13 and M14. First the M14 DEM was corrected for the flow which occurred over the same time period, using the flow vectors constructed for the surface velocity measurements. This ensured that the difference DEM showed surface lowering for the same location at both moments in time. Subsequently the mass loss was computed using the average surface lowering over the observed area. The average ice loss (expressed in meters) was converted to ice loss in m^3 by multiplying with the observed area. Subsequently, assuming an average ice density of 900 kgm^{-3}, this was converted to mass loss in water, both m^3 and mm mean water equivalent (m.w.e.) per unit time. These calculations were performed for the entire observed area, the cliffs, lakes and terminus. The calculated changes were then compared to the changes that had occurred between May and October 2013. The contribution of the calculated amount of melt water has been evaluated against total catchment runoff of both the Lirung and Langtang catchments.

4.5 Uncertainty assessment

22 additional tie-points were sampled from the O13 ortho-mosaic and DEM. These were not introduced during processing, but were used to estimate the accuracy of the M14 results. Using a similar method by which surface velocity was measured, distance between two congruent stationary points on off-glacier area was measured. The sampled points were evenly spread over the entire area, to decrease location dependency of errors as much as possible. The distance in the x and y directions represented the x and y displacement errors. The difference in elevation represents the elevation displacement. This error is in respect to the O13 results, and therefore the reported accuracies from Immerzeel et al. (2014) were also taken into account during the final accuracy calculation.

In order to achieve the highest possible accuracy, DEM construction has been performed several times. The different variations of input data and program settings that were used are described in full in section 6.1.

5. Results

In the following chapter the results of this study will be presented. This will be done in two main sections. First the analysis of the observed surface features will be discussed, followed by a discussion of the observed surface elevation change over the winter period between October 2013 and May 2014. The analysis of the surface features will begin with a discussion of the observations from the M14 ortho-mosaic and DEM. This will be followed by a comparison with the M13 and O13 ortho-mosaics and DEMs as computed by Immerzeel et al. (2014). Subsequently the surface velocity over the winter period, computed based on feature tracking on the O13 and M14 ortho-mosaics, will be discussed.

Elevation change shall be discussed based on observations from the calculated differences between O13 and M14. Corresponding mass change over the winter period will be treated and will be concluded by a comparison to the elevation and mass changes over the summer period between M13 and O13, as observed by Immerzeel et al. (2014).

5.1 Analysis of surface features

5.1.1 Surface features of the May 2014 ortho-mosaic and DEM

In figure 5.1 the generated ortho-mosaic and DEM for May 2014 are shown (see appendix A and B for full-page versions). The scene covers a surface area of about 2.5 km^2 and is located between 3900 and 4200 m amsl. The observed part of the glacier tongue is ±0.45 km^2, approximately 1370 m long, and ranges between 3990 and 4200 m in elevation. The pro-glacial area consists of several (meltwater) streams that flow into the pro-glacial lake at the southern end of the image scene. The holes that appear on the eastern outer glacier area are caused insufficient outer glacier area UAV image coverage. Another hole was formed in the northwestern corner, caused by deficient photo alignment. A large part of the glacier tongue's surface is clearly visible however, thus various observations could be made.

Subparts of the ortho-mosaic and DEM, based on the location of sub-debris ice, are presented in figure 5.2 and show the observed area of the glacier tongue (see appendix C and D for full-page versions). For further discussion purposes, the glacier has been split up into three parts : the upper, middle and lower area, based on the white, red and green areas in the DEM of figure 5.2. Distinctive surface features in the ortho-mosaic are the supra-glacial cliffs and lakes. Cliffs are indicated in figure 5.2 by rectangles and numbers 1 to 4. Lakes are in turn denoted by circles and characters A to C. The largest cliffs are generally facing in a northern direction, and lakes appear to be mostly present in depressions in the glacier surface. Only the cliffs at the terminus are facing southeast to southwest, and are smaller than Cliffs 1-3. The orientation and size of the cliffs are likely controlled by the incoming radiation. As explained in section 2.4, cliffs facing north receive less direct solar radiation and are therefore able to retain a steep slope and large surface area. This in contrast to the south(west) facing cliffs, which experience large amounts of melting due to the direct incidence of sunlight. Some of these features can also be recognized in the DEM: especially Cliff 2 is very distinct (figure 5.2 and 5.3). The cliff edge is clearly visible, with a relative depression of the surface exactly in front of the cliff. This depression is partly occupied by a lake. Lake C is also visible in figure 5.3, as lake and as corresponding depression in the top left corner of each panel. Cliff 1 can also be recognized in the DEM, though less clear. Near Cliff 1 however a depression does stand out. This depression, like the one near Cliff 2, coincides with the small Lake A in figure 5.2 (figure 5.4). Other depressions are also visible in the DEM, but these are not all accompanied by marked features in the ortho-mosaic: e.g. the large depression directly north of Cliff 2. Another surface characteristic present in the DEM but not so easily recognizable in the ortho-mosaic is a relatively swift drop in elevation (±20 m), in in the middle of the glacier. There is a similar drop visible at the terminus, and this one likely represents the transition from ice to glacier outwash plain. This drop can be recognized in the ortho-mosaic by the cliffs at the terminus.

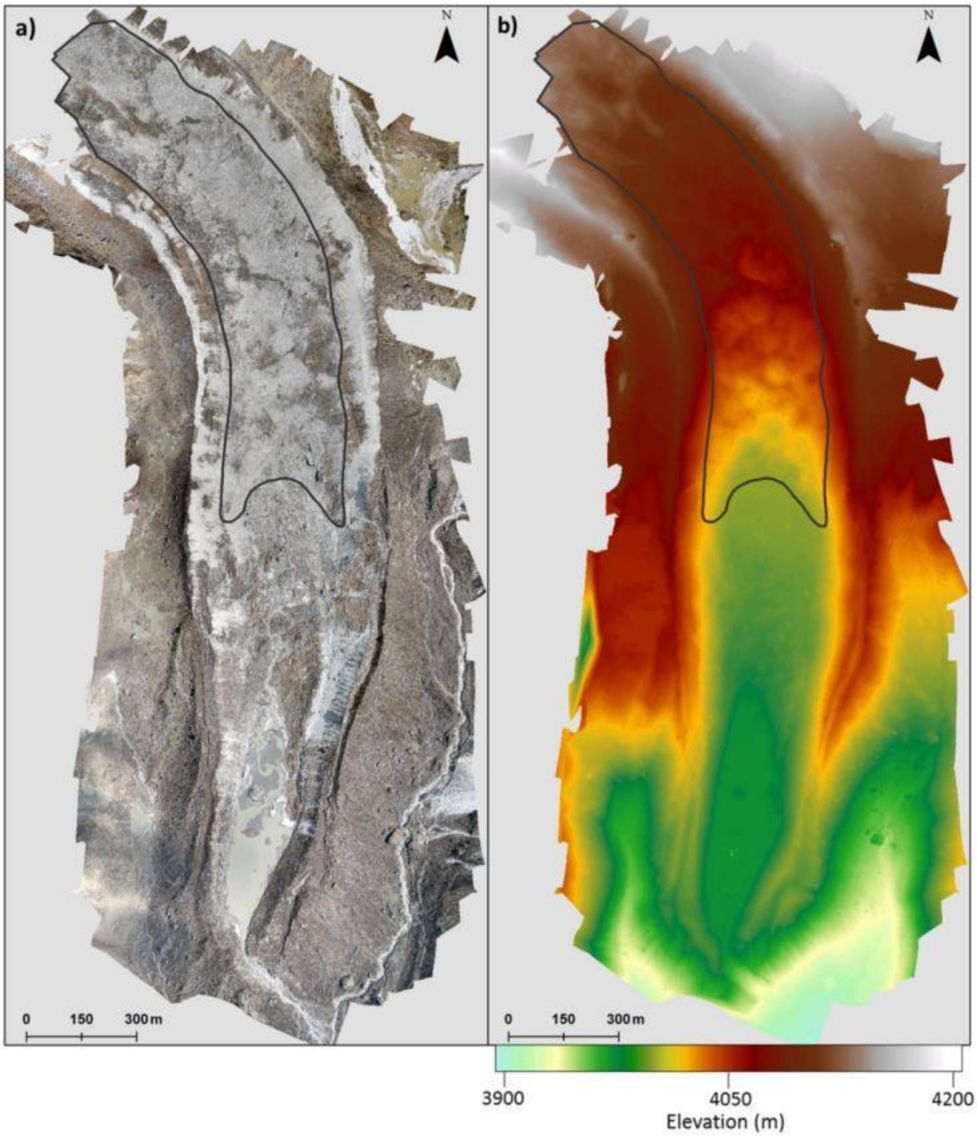

Figure 5.1: a) May 2014 ortho-mosaic of the complete scene, 10 cm resolution. b): May 2014 Digital Elevation Model, 20 cm resolution. The observed area of the glacier tongue is outlined in black.*(See appendix A and B for full-page versions).*

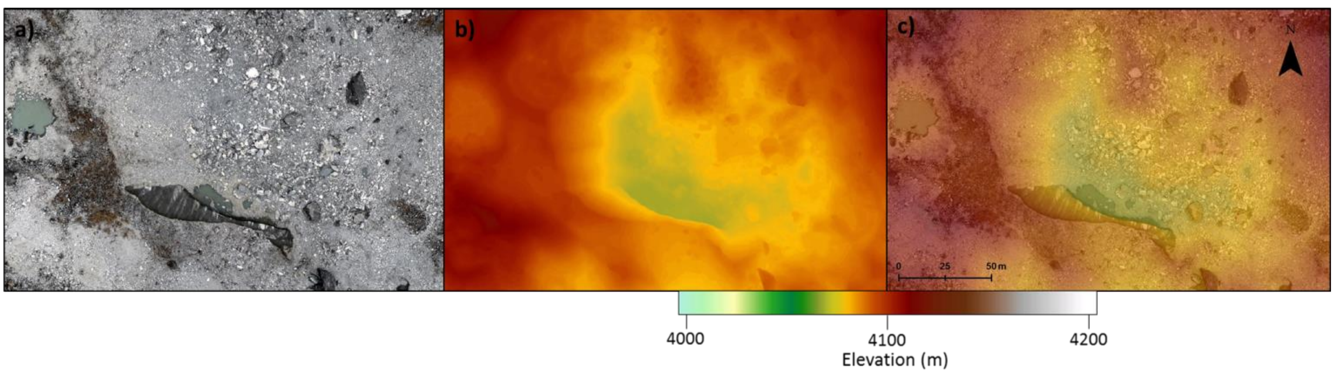

Figure 5.3: Close up of Cliff 2 in figure 5.2. a) Ortho-mosaic, b) DEM, c) Transparent overlay. In the top left of each panel there is a small lake present, recognizable in both the ortho and the DEM (as a small depression).

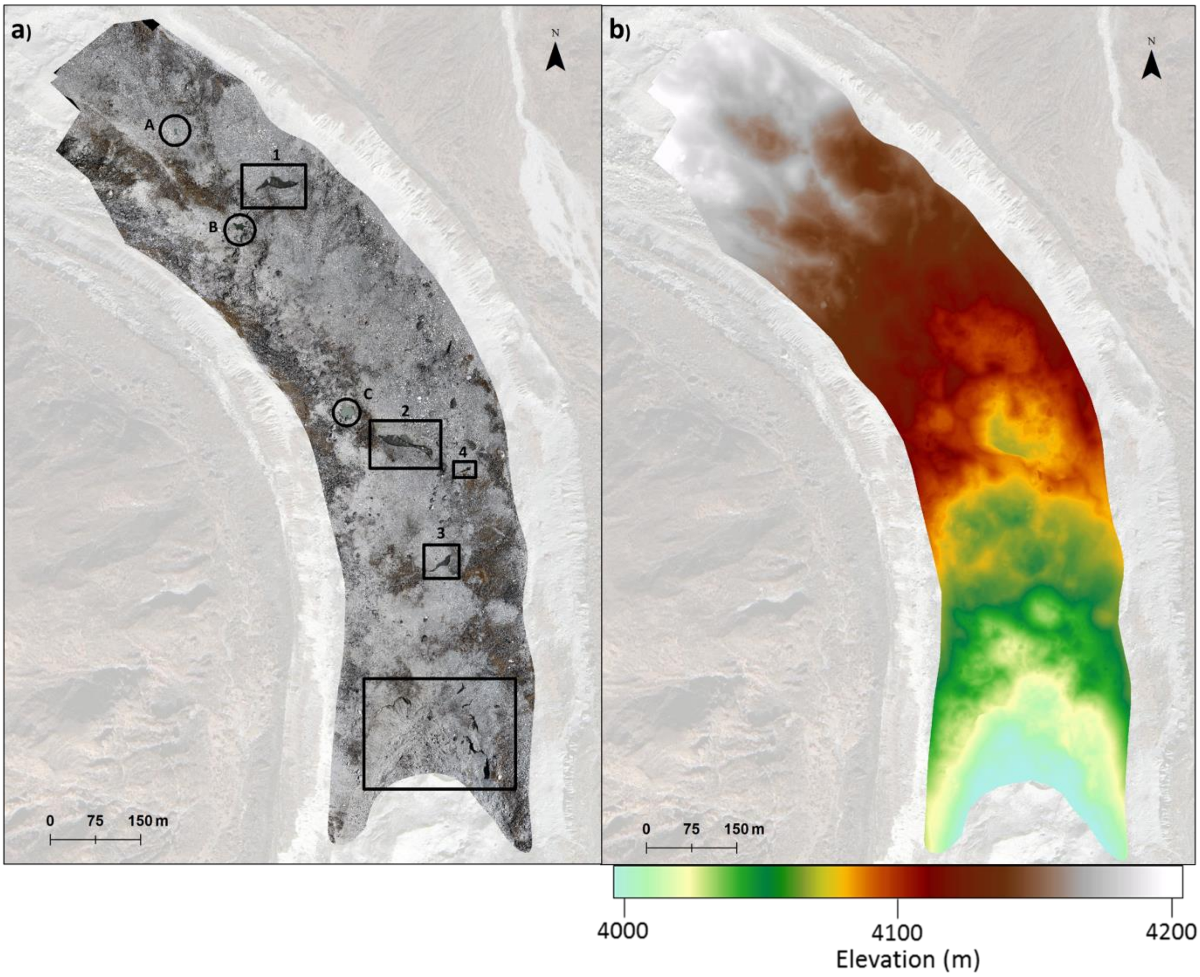

Figure 5.2: Studied subset of the Lirung Glacier. a) May 2014 ortho-mosaic (10 cm). Rectangles denote ice cliffs, circles denote supra-glacial lakes. b) May 2014 DEM (20 cm).*(See appendix C and D for full-page versions).*

5.1.2 Comparing the 2013 and 2014 ortho-mosaics and DEMs

The features described in the former section have been compared to the ortho-mosaics of May 2013 and October 2013 (M13 and O13), constructed by Immerzeel et al. (2014). The period between M13 and O13 constitutes the summer period, and includes the (wet and warm) summer monsoon. The period between O13 and M14 covers the dry and cold winter period. In this section the comparison of surface features shall be presented. This will be followed by an evaluation of the surface velocity between O13 and M14, based on manually tracking features on the respective ortho-mosaics.

Surface feature comparison

The most obvious difference between the two periods is the fact that the large ice cliffs have undergone considerably less change over winter than over summer. In figure 5.5 Cliff 1, 2 and 3 for the three image dates are shown. It is visible that there is very little difference between O13 and M14 images, while M13 images clearly look dissimilar. For instance in the images of Cliff 2 it can be seen that between M13 and O13 an entire portion of cliff disappeared, decreasing the surface area of bare ice by about 500 m^2. According to Immerzeel et al. (2014), this was likely caused slumping of the cliff wall. The pond in front of the cliff disappeared, likely filled by the slump. In contrast to the change between M13 and O13, the largest difference between O13 and M14 is the eastward expansion of the lake in front of the cliff by about 6 m. Cliff 3 shows very little change in shape over

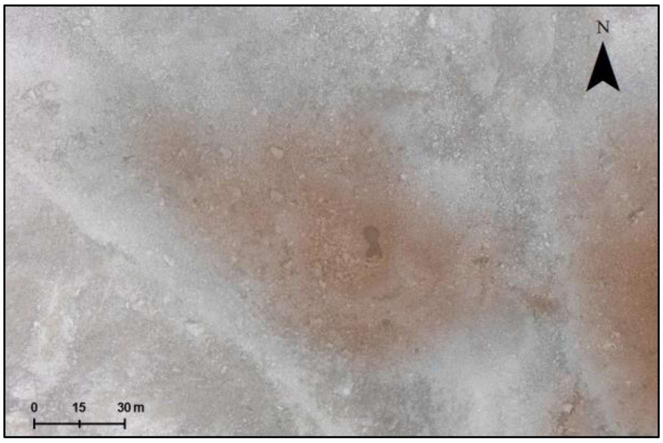

Figure 5.4: Transparent overlay of the M14 DEM and ortho-mosaic. In the center of the depression a small lake A is present.

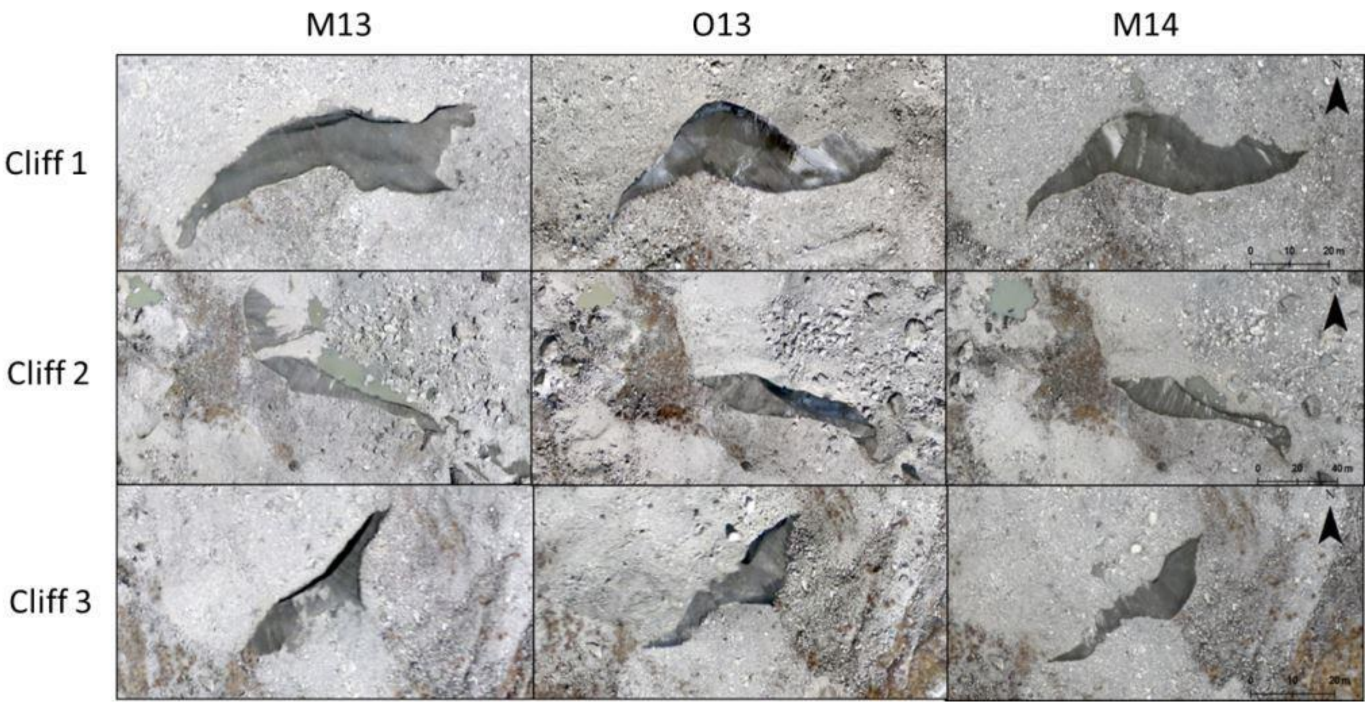

Figure 5.5: Ice cliff change over 18 months. From left to right: May 2013, October 2013 and May 2014 images. From top to bottom: Cliff 1, 2 and 3. At Cliff 2, a large decrease in bare ice area can be seen.

both seasons. However, during the summer period the cliff shifted up to 9 m southeastward, while in the winter period it retreated 1.5 m at most.

The relatively small amount of change between O13 and M14 is also apparent for the other cliffs on the body of the glacier. In sum, cliff retreat was far more substantial in summer than in winter. Where cliff retreat distances of 7-11 m have been recorded over summer (Immerzeel et al. 2014), retreat during winter does not exceed 2.5 m. It should be noted that the southwest facing cliffs at the terminus of the glacier tongue have retreated significantly farther, reaching maximum retreat rates of 6.5 m during winter, and up to 13 m over summer. In fact, the largest changes observed from the ortho-mosaics occurred at the terminus (Figure 5.6). Here it is visible that the cliff surface area greatly varied over the period 2013-2014, with the largest surface area in O13 (almost 2150 m^2), five times as large as in M13. During the winter period it decreased again to about 825 m^2.

Further observations are that in the O13 ortho-mosaic, small (±10 m^2) bare ice areas are

Figure 5.6: May 2013 (a), October 2013 (b) and May 2014 (c) images of the terminus. The largest bare ice surface area is reached in October 2013.

Figure 5.7: Appearance and disappearance of cliff surface area. a) M13, b) O13 and c) M14.

visible, while these are not present in M13 or M14 (figure 5.7). These patches of ice are usually facing western to southern directions.

Bare cliff surface areas have been computed for each image date. From these calculations it can be inferred that even though cliffs appeared and disappeared over summer, total cliff surface area did not change much between M13 and O13. Both times the cliffs covered about 1% of the total observed area. However, between O13 and M14 ice surface area did change, decreasing to about 0.6% of the total observed area in M14. This could be due to the fact that during summer monsoon rains, bare ice areas remain free of debris while during the dry winter debris and dust is able to cover the ice.

Supra-glacial lakes also experienced fluctuations concerning shape, size and number. Over the year, growth, shrinkage, appearance and disappearance of these lakes occurred. For instance, between O13 and M14 two lakes appeared (B in figure 5.2) near Cliff 1, having a total surface area of about 200 m^2 (figure 5.8). The lakes have formed in a depression in the surface, visible in the DEM. In the second panel of figure 5.5 the continuous growth of another lake (Lake C in figure 5.2) can be seen in the upper left corner of the images. Visible in this panel is also the shrinkage and subsequent growth of the lake in front of Cliff 2, with the largest surface area in M13. A similar trend is visible for Lake A (figure 5.4). This lake also shrinks and grows again during the year, showing surface areas of ±65, 20 and 40 m^2 for M13, O13 and M14 respectively.

The shrink over summer and subsequent growth during the winter period is also apparent in total supra-glacial lake surface area, which differs from the cliff surface area fluctuation pattern. Between M13 and O13 the surface area dropped from ±0.22 to 0.09% of total observed area, but rose to ±0.22% again M14.

In the pro-glacial area, which is covered by various lakes and streams, very little change in size was noticeable. The lakes and streams had all generally retained the same surface area and shape.

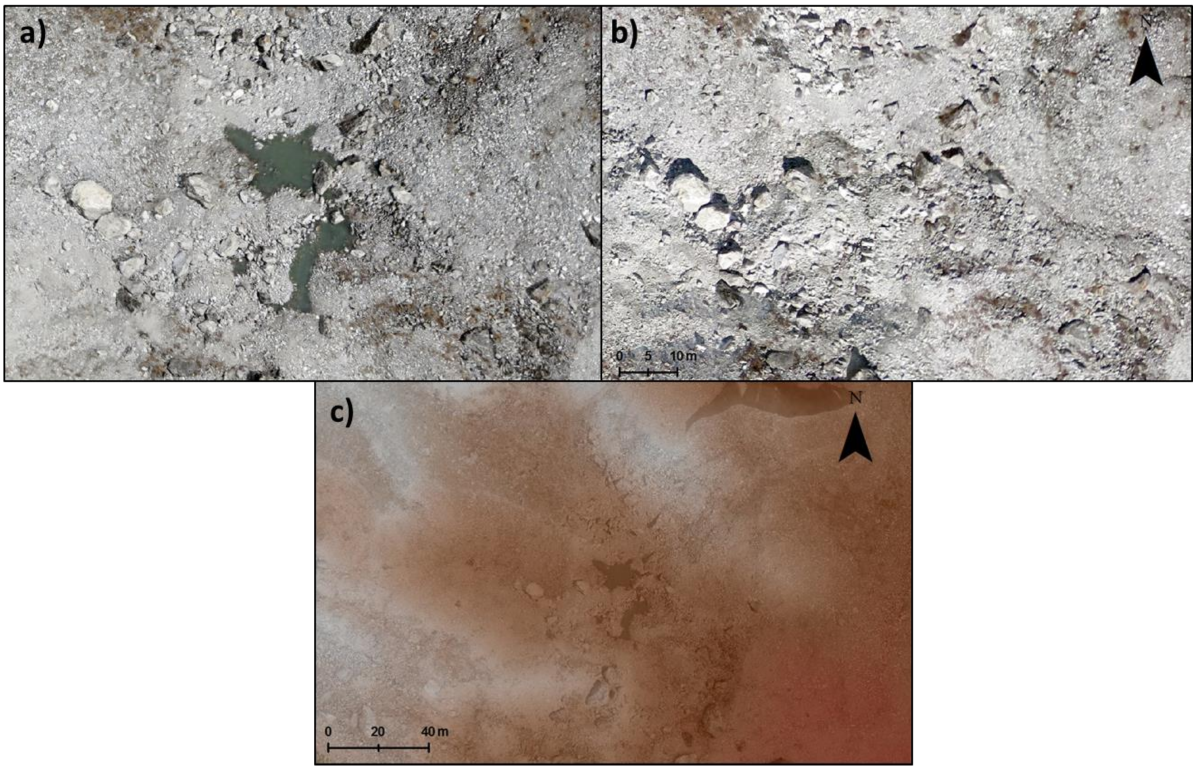

Figure 5.8: a) The appearance of lake B in May 2014, not present in October 2013 (b). c)location of lake B in the M14 ortho-mosaic overlain by the M14 DEM.

Surface velocity between October 2013 and May 2014

Surface velocity was evaluated, by means of manual tracking of features on the surface (i.e. boulders) on the ortho-mosaics of O13 and M14. The direction of flow and velocity of these points are shown in figure 5.9. In figure 5.9a the vectors are displayed on a flow field calculated by means of interpolation (kriging) of the flow vectors (see appendix E for full-page version). It can be seen that the upper part of the glacier apparently revolves around a fixed point and basically flows upstream with relatively large velocities: ±1.4 m over 190 days (or ±0.007 $mday^{-1}$). Upstream flow over such a large area is considered unlikely, and probably results from errors that originated during the processing of the images. The mean velocity of the entire glacier tongue is much lower: ±0.7 m (or ±0.004 $mday^{-1}$), with an average flow direction to the south. The middle and bottom part of the tongue both show velocities of around 0.4 m (±0.002 $mday^{-1}$). Since upstream flow was considered unlikely, these vectors were excluded from further mean surface velocity calculations. When discounting upstream flow the upper glacier area shows an average velocity of ±1.2 m (± 0.007 $mday^{-1}$) and the overall flow velocity drops to ±0.4 m (0.002 $mday^{-1}$) directed somewhat more to the southeast. Further observations are that the middle part of the glacier displays a region of slow flow, upstream of Cliff 2. Also, the lower part of the glacier appears to have relatively larger flow velocities on the western side than on the eastern side, though on both sides the flow is directed mainly towards the middle. By displaying the flow vectors on top of the DEM (figure 9b), it can be inferred that flow is mostly directed toward relatively low lying areas, such as the depression in front of Cliff 2.

The flow velocities approach those reported by Immerzeel et al. (2014). They state velocities between 2.5 m and near stagnancy over 154 days (±0.02 $mday^{-1}$) (figure 5.10). The region of relatively slower velocities in the outer curve is also present over summer. Leaving out of account the clear dissimilarity at the upper area of the glacier, a clear difference is that the summer velocity field shows a considerably more heterogeneous pattern. This occurs especially in the middle and eastern side of the glacier, where the winter flow field is largely homogeneous.

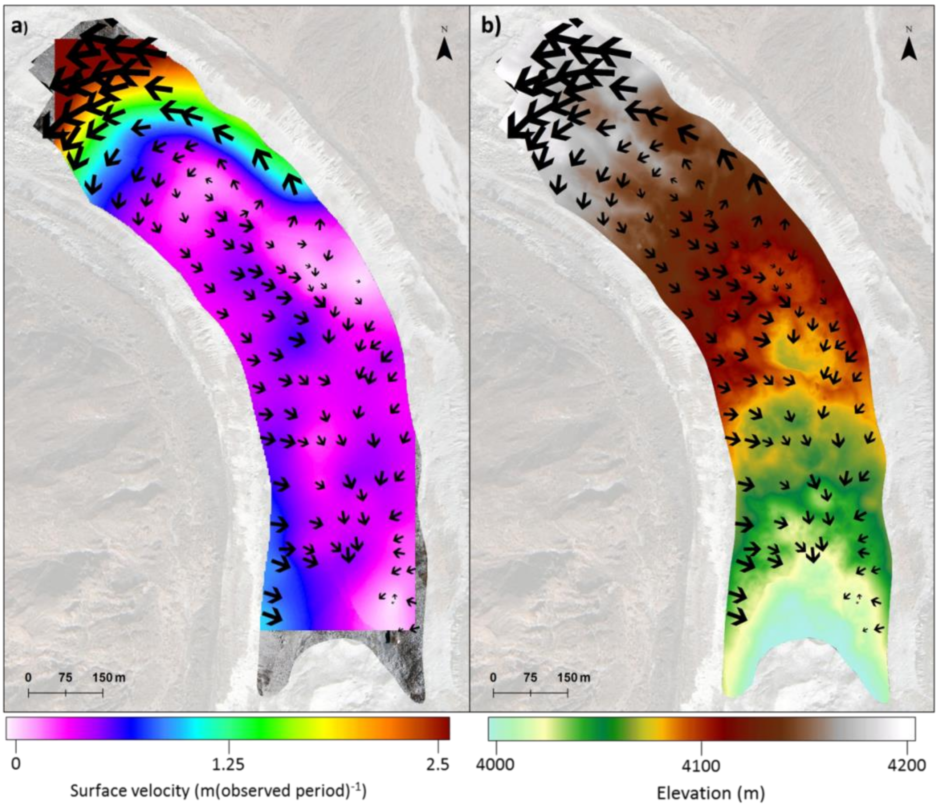

Figure 5.9: a) Surface velocity and direction over the period between O13 and M14. Arrow length indicates relative velocity *(See appendix E for full-page version)*. b) Velocity vectors over the same period displayed on DEM.

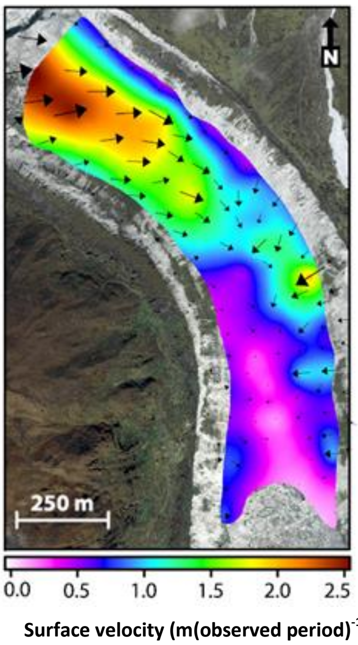

Figure 5.10: Surface velocities computed over summer. Note that the observed period here constitutes 154 days. *Adapted from: Immerzeel et al. (2014).*

5.2 Surface elevation and mass change

5.2.1 Surface elevation change between October 2013 and May 2014

The surface elevation change that occurred between O13 and M14 has been computed by subtracting the O13 DEM from the M14 DEM. The resulting difference DEM is shown in figure 5.11 (see appendix F for full-page version). The computed values are likely not entirely correct, due to difficulties that occurred during processing and caused problems for the construction of the DEM. This will be further discussed in section 6. Even though the values likely do not truly reflect reality they are still reasonable indications of the changes that occurred between O13 and M14. The entire upper half of the glacier shows elevation decrease of up to 3 m, while much of the lower part of the glacier shows an elevation increase, ranging from a few cm to a few dm. The average elevation change over all pixels is -0.63 m, with a standard deviation of 0.79 m. The regions of slight elevation changes are depicted more clearly in figure 5.11b (see appendix G for full-page version). Here the elevation change has been classed between the values of 1 and -1 m, with 8 classes of 0.25 cm each. This figure shows that the glacier mainly experienced elevation changes ranging between 1 meter rise and fall. Only the upper part, the areas around the cliffs and the terminus experienced larger decreases in elevation (figures 5.11 and 5.12). A maximum elevation decrease 13 m was observed in the terminus area. In the region near the outer curve of the glacier the surface has apparently risen a few centimeters up to 0.5 m. This area coincides with the region of slow surface velocity noted above, and likely this surface increase (and slow velocities) are due to emergence which has also been noted by Immerzeel et al. (2014). The surface also seems to have risen at the lower middle left area, but is most likely unrelated to emergence. Somewhat southwest of Cliff 1 a region of relatively greater surface lowering is visible (figure 5.13), and coincides with the area where Lake B appeared. However the lake itself is not located within the lowered surface area. Another observation is that the bare-ice areas/cliffs that had apparently disappeared over winter on the ortho-mosaic, are still visible as regions of increased downwasting in the difference DEM (figure 5.14).

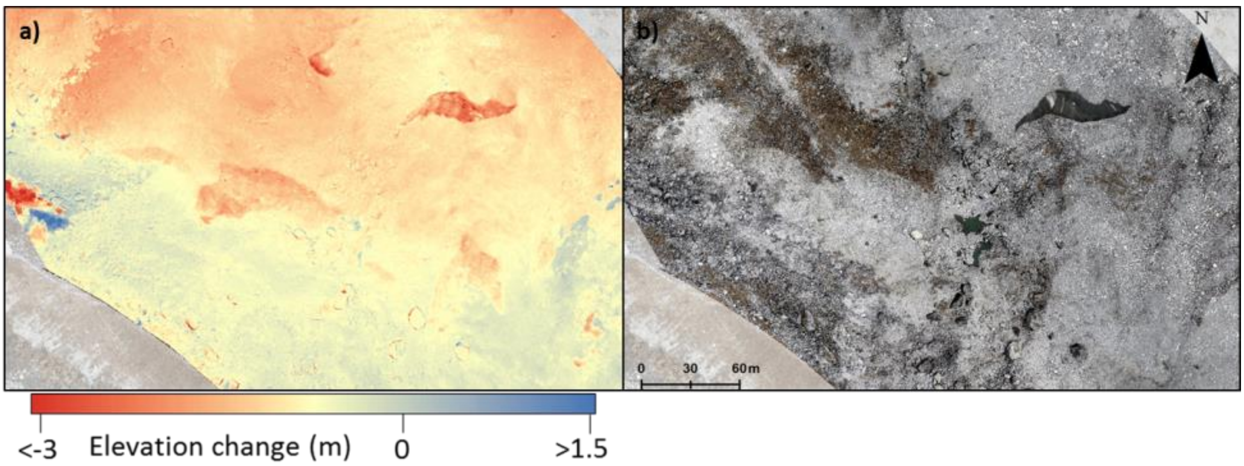

Figure 5.13: Region of surface lowering near the location of the new lake. a) M14-O13 difference DEM, b) M14 ortho-mosaic.

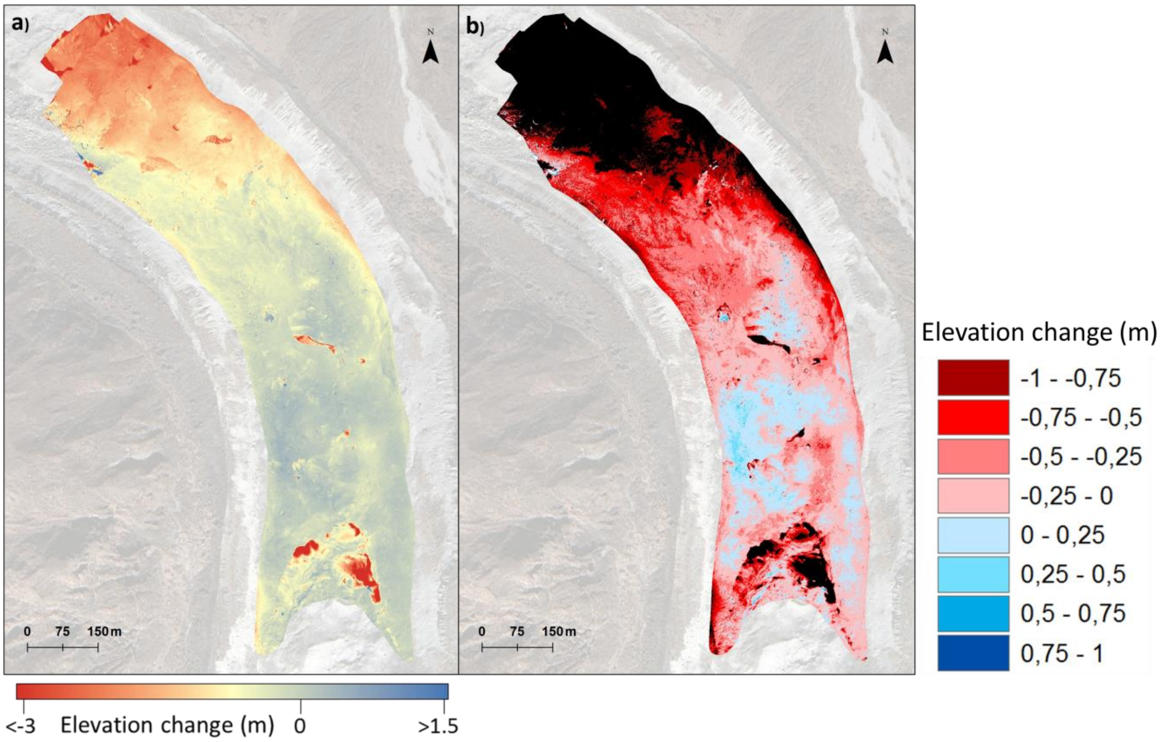

Figure 5.11: a) Difference DEM between M14 and O13. b) difference DEM showing only regions of surface rise or decrease within 1 m. Black areas denote >1m elevation decrease. *(See appendix F and G for full-page versions).*

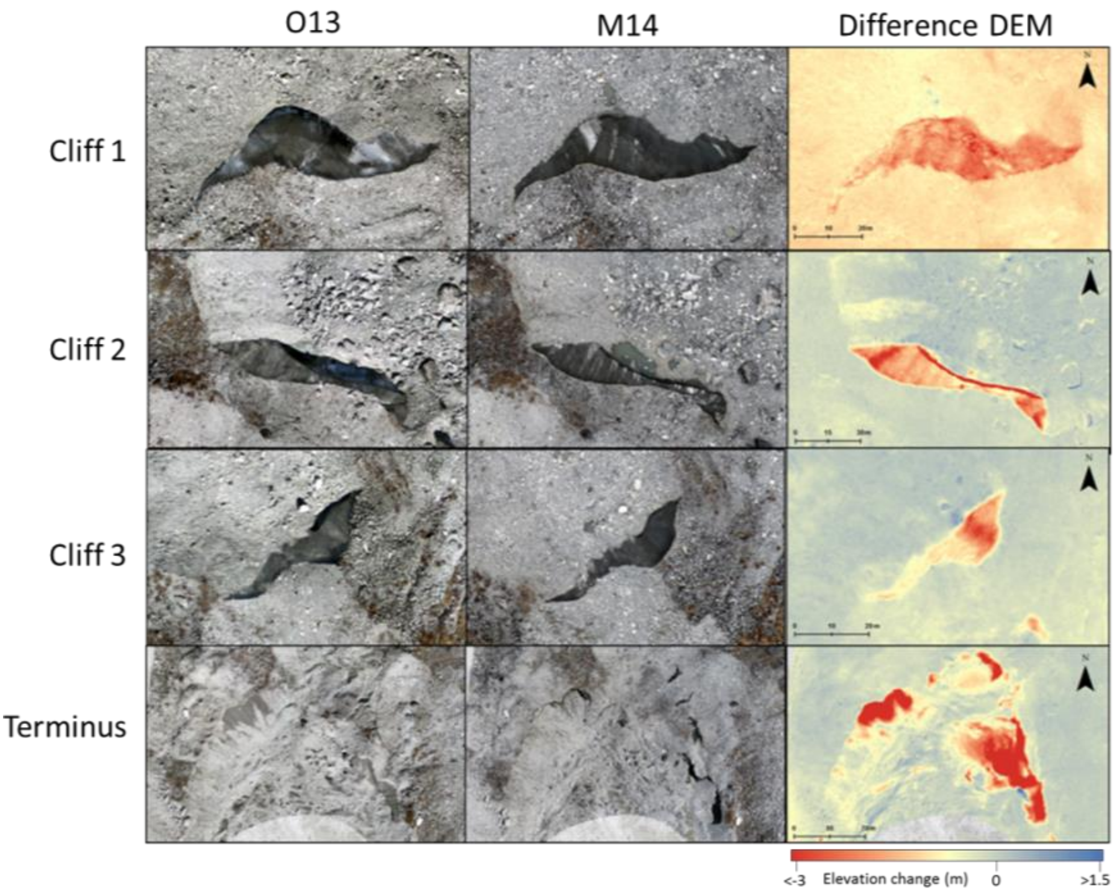

Figure 5.12: Right panels: Difference DEM close ups of cliff 1, 2 and 3 and the terminus. The left panels show ortho-mosaic close-ups of October 2013 and May 2014. In the bottom panel can be seen that even though the cliff surface area seems to have disappeared over winter, there was still substantial surface lowering.

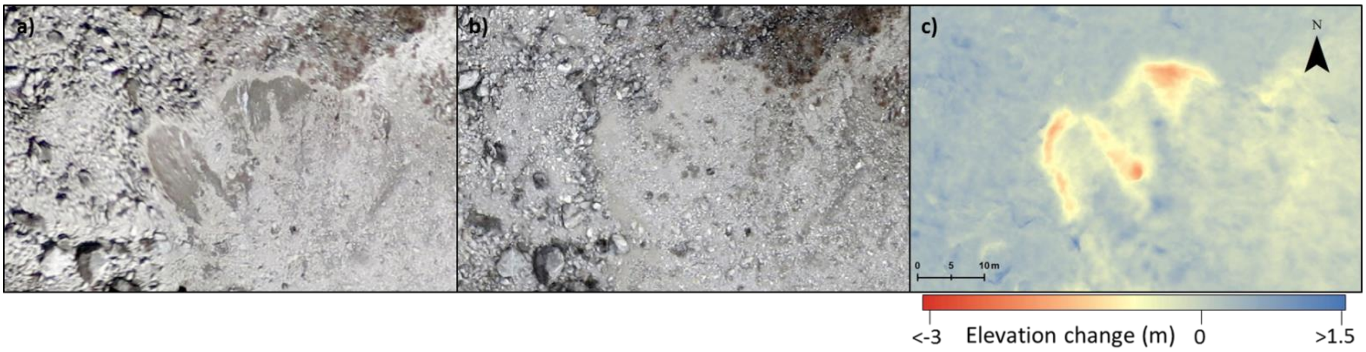

Figure 5.14: a) Part of October 2013 ortho-mosaic. b) The same area in May 2014, without the ice. c) M14-O13 difference DEM of the same area.

5.2.2 Mass change between October 2013 and May 2014

The observed elevation changes were converted to average melt and mass loss. Based on the M14 difference DEM (average surface lowering of 0.63 m over 0.45 km^2) the total ice loss over the observed period of 190 days is approximately $2.8*10^5 \pm 3.5*10^5$ m^3. Assuming an average ice density of 900 kgm^{-3}, this equals about $2.6*10^5 \pm 3.2 *10^5$ m^3 or 0.016 ± 0.019 m^3s^{-1} (3.0 ± 3.7 $mmday^{-1}$, mean water equivalent (m.w.e.)) of meltwater generated. The downwasting around the terminus is more substantial, averaging around 4.5 ± 2.2 $mmday^{-1}$, m.w.e. It was expected that around the ice cliffs mass loss would also be greater than average, but was not observed from the difference DEM. Only the cliff surfaces stand out. Cliff 1 (800 m^2 surface area) and Cliff 2 (~1000m^2) show average mass loss of about 18 ± 2.5 $mmday^{-1}$, m.w.e. Cliff 3 shows lower downwasting rates, of about 6.1 ± 3.0 $mmday^{-1}$, m.w.e. When also taking into account the surrounding area of the cliffs the average per unit area downwasting decreases substantially, to 5.9 $mmday^{-1}$ for Cliff 1, 1.7 $mmday^{-1}$ for Cliff 2, 1.2 $mmday^{-1}$ for Cliff 3 and 3.2 $mmday^{-1}$, m.w.e. for the terminus. Cliff 1 is in a region of large average downwasting rates, therefore the average downwasting remains relatively high. The fact that the surrounding area of the cliffs lowers the average downwasting is also observable from the figure 5.11, showing surface rise in front of the cliffs.

Even though cliffs only made up about 0.5% of total observed surface area, they contribute about 17% to total surface melt. The lakes on the other hand do not seem to contribute any extra to total surface downwasting. In the difference DEM they are actually visible as regions of relative surface elevation: in figure 5.15a a close up of lake C is shown. In the figure it is visible that the lake itself appears to have experienced surface rise. Still, the on average surface elevation change of the lake and its immediate (± 1m) area remains negative(-0.02 ± 0.4m).This is also visible for lake B (figure 5.16), which has formed during winter. The lake in front of Cliff 2 also shows an apparent surface rise, beside the fact that it has expanded somewhat eastward.

The contribution of the calculated melt water to total catchment runoff is likely minimal. Immerzeel et al. (2014) state that during summer, the melt water only constituted about 2% of the average runoff generated for the Lirung catchment. Likely the amount of melt water calculated in this study will not deviate much in total runoff contribution. The contribution to runoff of the entire Langtang catchment is even smaller. Discharge measurements at the Kyanging Base Station for winters between 2000 and 2006 show average runoff between 2 and 3 m^3s^{-1}. The meltwater calculated for this winter (0.016 ± 0.019 m^3s^{-1}) therefore constitutes about 0.5-0.8% of total discharge.

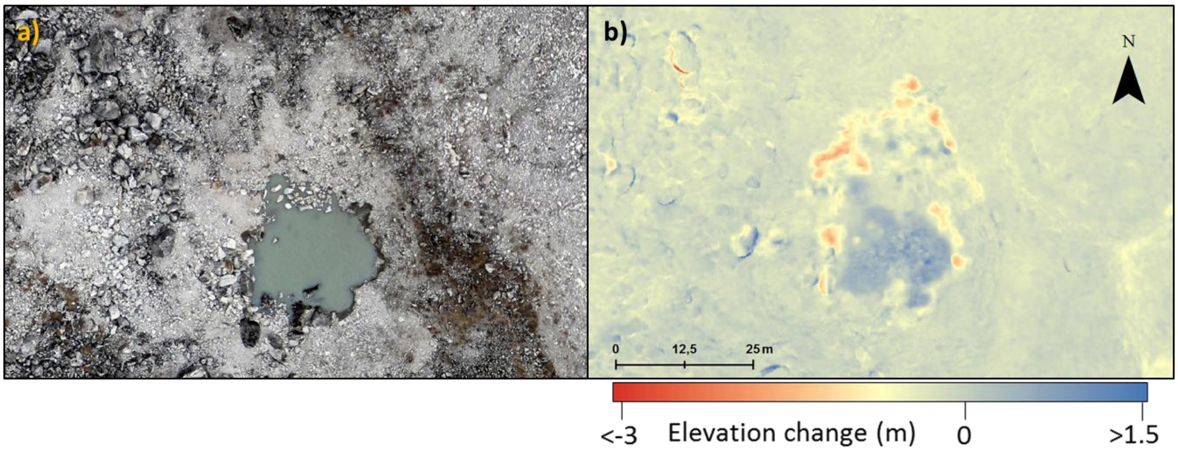

Figure 5.15: Lake C and its elevation change during the winter between O13 and M14. a) Ortho-mosaic of M14, b) M14-O13 difference DEM.

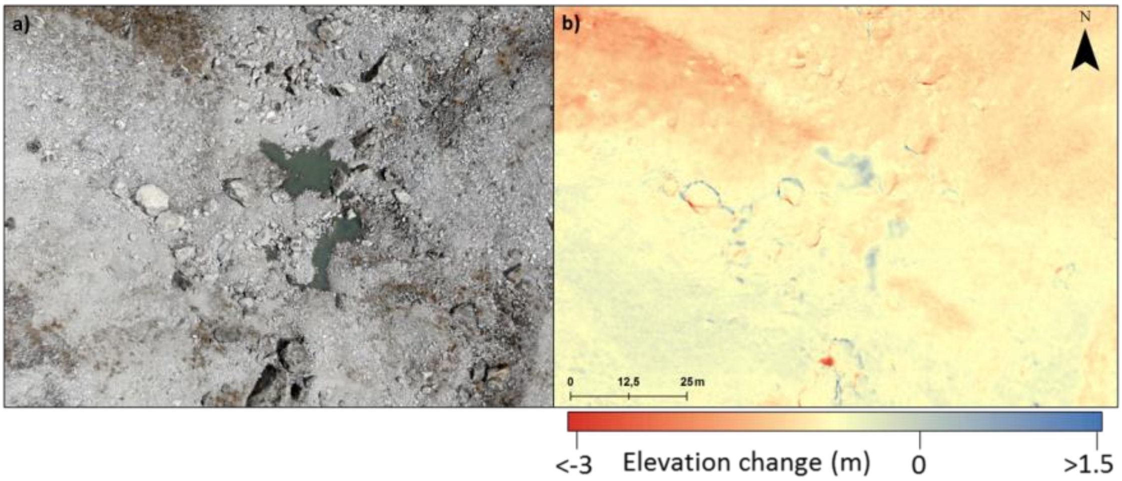

Figure 5.16: Close up of lake B, and its apparent surface rise during the winter between O13 and M14. a) Ortho-mosaic of M14, b) M14-O13 difference DEM.

5.2.3 Comparison to elevation and mass changes between May 2013 and October 2013

Even though it is already apparent that the M14 results are likely not entirely correct, a general comparison between the M14 and O13 DEMs could still be performed. In figure 5.17 the difference DEMs of the period over summer and over winter are shown (see appendix F and H for full-page versions). It is visible that considerably more changed during summer than during winter, as was also visible from the ortho-mosaics. Even taking into account the inaccuracies associated with the M14 results, the difference is still remarkable. Maximum elevation decreases of up to -14 m occur on cliffs over summer while this only reached -3 m in winter. Even though the changes over summer are much more pronounced the locations of change remain largely the same. Again especially the cliffs and the terminus are areas of increased change. In both difference DEMs the region of surface lowering to the northwest of Lake B is visible. The apparent surface rise in the outer curve is also visible over both seasons. An observed difference is that over summer the upper and lower parts of the glacier tongue both show comparatively equal rates of lowering, while over winter surface lowering rates gradually decrease. Additionally, there appears to be much more spatial variation in elevation change over summer than over winter.

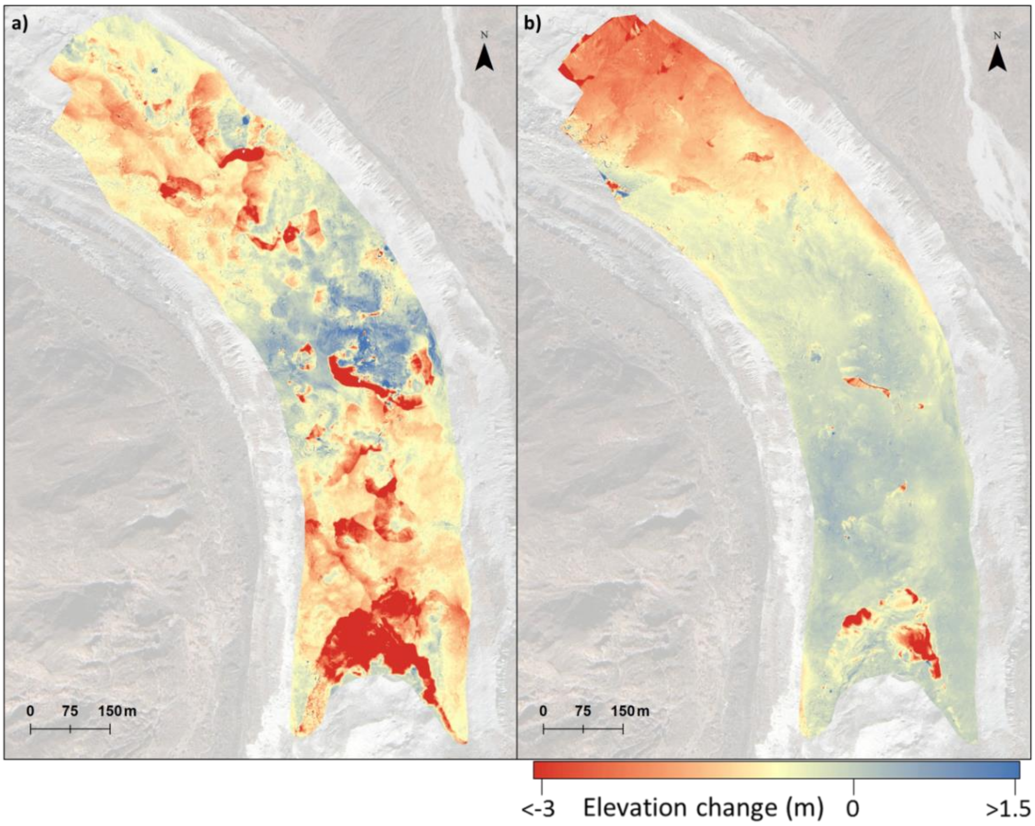

Figure 5.17: a) Difference DEM between May 2013 and October 2013 *(Adapted from: Immerzeel et al., 2014)* *(See appendix H for full-page version).* b) Difference DEM between October 2013 and May 2014.

The difference in spatial variation of downwasting has been made more clear in figure 5.18 (see appendix G and I for full-page versions) , where the summer difference DEM has been displayed using the same scale as figure 5.11b. In figure 5.19 (appendix J for full-page version) more elevation classes have been added, emphasizing the greater spatial variation occurring over summer, in contrast to the relatively homogeneous and gradual surface change over winter.

6. Discussion

In the following section the results presented in the former chapter shall be discussed, both in relation to the processing approach and in relation to other studies available in literature. The processing line and uncertainties that arose during the process will be evaluated. Possible causes that might lead to deficient results shall be presented, together with various options to improve the processing. This will be followed by an evaluation of the results and a reflection to other studies.

6.1 Processing

Considerable difficulties arose during processing. The constructed difference DEM showed elevation changes of up to 1 meter in off-glacier area (figure 6.1, see appendix K for full-page version), which is very unlikely. It appears that the middle and western sides of the DEM has mainly risen while the eastern parts have mainly decreased in elevation, leading to suspect distortion of the DEM. Also, the upper area of the glacier is located at the edge of the area covered by the UAV images. This makes this area of the DEM vulnerable to distortions, since edges of 3D models can often not be adequately

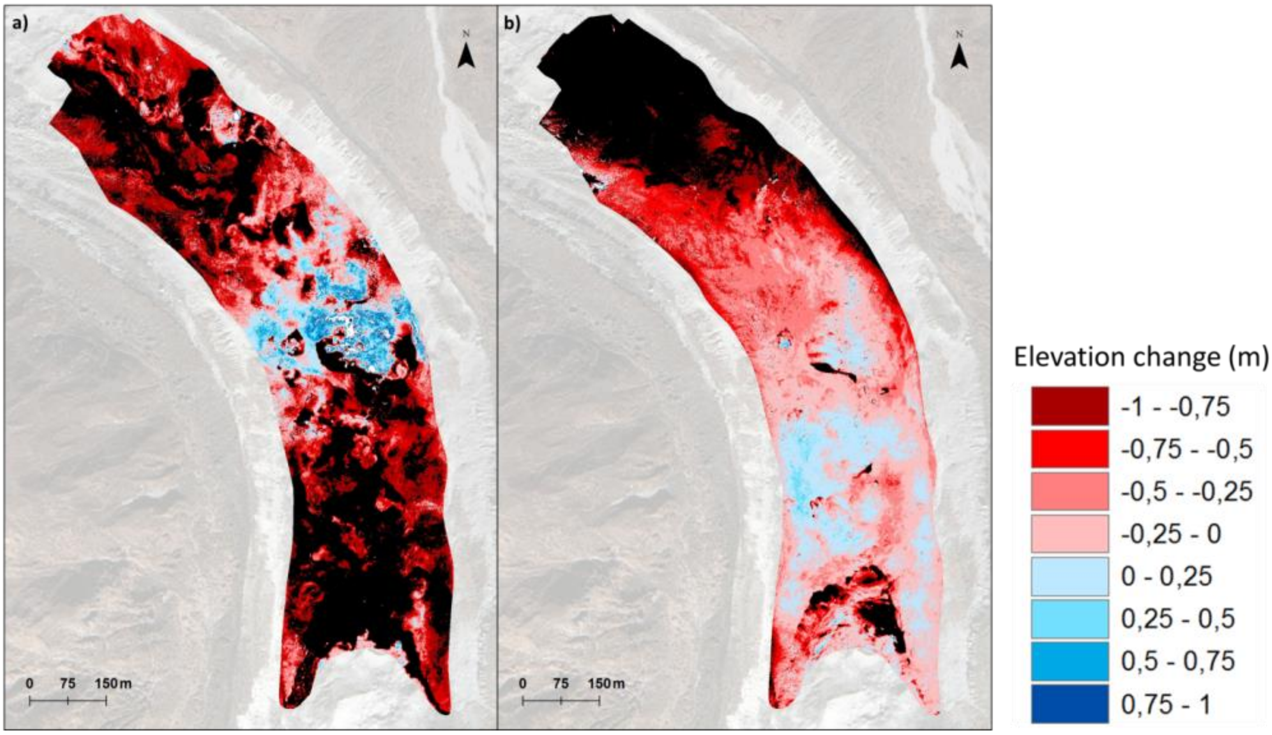

Figure 5.18: Elevation change, scaled with +1 and -1 m. a) Difference DEM of period between M13 and O13 (summer) *(Adapted from Immerzeel et al., 2014)(See appendix I for full-page version).* b) Difference DEM of period between O13 and M14 (winter).

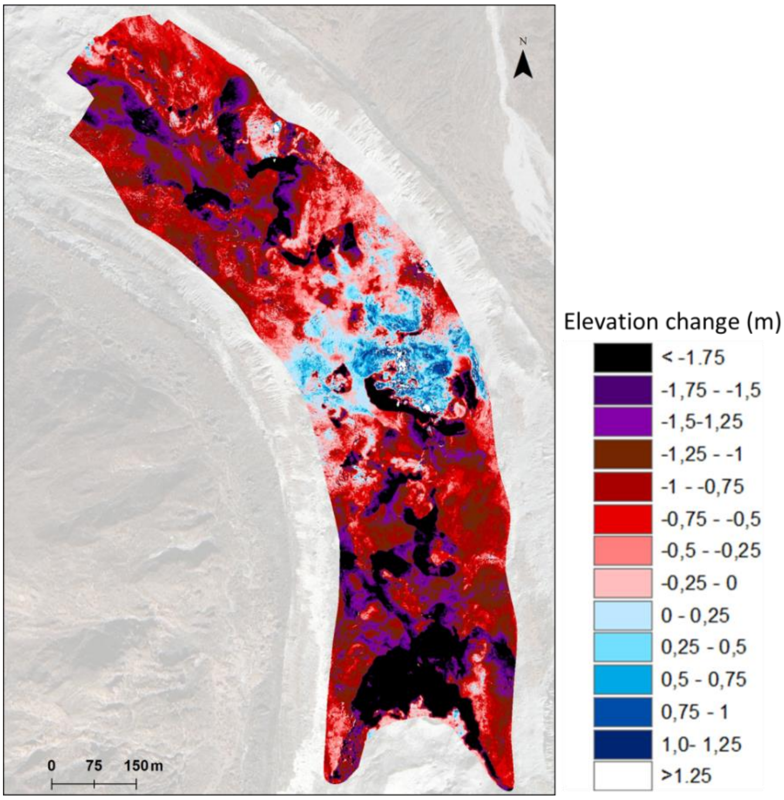

Figure 5.19: Difference DEM of period between M13 and O13 (summer), up to between -1.75m and 1.25 m *(Adapted from: Immerzeel et al. (2014) (See appendix J for full-page version).*

reconstructed in the SfM process. Using statistical methods (e.g. spline) to correct the outer glacier areas was not a feasible option, since this might lead to other unknown deformations on the glacier surface. Therefore the DEM resulting from the processing of the May 2014 images should be considered as reasonable approximation of reality. The main reason of the deficient DEM is likely the fact that the image set was of insufficient quality for PhotoScan to process adequately. Especially the photos of the upper glacier area caused difficulties in processing. This likely has resulted in a poor 3D representation of the scene.

There are several possibilities that could lead to miss-alignment of photos and failure to reconstruct geometry. According to the PhotoScan manual, the most likely causes of failure are insufficient photo quality due to e.g. lack of contrast or motion blur, or insufficient overlap of photos (Agisoft, 2014). To see whether this was the case for the M14 set, the images have been inspected and compared to the M13 and O13 image sets.

6.1.1 May 2014 image set

Since the specific algorithms Photoscan uses are not available in detail, the true reason why certain photos are inadequate, while others are not, is difficult to find out. Image quality is mainly determined by the camera and its settings. The main camera settings are focal length, aperture, ISO and shutter speed. Focal length determines how much of the scene will be captured, and the magnification of the scene. A longer focal length results in narrower scenes and larger magnifications. Aperture determines depth of view, or the range of distances at which object appear sharp (Nikon). ISO determines light sensitivity, with higher ISO values meaning a greater sensitivity to light. Too high or low ISO values might lead to over and under exposure of your images respectively. Shutter speed determines the duration of the image capture, and is especially important in situations where the camera is moving relative to the object. The combination of focal length, aperture, distance to object etc. determines the resolution of an image.

Photoscan recommends the following when capturing images that one wishes to process into 3D models (Agisoft, 2014):

- Images are preferably taken at the highest possible resolution
- ISO should be set to the lowest value. Higher ISO values might lead to unwanted noise in the image, which hampers the alignment procedure
- Aperture should be set so that the depth of view is high enough (thus, large apertures). Shallow depth of view can lead to blurred photos
- Shutter speed should be as low as possible, to prevent blur due to camera movement.

Additionally, shooting 'in raw' is recommended. This means that no image compression process (e.g. into JPEG format) occurs. This compression causes loss of data, and might produce extra unwanted noise (Agisoft, 2014). Also, shooting in raw allows post-capture processing of the image, for instance re-adjusting the white balance (which determines the color of neutral colors). In the case of UAV imagery, there has to be a trade-off between all the above settings. Under- or over-exposure of images for instance can be a large problem, since this lowers contrast, and therefore hinders object recognition. When forced to choose between under or over-exposure, under-exposure might be best since that preserves contrast more than does over-exposure, and PhotoScan requires contrast for adequate feature recognition. Also, underexposed photos are likely better than correctly exposed but blurry. Naturally there are additional factors which determine the quality of an image taken from

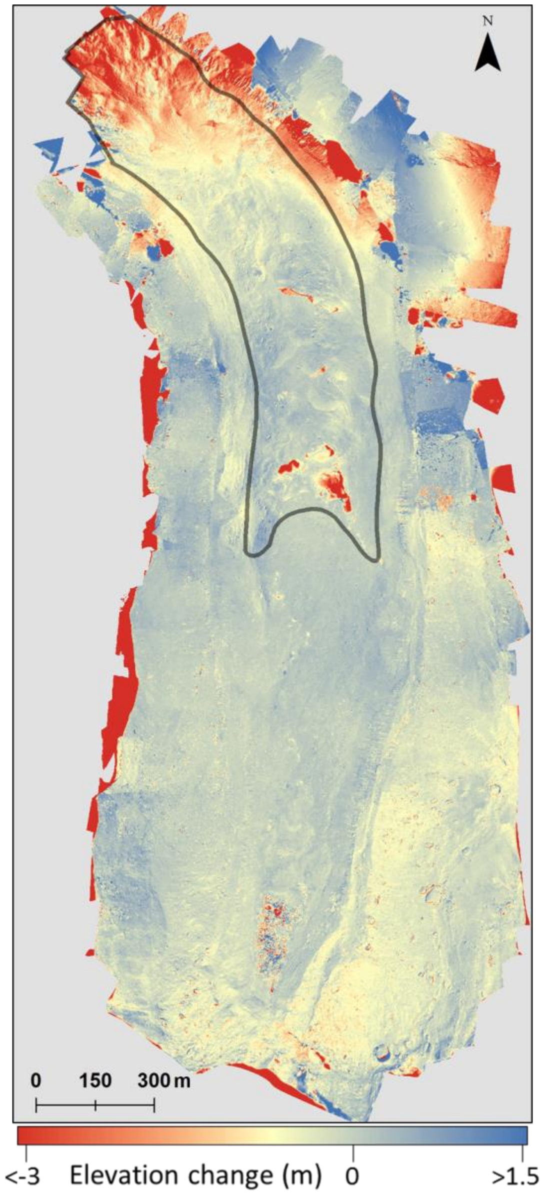

Figure 6.1: Winter difference DEM of entire glacier. The outline of the ice is provided in black. Notice the large elevation changes in the outer glacier area. The large elevation lowering at the outer edges are likely edge-effects introduced by the SfM procedure. *(See appendix K for full-page version).*

a UAV, such as the stability of the aircraft, the auto-focus function the camera uses, the light quality (a cloudy or sunny day) etc. (http://theuavguy.wordpress.com/). As stated in section 4.2, the Swinglet CAM (used for the M13 and O13 campaigns) was mounted with a Canon IXUS 125 HS camera, and the eBee (used for the M14 campaign) with a Canon IXUS 127 HS. Both cameras were set in full auto mode, with a fixed focal length of 4.3 mm. In full auto mode the camera autofocusses based on the prevailing light conditions. In adequately light conditions this mostly results in images captured with relatively large apertures, ISO values ranging between 100 and 250 and shutter speeds between 1/320 and 1/1250s. These settings should results in sufficient quality photos. In all three field campaigns the camera was set at full auto mode so there is no reason to suspect they caused the problems for the M14 dataset.

PhotoScan features a built-in quality check based on which images can be excluded from the dataset. This is a figure between 0 and 1, representing blurred and sharp images respectively. The quality is estimated based on the contrast between pixels in the image, with a larger contrast leading to higher image quality. Images with qualities of 0.5 or lower should be removed provided enough image overlap remains. Unexpectedly, no image of the M14 dataset had values that indicated removal was necessary. The quality did not differ much from the M13 and O13 images (table 6.4). Still, ISO, Shutter Speed or Aperture settings between the different image sets and flights within the M14 dataset were inspected for any notable differences. There was not a considerable difference between the three flights of M14. Aperture was on f/2.7 for all flights, which causes a small depth of view and could cause blur for distant objects. The average ISO values of flight 3 were somewhat higher than the other two flights, and shutter speed was consistently lower in flight 3 than in flight 1 and 2. This might be a reason for the alignment troubles. The images from O13 taken over the same area also had relatively low shutter speeds and higher ISO values however. Overall, the M13 and O13 images feature consistently lower shutter speeds than in M14. M13 and O13 aperture was smaller, providing a larger depth of view and potentially compensating the high ISO and low shutters speed values. However for some M14 imagery the same aperture setting was used as in O13 and M14. Since any differences that occurred between the image ISO, shutter speed and aperture are so small, it is considered unlikely that this is the reason for the failed alignment of the M14 images.

The only truly great difference between the O13 and M14 image set is the fact that the sun was shining in October. This might improve image alignment by PhotoScan, because sunlight increases contrast and the intensity of bright areas in images. However, in May 2013 the sun did not shine either so the miss-alignment is likely also not caused by (lack of) sunshine.

A factor that might have been of influence is the faster flying speed of the eBee compared to the swinglet Cam. This might have increased the so-called non-radial distortions for the M14 imagery, compared to M13 and O13. Non-radial distortions often result from 'rolling shutters'. When a camera is moving relative to the object it is shooting at the moment the image is taken means that the shutter is open while the camera moves, causing a so-called rolling shutter effect. Not only might this produce blurring or smearing effects, but also various distortions of the images, e.g. compression or stretching. While PhotoScan does correct radial distortions in the camera calibration procedure, these non-radial distortions are not modelled, producing poor results for 3D reconstruction (Agisoft Tech Support). This could thus be a reason for the difficulties during processing. However since the problem only occurs in the upper region of the glacier, it is likely not the only cause.

It could also be possible that the flights of May 2014 were suffering of instability issues, leading to distorted images or feature recognition issues. Average roll and yaw of the images was compared for 2013 and 2014 (table 6.1 and 6.2). As can be seen in the tables, a clear difference that might explain the problems with M14 is not visible. The roll and yaw data accompanying the photos

Table 6. 1: UAV pitch for the three image dates, as recorded in the image data *(*Source: Immerzeel et al., unpublished).*

Project	Mean	Min-Max	StDV
May 2013*	6.17	-21.50 - 17.59	4.45
October 2013*	6.94	-28.30 - 19.79	3.73
May 2014	4.36	-5.15 - 11.90	2.83

Table 6.2: UAV roll for the three image dates, as recorded in the image data *(*Source: Immerzeel et al., unpublished).*

Project	Mean	Min-Max	StDV
May 2013*	-1.00	-30.64 - 20.19	5.50
October 2013*	-0.93	-21.00 - 15.02	3.82
May 2014	-0.31	-17.86 - 19.37	6.93

is a snapshot of the longer process of image acquirement and might therefore not be representing the motion of the UAV entirely correctly. However it can still be used as an approximation of flight stability, and based on this there is not a discernable difference possibly causing the alignment problems. Flight instability might also cause the UAV to skip taking certain photos if the instability is too severe. Distribution of the images is a very important factor determining the quality of the 3D reconstruction. The PhotoScan manual states that at least 60% overlap is required to produce sufficient quality results (Agisoft, 2014). In all campaigns, the desired image overlap was set to 60% in lateral and 70% in longitudinal direction for each flight. Due to unknown reasons this overlap was not reached in third flight of the M14 campaign, and likely resulted in the problems that occurred during processing. A potential cause are gusts of wind causing the UAV to wobble so much that the camera did not take pictures at the appropriate intervals. This instability cannot be retraced in the image data, since no image was taken at those times. Severe flight instability and the skipping of image acquirement might be the cause of the low amount of photos and thus overlap in the upper area of the glacier tongue.

6.1.2 Attempting improvement of the 3D reconstruction

Since it is unlikely that a perfect set of images is always acquired, there are possibilities to 'help' PhotoScan during processing. As stated, it is likely that lack of overlap on the photos is the problem. However in order to eliminate other possible causes, various attempts have been made to improve the results of the 3D reconstruction (table 6.3). A complete accuracy assessment was not performed for every project run. Instead, model quality was assessed by visual inspection of the ortho-mosaic, and by differencing the resulting DEM with the DEM of May 2013. This difference DEM was then inspected for any anomalous elevation differences (e.g. 25 m) or any elevation change in the outer glacier area, which ideally would show no change in elevation at all. In the following sections these attempts will be presented. Firstly attempts with varying the input will be presented. This will be followed by a discussion of tries where the settings of PhotoScan were varied.

Table 6.3: The various options tried to improve model results

	Retries concerning	Variation
Input	Image input	Adding extra May and October 2013 images Only processing flight 1 and 2 of May 2014
	Re-alignment of images	With additional tie-points Without additional tie-points
	Omitting camera coordinates	Non-aligned images Flight 3 Entire image set
	Georeference markers and manual tie-points	Removing markers based on reprojection error Adding additional markers
Settings	Sparse cloud generation	Varying feature point limit per image
	Dense cloud generation	Varying quality settings from low to high
	Mesh generation	Varying polygon face count
	Editing	Manual removal of outliers in point cloud(s) Removal of outliers based on reprojection error Optimization iterations Editing anomalous mesh

Varying input

Images

The recommended first option to improve model results is to remove poor quality images (Agisoft, 2014). The quality check did not indicate removing any photos was necessary, since the lowest quality photo of this series was 0.6. Moreover, deleting any images was not a feasible option because there already was a shortage of images to reach the required overlap of 60%. Improvement of the 3D reconstruction was therefore attempted by adding more off-glacier imagery of May and October 2013, since the May 2014 flight lack sufficient off-glacier photos. This increased off-glacier image coverage, but the DEM of the glacier tongue itself did not improve. To see whether the images of the upper glacier area were the main cause of the problems a DEM with just the images from flight 1 and 2 was made, covering d the middle and lower area of the glacier tongue. It appeared that this DEM indeed showed some less extreme values in elevation change, but there was no other clear improvement. The elevation change values on the glacier itself also changed. In some locations it gave smaller elevation change values than the model using all three flights, but in other the change were larger. Therefore no other attempts at DEM creation without flight 3 were taken. More so since the area that flight 3 (should have) covered is actually the area of greater interest on the glacier.

Alignment

If the initial feature recognition process of PhotoScan fails, an option exists to re-align a certain selection of images. Photoscan then uses the matches and marker positions, found during the initial alignment phase, to estimate the locations of the selected non-aligned images. This can be done with or without the manual assigning of additional tie-points on congruent photos. The tie-points basically 'tell' the program that those points are the same. This re-alignment has been attempted both with and without extra tie-points and for image subsets of various amounts.

Camera orientation

Another potential cause of the problems was that the camera orientation parameters (coordinates, pitch etc.) included in the image data were faulty, possibly causing errors in the alignment process. To check whether this was the case several attempts have been made in which coordinates were not taken into account during the alignment process. This basically means that images are solely aligned based on feature recognition algorithms (greatly increases computation time). This was attempted for the selection of missing images, the entire third flight and the entire image set.

Georeference markers

Tie-point and marker input has also been varied. Firstly, both manual tie-points and the O13 ortho-mosaic-based markers showing high placement errors were removed. Photoscan represents this error in meter and in pixels. The meter error is the distance between the input (marker position) and the estimated position of the marker. The error represented in pixels is the root mean square reprojection error, calculated over all the photos where the marker is visible. The reprojection error is formed when a 3D coordinate of a point is calculated based on its location on several 2D images. This 3D point is reprojected on these images, and the distance between the marked and the reprojected point in an image is the reprojection error (https://support.pix4d.com) (figure 6.2). The error depends on camera calibration and on the quality of the marked point on the image. This quality in turn is determined by the position at which the point is marked, and by the amount of zoom used during placement. A reprojection error of 0.5 basically means that the marker is only half a pixel off. In addition to removal of markers, 29 extra markers were generated on the moraine-slope. This was done in a similar way as the generation of the already existing tie-points, by sampling them from the ortho-mosaic and DEM of October 2013. Stationary objects or points (such as large

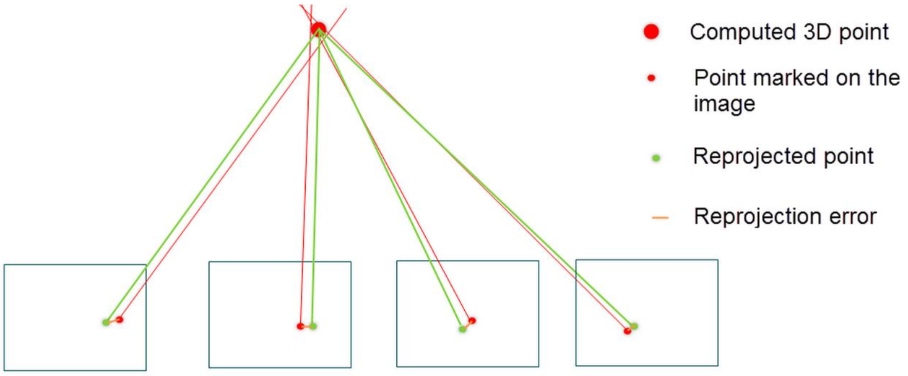

Figure 6.2: Reprojection error. *Source: support.pix4d.com*

boulders, or clearly distinguishable shrubs) were selected in the ortho-mosaic, and cross-checked with the images of May 2014, to see whether they are clearly visible.. Several points were selected that way, and subsequently used in the processing. The points were placed along the moraine wall, keeping the points as evenly distributed as possible.

For all of the above project variations the resulting DEM did not show any improvement.

Varying settings

Several of the above run variations have also been tried with different quality settings of the program. The quality can be changed for the initial alignment (resulting in the sparse point cloud), for the dense cloud and for the mesh.

Sparse cloud generation

The alignment quality can by influenced by changing the number of feature points PhotoScan tries to construct. This number indicates the upper limit of feature points on every image to be taken into account during processing (Agisoft, 2014). In principle, setting a higher upper limit will improve the accuracy of the alignment. However, based on the Agisoft User Forum, this is not so straightforward. A user stated that sometimes setting a lower point limit showed better results than a higher one, though at other times this proved to not be the case. An explanation for this occurrence has not been found, so the upper limit of the feature points has been varied for several runs.

Dense cloud generation

Dense cloud settings could be varied from low to ultra-high. This basically means whether full size images or down-scaled versions are used during the processing. Settings had at first been varied from low to high. No visible improvement of the resulting DEM occurred, therefore it was not deemed necessary to try the ultra-high settings.

Mesh generation

The quality of the mesh is mainly determined by its polygon (or face) count. A low face count results in a rough mesh, while higher number of faces results in greater detail of the 3D model. Very high settings result in visualization problems due to the high graphical requirements, thus there was a limit in the quality of the meshes that could be feasibly varied with. In any case, very high mesh settings would not be of extra merit since the debris on the glacier would be represented in great detail, while this was not the object of this study.

Editing

The point clouds and mesh could be edited in-between processing steps. After alignment the resulting point cloud and estimated camera parameters can be optimized based on the now-known reference coordinates of the markers. Often georeferencing is improved considerably after optimization. The sparse point cloud can also be directly edited by removing obvious outliers, and should be done before optimization. This can be done by manual selection and by a PhotoScan tool which selects points based on their reprojection errors. The user can set an error limit and remove the points that exceed that limit. According to the Photoscan tech-support, a project with an average reprojection error of larger than 0.8 is already quite inaccurate and an error less than 0.5 is almost perfect, and setting the selection threshold to a reprojection error of 1 is therefore advised. This was not a feasible option in this case since it would lead to the deletion of the entire point cloud. Therefore, the threshold was set so that up to a few thousand points were selected (which was also the suggested amount of selected points on the forums). After removal of the outliers optimization was performed, indeed resulting in lower average reprojection errors. Based on user advice, this process was repeated two times. Iterating more often would result in lower errors, but could result in ‘rippled’ models. Frequently, after three iterations the models had an average reprojection error of around 1 pixel, with maximum values varying between 3 and 30. These values were compared to the projects that created the DEMs of May and October 2013 (table 6.4). Since, the values did not substantially differ from each other, it was considered that high reprojection error is not the cause of the failure. Photo quality and effective overlap were also compared. Effective overlap is the mean number of projections of each point in the sparse point cloud. An effective overlap of 3 means that each point in the sparse point cloud is matched, or visible, in 3 images on average (Agisoft Tech Support). The values varied little between 2013 and 2014, therefore it was considered that a cause inaccurate 3D reconstruction likely did not lie in the image quality or program settings.

A final option is to edit the constructed 3D mesh. Constructed meshes often feature

Table 6.4: Model quality assessment values *(*Source: Immerzeel et al., unpublished).*

Project	Mean Reprojection Error (Max)	Photo Quality	Effective overlap
May 2013*	1.17 (28.58)	0.59-0.85	3.01
October 2013*	0.75 (20.60)	0.60-0.84	3.37
May 2014	0.97 (6.21)	0.61-0.87	3.55

Figure 6.3: Anomalies and holes in the mesh.

anomalies and/or holes (figure 6.3) which can be removed, thereby improving geometry reconstruction.

The variations of the processing explained above did not result in any notable improvement of the results. It should be noted that for the same project and project settings, the resulting DEM also varied. This is likely due to the fact that the 3D model is a result of SfM (which has several calculations and thus solutions) and optimization processes, which likely never have the same end-result (Agisoft Tech support). Therefore it was deemed unlikely that the deficient DEM was caused by any PhotoScan setting. Reprojection errors and efficient overlap of the M14 project were better than the M13 project, which was apparently successful. However, the reprojection errors and effective overlap figures PhotoScan provides are likely based only on the aligned imagery. Since the problems for the M14 imagery are most likely due to photos that do not align and are hence not taken into account, the effective overlap is not an entirely representative figure.

Conclusion

The most likely cause for the deficient DEM is the lack of overlap. Varying the input or quality settings has no substantial effects, and camera and other image parameters did not considerably vary from the O13 and M13 images. Lack of overlap can only be remedied by re-acquiring the images, which was not an option. Therefore it is strongly recommended for further field campaigns to ensure enough overlap of images. To make sure georeferencing is optimal, enough outer glacier area should also be covered so that enough markers can be placed. Additionally, it would be preferable to be able to have full control over the camera settings. The fact that the camera was allowed to shoot in full auto mode leads to varying colors and lighting, which will decrease the matching efficiency of the program. To prevent this it is advisable to shoot in raw, which allows the user to modify the colors in image processing software, such as Lightroom (Adobe). This might lead to an increased processing workload, however shooting in raw allows a bigger range of possible adjustments to the images which are not possible with jpeg or other file types.

6.2 Results

In this section the results presented in section 5 shall be further evaluated. First the accuracy assessment shall be presented, after which the results themselves shall be discussed.

6.2.1 Accuracy assessment

The geographic accuracy of the M14 ortho-mosaic was examined using control tie-points sampled from the O13 ortho-mosaic. Errors are introduced in the ortho-mosaic and DEM in various ways. Errors are inherent to the SfM workflow, due to the calibration and optimization algorithms, but also because of the manual input of the tie-points. The tie-points used in this research are sampled from the O13 ortho-mosaic, which in turn is subject to the precision of the dGPS system used to take GCPs, and to the errors introduced by processing. The dGPS system is reported to have ±0.20 m accuracy in x, y and z directions for the base station (Wagnon et al., 2013). The reported errors of the dGPS device for the GCPs for October are smaller than 15 mm, and hence considered negligible compared to the accuracy of the base station (Immerzeel et al., 2014). Compared to the O13 mosaic, the M14 one deviates by -0.023 and 0.051 m in the x and y directions respectively, with maximum displacements of 0.48 m and 0.75 m, minima of 0.016 m and 0.036 m of and standard deviations of 0.23 m and 0.31m respectively. Thus, the horizontal errors all fall within 0.75 m displacement, but the majority of the errors fall within 0.2 m (figure 6.4). The accuracy of the DEM has been similarly assessed: the average deviation from the O13 surface is -0.03 m, with maximum and minimum deviations of 1.2 and -0.94 m respectively, and a standard deviation of 0.50 m. The main part of the errors falls within 0.45 m however. These errors are considerably larger than those reported for the O13 and M13 DEM (Immerzeel et al., 2014). Especially the negative deviation is considerably larger. Immerzeel et al. (2014) reported horizontal and vertical errors falling within 0.25 m, averaging about 0.1 m in the horizontal and -0.1 m in the vertical. Therefore, these errors have to be incorporated in the accuracy of the May 2014 results. This leads to an error range between -0.75 and 0.69 m in the horizontal, and -0.98 and 1.2 m in the vertical. Compared to Immerzeel et al. (2014), the total error range of the new ortho-mosaic and DEM is considerably larger and more spread. Still, this is considerably better than reported accuracies for DEMs constructed by other methods. Aster DEM accuracy varies between 15 (low relief areas) and 60 m in glacierized areas with steep rock headwalls and large low-contrast accumulation areas (Racoviteanu et al., 2008). SRTM DEMs have reported error margins of 7 m average and 285 m at maximum (Kääb., 2005). Even with the large displacement error introduced by the various processing steps, the results are still promising. Observations and findings based on visual inspection of the ortho-mosaic are likely valid. A finding such as lakes appearing to be mostly present in depressions hold, and is not unlikely since ponds and lakes generally form in depressions (Röhl, 2008), and increased melt rates due to the water sustain these depressions.

6.2.2 Evaluation of results

The main finding of this research is that during winter, considerably less change occurred than during summer and that these changes were also less spatially heterogeneous . Even though exact numbers cannot be obtained, it is clear that cliff retreat and total downwasting rates were considerably less. This is most likely due to the fact that temperatures, and thus melt rates, are much lower during winter than during summer. Moreover, the period between M13 and O13 covers the wet summer monsoon, while the one between O13 and M14 covers the dry winter monsoon. The summer monsoon is a much more dynamic period in general, due to the unstable, moist air being transported from the Indian Ocean to the Himalayan range. Hence, due to the orographic lift precipitation rates

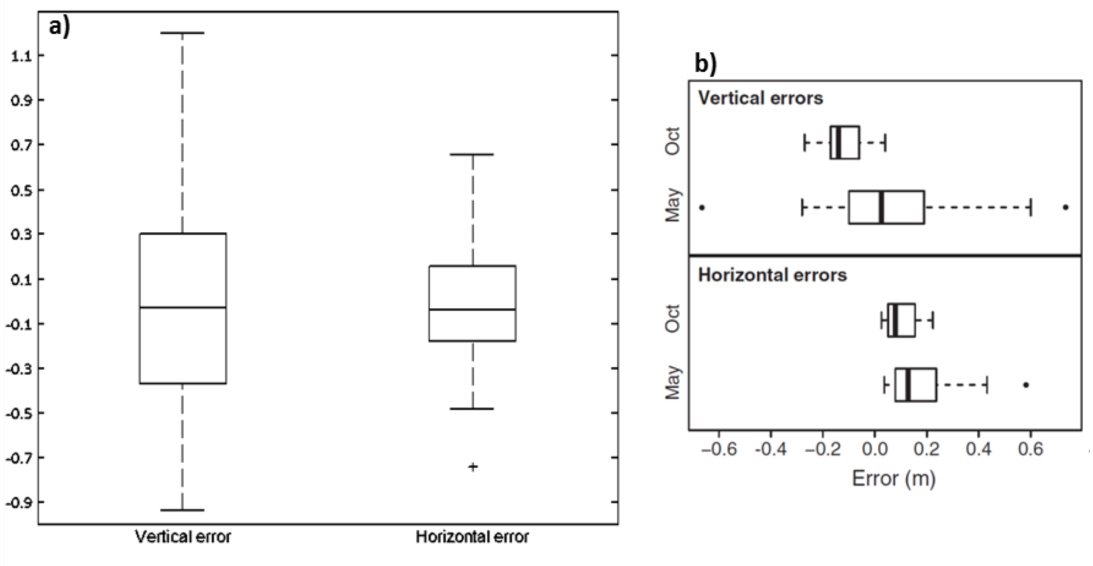

Figure 6.4: a) Error margin of the DEM and ortho-mosaic. b*) Error margins of May and October 2013, for comparison *(*Source: Immerzeel et al., 2014).*

are also much higher in summer. Since this precipitation mostly falls in the form of rain, this will increase melting rates. This rain can also explain the presence of many bare ice areas in O13 where there were none in M14. The ice was likely washed clean of the cover of debris by summer monsoon showers, and were covered again during the dry winter monsoon.

Surface features

The observations concerning the surface features likely due not suffer much from the errors explained above. The fact that cliff surface area was smallest in May 2014 is still a valid observation, even though the exact surface areas might not be correct. It would be interesting to see whether additional ice would again be exposed in October 2014, and covered again in May 2015, and whether the total cliff surface area would again have decreased compared to M14. Unfortunately, the UAV image acquisition that was planned for a field campaign in October 2014 could not continue, thus renewed exposure of ice cliffs cannot be determined. Further ice cliff evolution can be part of future research on this glacier.

The observations concerning the growth and shrinkage of supra-glacial lakes are also of interest. As was explained in section 2.4 conduits connecting the lake to the englacial drainage system may melt or otherwise open during summer, leading to the drainage of a lake (Röhl, 2008). Subsequently these conduits freeze again over winter. This likely explains why total lake surface area was smallest in O13. The fact that the Lake C did not empty over summer might simply be because the conduit did not open. The lake that appeared over winter (Lake B) is located near a relative depression. Any water which flows down over and through the debris or ice could have accumulated there. Which type of depression (location, size, shape) might lead to an actual lake, and how it would subsequently grow could be a topic of continued research on this glacier.

Surface flow velocity

The magnitude of flow velocity computed in this study is quite similar to those calculated by Immerzeel et al. (2014), who reported summer velocities between 2.5 m at the upper glacier tongue and near stagnancy at the terminus. It is questionable whether velocities would be the same over winter as over summer since other observations indicate that winter is a less dynamic period. Moreover, when comparing the flow field of Immerzeel et al. (2014) to the one produced here, the upper glacier area seems additionally doubtful. Both Immerzeel et al. (2014) and Naito et al. (1998) report upper glacier flow direction towards the east, while here it appears to be mostly northwest. Upstream flow is very unlikely, and is probably due to miss-construction of the ortho-mosaic and DEM, as explained above. Using statistical correction methods (e.g. spline) did not improve the results. The upper glacier area might show more realistic flow directions, but in those cases other areas of the glacier tongue showed anomalous flow directions. Still, when not considering the upper glacier area the entire glacier seems to be near stagnant, which is to be expected over winter. Naito et al. (1998) report velocities between 1.9 and 2.5 m for the lower part of the glacier over summers between 1994 and 1996, and velocities between 2.8 and 7.5 m in the middle. In contrast, here the middle glacier flow velocities do not exceed 0.5 m. The relatively larger flow velocities on the western side of the glacier compared to the eastern side might be due to increased avalanching coming from the west (Immerzeel et al., 2014) or by the fact incoming radiation from the sun is strongest from the southwest, leading to larger flow rates. These results presented here and those of Immerzeel et al. (2014) indicate that the flow has greatly decreased since 1996. It has also been shown that over during winter flow velocities likely decrease even more. Even though exact quantification of flow is not possible in this case, the results still show the great potential of the use of UAV in glacier research due to its high temporal resolution.

Downwasting

The difference DEM computed for the period between O13 and M14 can be considered a good indication of the fact that over winter, considerably less downwasting occurs than over summer. This can be inferred from the average elevation change, but especially from the differences in surface lowering around the cliffs. The difference DEM over summer shows a more spatially variable pattern of surface lowering, featuring many small regions of increased surface change. Still, the main areas of surface decrease which are visible in the O13-M13 difference DEM are also visible in the M14-O13 difference DEM, though less pronounced. The region of relative surface elevation in the outer curve, present in both difference DEMs, likely indicates emergence, also noted by Immerzeel et al. (2014) and Naito et al. (2002). Compression of the ice in the outer curve causes uplift of the glaciers surface, leading to emergence. Naito et al. (2002) estimate the emergence velocity of about 0.2 $myear^{-1}$, over the period from 1996 to 1999. Immerzeel et al. (2014) report surface rise of up to 0.5 m over summer, while the surface rise observed over winter barely passes 25 cm and covers a much smaller area. This is in itself not surprising, since the glacier shows less activity overall over winter. However, since surface rise also seems to occur over a considerable area in the lower region, and considering the error margin of the DEM, the calculated downwasting bears additional comment. The observed average surface lowering of 0.63 m over an area of 0.45 km^2, corresponds to average downwasting of 3.0 ± 3.7 $mmday^{-1}$, m.w.e. during the observed period. Immerzeel et al. (2014) computed an average surface lowering of 1.09 m over 0.49 km^2, and calculated the average downwasting over summer to be around 6.3 $mmday^{-1}$, m.w.e., also assuming an average ice density of 900 kgm^{-3}. Based on the dissimilarities between the two difference DEMs (figure 5.17), one would expect a larger difference in total downwasting. However, emergence causes an apparent mass gain in the downwasting calculation due to the surface rise associated with it, and leads to erroneous downwasting rates. Since surface velocity of the glacier tongue is very low, the error associated with this emergence is likely small. Still, the fact that emergence is more substantial in Immerzeel et al. (2014)'s difference DEM than in the one produced here might be the reason of the relative small difference in downwasting rates. Naito et al.(2002) report annual average surface lowering ranging from 1 to 2 $myear^{-1}$ during the period from 1996 to 1999. Combining the downwasting rates calculated by Immerzeel et al. (2014) and the one in this study gives a total average surface lowering of 1.72 m over one year. This falls within the range provided by Naito et al. (2002).

Additional uncertainty concerning the downwasting arises from the unknown contribution of avalanches, snow and rain on any mass gain. As stated in section 4.1, the glacier tongue only gains mass by avalanches and intermittent precipitation, and most of this precipitation falls during the summer monsoon (Immerzeel et al., 2014; Ageta and Higuchi, 1984). How much avalanches contribute to mas gain is difficult to research due to the dangers involved researching them, and due to their unpredictability (Benn and Lehmkuhl, 2000). The apparent surface rise below the middle of the glacier could be due to the errors introduced in the processing, but very small increases in mass of a glacier are not impossible over winter. Still, since the upper part of the glacier tongue (lying at higher elevation) shows significant downwasting, sudden increases in mass at lower elevation is unlikely. It could also be a delayed signal of mass increase, slowly making its way down-glacier, but some indication would have been already present in the difference DEM of Immerzeel et al. (2014), which is clearly not the case. Alternatively, it could be that a localized snow avalanche covered this lower part of the glacier, leading to a relative increase in surface.

The contribution of ice cliffs to downwasting was also examined, and it was shown that even though the ice cliffs only make up 0.6% of the total surface area, they contributed to about 17% of total melt. The large downwasting rates of the cliffs is likely due to backwasting. Cliffs retreated up to 2.5 m on the glacier body, and up to 6.5 m at the terminus. This is less than was observed over the summer period Immerzeel et al. (2014), and can be explained by the general decrease of activity that has been noted. The cliffs at the terminus showed the largest retreat rates in both summer and winter. Likely the terminus cliffs have retreated farther since they are facing southwest, in contrast to the generally northward facing other cliffs. The largest amount of sunlight (and thus, radiation) comes from the southwest, leading to enhanced backwasting rates (Sakai et al., 2002). The reason that south-facing cliffs on the rest of the glacier tongue (mostly only visible in the O13 ortho-mosaic) are few and small in number is also due to this incidence difference. As was stated in section 2.4, cliffs facing southwest generally have gentle slopes, small surface areas and tend to disappear (Sakai et al., 2002). The low slope angles also facilitate the observed re-coverage by debris over winter. Reid and Brock (2014) assessed ice cliff backwasting on the Miage glacier in Italy, and noted retreat rates of 61-75 $mmday^{-1}$, which would correspond to 12-14 m of retreat during the 190 days observed in this study. The values of Reid and Brock (2014) are much larger than observed here, but their observation periods cover several days in June. Air temperatures were likely higher than on the Lirung glacier during the winter period, causing the relatively large retreat rates. The values stated by Reid and Brock (2014) are instead more similar to those reported by Immerzeel et al. (2014), who observed the Lirung glacier over summer. Over their observed period of 154 days, the retreat rates would correspond to 9.4 to 11.5 m of retreat. These values are very close to the 7-11 m reported by Immerzeel et al. (2014). The observed contribution of the ice cliffs to total melt is far less than reported in Sakai et al. (1998), who state a 2% surface area coverage and a contribution of 69% of total melt. However, up-glacier of the observed area the glacier surface has a higher density of cliffs and lakes, possibly explaining part of this difference. Immerzeel et al. (2014) report 8% total ice cliff and lake area and a contribution of 24% to total melt. The percentage melt is more in the range of values found in this study, but there is still a relatively large difference in areal coverage. This might be due to the fact that in O13 more bare ice was exposed than in M14, which became covered by debris again over winter. In addition, Immerzeel et al. (2014) combined the surface areas of lakes and cliffs and their observed area was lager, including a large cliff-lake complex that is not included in the area observed for this thesis. Reid and Brock (2014) calculated ice-cliff contribution total melt on the Miage glacier. They state that 7.4% of total ablation is due to ice cliff melt, while they only constitute 1.3% of the observed glacier surface. They also note the difference to the calculations of Sakai et al. (2008) and state that it is likely due to differences in ice cliff number and distribution per unit area, and due to the fact that the debris cover of the Miage glacier is thinner. A thinner debris cover reduces melt rates less, indirectly lowering the relative contribution of ice cliffs (Reid and Brock, 2014).

Immerzeel et al. (2014) also report additional contribution of the lakes to total surface melt. This is expected since water absorbs more heat than ice does, thereby increasing melt rates (Sakai et al., 2000). However this was not as apparent in the difference DEM created in this study. Instead the lakes appeared to be regions of surface elevation increase. However this might actually just the water surface rising due to the continuous filling up of the lakes. Whether lake levels indeed rise over winter could be topic of further research. Another possible reason that lakes did not contribute as much to total surface melt over winter as in summer is that they were frozen over in winter. The ice-surface would then reflect, instead of absorb, much of the incoming solar radiation. If the frozen lakes were additionally covered by snow the reflectance would be even higher, decreasing heat absorption further. The exact way ice cliffs and lakes contribute to localized surface melt could be researched by examining them in higher detail. This could be done by e.g. in-situ measurements of radiation distribution on and around the cliffs, combined with the surface elevation change data. It would be interesting to see whether the depth of relatively permanent lakes remains constant over winter, or whether ice grows at the lake bottom. In addition to the effects of ice and lakes, it would be interesting to see whether stands of vegetation that grow on the debris itself add any to the mass and thus energy balance processes. Vegetation influences the temperature around it by evapotranspiration, and affects mass exchange processes by e.g. interception of rainfall. Therefore, it is not impossible that, should sufficient amounts of vegetation cover be present, glacier surface dynamics are influenced.

The contribution of the calculated melt water to total catchment runoff is likely minimal. Immerzeel et al. (2014) state that during summer, the melt water only constituted about 2% of the average runoff generated for the Lirung catchment. This is, among other reasons, due to the fact that most of the runoff during that period was likely generated by monsoonal rainfall. The contribution of Lirung Glacier melt to the Langtang Catchment runoff is about 0.2%, based on discharge measurements at the Kyanging Base station for summers between 2000 and 2006. Discharges were about 15 m^3s^{-1} during those periods (Immerzeel et al., 2010). Based on the meltwater discharge of 0.036 m^3s^{-1} by Immerzeel et al. (2014), meltwater generated during summer constituted about 0.2% of total catchment runoff. For winters during the same years, discharge at the base station averaged between 2 and 3 m^3s^{-1}. The meltwater calculated for this winter (0.016 ± 0.019 m^3s^{-1}) therefore constitutes about 0.5-0.8% of total discharge. This relative increase of meltwater contribution in winter is likely due to the greatly decreased contribution of precipitation, which is highest during the summer monsoon and falls mainly as rain.

Based on the numbers of Immerzeel et al. (2014) and those computed in this thesis, excess meltwater can be said to contribute very little to total catchment runoff. It appears that, should Lirung Glacier disappear the coming years, it would have little influence on total discharge since most of the runoff appears to be due to rainfall. Still, the exact contribution to total catchment runoff requires detailed data of precipitation, avalanches and melt, discharge measurements etc. Since melt is dependent on a multitude of factors, only a glacio-hydrological model with the right specifications would be able to determine the relative contributions of each. Continued UAV coverage before and after every monsoon period, in combination with discharge monitoring both at glacier outlet and at the Kyanging base station could prove very valuable, as knowledge and as input for these glacio-hydrological models.

7. Conclusion

The goal of this study was to:

- Examine the evolution of surface features and to quantify surface lowering, melt, mass change and surface velocity of part of the debris covered tongue of the Lirung Glacier during the winter period between October 2013 and May 2014,
- By means of the relatively novel approach using UAV acquired imagery.

The main finding is that the tongue of the Lirung glacier experienced considerably less change over winter than over summer. Even taking into account any uncertainties in the May 2014 results due to difficulties during DEM construction, the difference is very clear. The ice cliffs show far less substantial retreat rates, and average surface lowering is also considerably less during winter than summer. The likely reason for this difference is the fact that during winter the prevailing weather is determined by the dry and cold monsoon, in contrast to the precipitation rich and warm summer monsoon. Precipitation and warm temperatures promote glacier dynamics in through mass gain and mass loss processes, while decreased precipitation and lower temperatures in winter will inhibit these processes. By differencing the DEM of May 2014 with the DEM of October 2013 it was shown that the glacier has likely decreased in mass, therefore it is clear that mass wasting continues over winter. The uncertainty introduced by the DEM generation, in addition to unknown potential mass gains due to avalanching make exact quantification of surface velocity, surface elevation change, melt and mass change impossible. Therefore, the results presented here should be interpreted with care and considered as an indication for the changes that occurred over winter. A large part of the glacier tongue is not taken into account in this study, adding an even greater uncertainty to the estimation of total downwasting.

The set of images available for this study was unfortunately of insufficient quality. Too few off-glacier images were available to adequately georeference the DEM and there was insufficient overlap between images, especially at the upper part of the glacier tongue. This caused certain parts of the glacier tongue to be missing from the ortho-mosaic and DEM and likely caused the large uncertainties associated with the DEM. The only way to remedy this would be to acquire a new set of images, which was not possible. However the merits of UAV use in glaciological research are still proven. Even without a perfect set of images valuable information could be inferred from the ortho-mosaic and DEM. Further research of the Lirung using these drones can provide information about debris covered glacier dynamics at a high spatial and temporal resolution. For future research it is recommended to cover the entire glacier tongue to be able to consider its total surface and mass changes. Care should be taken that UAV images are acquired with sufficient overlap, and with glacier and off-glacier coverage. In addition it is preferable to have total control over the camera parameters, so that shutter speed, ISO and aperture can be set to fixed values and lighting is the same for each image. This will help the image processing in Agisoft PhotoScan. Shooting in raw is recommended due to its additional image modification possibilities.

If repeated UAV coverage of the glacier tongue is combined with continuous observations concerning mass gain processes (avalanches, snow, etc.) and glacier outlet discharge measurements, a greater insight in the mass exchange processes could be gained. However, these mass gain and loss processes are very difficult to observe and quantify. Avalanches are random occurrences and quantifying the amount of mass gained will be very difficult. Researching avalanches is not without danger. Therefore, the only way in which the dynamics of the Lirung Glacier can be examined is by means of a fully integrated and calibrated glacio-hydrological model, using the data gained by UAV campaigns and in-situ field measurements as input.

References

Ageta, Y. and Higuchi, K. (1984). *Estimation of mass balance components of a summer-accumulation type glacier in the Nepal Himalaya.* Geografiska Annaler. Series A, Physical Geography, 66(3), 249-255.

Agisoft (2014). PhotoScan professional 1.0 user manual. , p.p. 66 (St. Petersburg).

Armstrong, R.L. (2010). *The glaciers of the Hindu Kush-Himalayan region: A summary of the science regarding glacier melt/retreat in the Himalayan, Hindu Kush, Karakoram, Pamir, and Tien Shan mountain ranges*. Kathmandu: ICIMOD.

Bajracharya, S.R., Maharjan, S.B. and Shrestha, F. (2011). *Glaciers Shrinking in Nepal Himalaya, Climate Change.* In: Geophysical Foundations and Ecological Effects, Dr Juan Blanco (Ed.), ISBN: 978-953-307-419-1, InTech, Available from: http://www.intechopen.com/books/climate-change-geophysical-foundationsand-ecological-effects/glaciers-shrinking-in-nepal-himalaya

Bamber, J. (2006). *Remote sensing in glaciology.* In: Glacier Science and Environmental Change. Editor: Knight, P.G. Blackwell Publishing.

Bamber, J.L. and Rivera, A. (2005). *A review of remote sensing methods for glacier mass balance determination.* Global and Planetary Change, 59, 138-148.

Benn, D.I., Bolch, T., Hands, K., Gulley, J., Luckman, A., Nicholson, L.I., Quincey, D., Thompson, S., Toumi, R. and Wiseman, S. (2012). *Response of debris-covered glaciers in the Mount Everest region to recent warming, and implications for outburst flood hazards.* Earth-Science Reviews, 114, 156-174

Benn, D.I. and Lehmkuhl, F. (2000). *Mass balance and equilibrium-line altitudes of glaciers in high-mountain environments.* Quaternary International, 65/66, 15-29.

Benn, D.I., Wiseman, S. and Hands, K.A. (2001). *Growth and drainage of supra-glacial lakes on debris-mantled Ngozumpa Glacier, Khumbu Himal, Nepal.* Journal of Glaciology, 47(159), 626-638.

Bolch, T., Buchroithner, M.F., Peters, J., Baessler, M. and Bajracharya, S. (2008a). *Identification of glacier motion and potentially dangerous glacial lakes in the Mt. Everest region/Nepal using spaceborne imagery.* Natural Hazards and Earth System Sciences, 8, 1329-1340.

Bolch, T., Buchroithner, M., Pieczonka, T. and Kunert, A. (2008b). *Planimetric and volumetric glacier changes in the Khumbu Himal, Nepal, since 1962 using Corona, Landsat TM and ASTER data.* Journal of Glaciology, 54(187), 592-600.

Bolch, T., Kulkarni, A., Kääb, A., Huggel, C., Paul, F., Cogley, J.G., Frey, H., Kargel, J. S., Fujita, K., Scheel, M., Bajracharya, S., and Stoffel, M. (2012). *The State and Fate of Himalayan Glaciers*. Science, 336, 310–314.

Bolch, T., Pieczonka, T. and Benn, D.I. (2011). *Multi-decadal mass loss of glaciers in the Everest area (Nepal Himalaya) derived from stereo imagery.* The Cryosphere, 5, 349-358.

Brock, B. W., C. Mihalcea, M. P. Kirkbride, G. Diolaiuti, M. E. J. Cutler, and C. Smiraglia (2010). *Meteorology and surface energy fluxes in the 2005–2007 ablation seasons at the Miage debris-*

covered glacier, Mont Blanc Massif, Italian Alps, Journal of Geophysical Research, 115, D09106, doi:10.1029/2009JD013224.

Brown, M.E., Ouyang, H., Habib, S, Shrestha, B., Shrestha, M., Panday, P., Tzortziou, M., Policelli, F., Artan, G., Giriraj., A, Bajracharya, S.R. and Racoviteanu, A. (2010). *HIMALA: Climate impacts on glaciers, snow, and hydrology in the Himalayan region.* Mountain Research and Development, 30, 4, 401-404.

Cogley, J.G. (2011). *Present and future states of Himalaya and Karakoram glaciers.* Annals of Glaciology, 54(59), 69-73..

Cuffey, K. M. and Paterson, W. S. (2010). *The physics of glaciers* (4th ed.). Oxford: Butterworth-Heinemann.

Environmental Systems Research Institute (ESRI), Inc., (2013). ArcGIS for Desktop. Version 10.2.1.

Fonstad, M.A., Dietrich, J.T., Courville, B.C., Jensen, J.L. and Carbonneau, P.E. (2013). *Topographic structure from motion: a new development in photogrammetric measurement.* Earth Surface Processes and Landforms, 38, 421-430.

Fujita, K. and Nuimura, T. (2011). *Spatially heterogeneous wastage of Himalayan glaciers.* Proceedings of the National Academy of Sciences of the United States of America, 108(34), 14011-14014.

Fujita, K., Suzuki, R., Nuimura, T. and Sakai, A. (2008). *Performance of ASTER and SRTM DEMs, and their potential for assessing glacial lakes in the Lunana region, Bhutan Himalaya.* Journal of Glaciology, 24(185), 220-228.

Furukawa, Y. and Ponce, J. (2009). *Accurate camera calibration from Multi-View Stereo and Bundle Adjustment.* International Journal of Computer Vision, 84, 257-268.

Gardelle, J., Berthier, E. and Arnaud, Y. (2012). *Slight mass gain of Karakoram glaciers in the early 21st century*. Nature Geoscience, 5, 322–325.

Gardelle, J., Berthier, E., Arnaud, Y., and Kääb, A. (2013). *Region-wide glacier mass balances over the Pamir-Karakoram-Himalaya during 1999–2011.* The Cryosphere Discussions, 7, 975–1028, doi:10.5194/tcd-7-975-2013.

Gardner, A.S., Moholdt, G., Cogley, J.G., Wouters, B., Arendt, A.A., Wahr, .J, Berthier, E., Hock, R., Pfeffer, W.T., Kaser, G., Ligtenberg, S.R.M., Bolch, T., Sharp, M.J., Hagen, J.O., van den Broeke, M. and Paul, F. (2013). *A reconciled estimate of glacier contributions to sea level rise: 2003 to 2009.* Science, 340, 852-857.

Hagg, W., Mayer, C., Lambrecht, A. and Helm, A. (2008). *Sub-debris melt rates on southern Inylchek Glacier, central Tian Shan*. Geografiska Annaler. 90 A(1), 55–63.

Han, H., Wang, J., Wei, J. and Liu, S. (2010). *Backwasting rate on debris-covered Koxkar glacier, Tuomuer mountain, China.* Journal of Glaciology, 56(196), 287-296.

Hock, R. (2005). *Glacier melt: a review of processes and their modeling.* Progress in Physical Geograpy, 29 (3), 362-391

Hooke, R., LeB. (2005). *Principles of glacier mechanics (2nd ed.).* Cambridge: Cambridge University Press.

Immerzeel., W.W., van Beek, L.P.H and Bierkens, M.F.P. (2010). *Climate change will affect the Asian water towers.* Science, 328, 1382-1385.

Immerzeel. W.W., van Beek, L.P.H., Konz, M., Shrestha, A.B. and Bierkens, M.F.P. (2012). *Hydrological response to climate change in a glacierized catchment in the Himalayas.* Climatic Change, 110, 721-736.

Immerzeel, W.W., Kraaijenbrink, P.D.A., Shea, J.M., Shrestha, A.B., Pellicciotti, F., Bierkens, M.F.P and De Jong, S. M. (2014). *High-resolution monitoring of Himalayan glacier dynamics using unmanned aerial vehicles.* Remote Sensing of Environment, 150, 93-103

IPCC (2007). *Climate Change (2007) The Physical Science Basis: Contribution of Working Group 1 (The Physical Science Basis) to the Fourth Assessment Report of the Intergovernmental Panel on Climate Change.* (edited by S. Solomon, D. Qin, M. Manning, Z. Chen, M.C. Marquis, K. Averyt, M. Tignor, and H.L. Miller),Intergovernmental Panel on Climate Change, Cambridge University Press, Cambridge, U.K.

Juen, M., Mayer, C., Lambrecht, A., Haidong, H., and Shiyin, L. (2013). *Impact of varying debris cover thickness on catchment scale ablation: A case study for Koxkar glacier in the Tien Shan*. The Cryosphere Discussions, 7(6), 5307–533.

Kääb, A. (2005). *Combination of SRTM3 and repeat ASTER data for deriving alpine glacier flow velocities in the Bhutan Himalaya.* Remote Sensing of Environment, 94, 463-474.

Kääb, A. et al., (2014). *Glacier mapping and monitoring using multispectral data.* In: *Global Land Ice Measurements from Space*. J. S. Kargel et al. (eds.) Springer Praxis Books, DOI: 10.1007/978-3-540-79818-7_1, Springer-Verlag Berlin Heidelberg 2014.

Kääb, A., Berthier, E., Nuth, C., Gardelle, J., and Arnaud, Y. (2012). *Contrasting patterns of early twenty-first-century glacier mass change in the Himalayas.* Nature, 488(7412), 495–498.

Kayastha, R. B., Takeuchi, Y., Nakawo, M. and Ageta, Y. (2000). *Practical prediction of ice melting beneath various thickness of debris cover on Khumbu Glacier, Nepal, using a positive degree-day factor. Debris-Covered Glaciers (Proceedings of a workshop held at Seattle, Washington, USA, September 2000). IAHS Publ. no. 264, 2000.*

Lillesand., M., Kiefer, R. and Chipman, J. (2008). *Remote Sensing and Image Interpretation. 6th edition. John Wiley & Sons, Inc.*

Lucieer, A., De Jong, S. M., and Turner, D. (2013). *Mapping landslide displacements using Structure from Motion (SfM) and image correlation of multi-temporal UAV photography*. Progress in Physical Geography, 38(1), 97–116.

Lutz, A.F., Immerzeel, W.W., Gobiet, A., Pellicciotti, F. and Bierkens, M.F.P. (2012). *New climate change scenarios reveal uncertain future for Central Asian glaciers.* Hydrology and Earth System Science Discussions, 9, 12961-12727.

Marshak, S. (2008). *Earth; Portrait of a planet (3rd ed) International student edition.* New York: W.W. Norton & Company, Inc.

Mihalcea, C., Mayer, C., Diolaiuti, G., Lambrecht, A., Smiraglia, C. and Tartari, G. (2006). *Ice ablation and meteorological conditions on the debris-covered area of Baltoro glacier, Karakoram, Pakistan.* Annals of Geology, 43, 292-300.

Naito, N., Nakawo, M., Aoki, T., Asahi, K., Fujita, K., Sakai, A., Kadota, T., Shiraiwa, T. and Seko, K. (1998). *Surface flow on the ablation area of the Lirung Glacier in Langtang Valley, Nepal Himalayas.* Bulletin of Glacier Research, 16, 67-73.

Nakawo, M. and Rana, B. (1999). *Estimate of ablation rate of glacier ice under a supra-glacial debris layer.* Geografiska Annaler, 81A(4), 695-701.

Nuimura, T., Fujita, K., Yamaguchi, S. and Sharma, R.R. (2012). *Elevation changes of glaciers revealed by multitemporal digital elevation models calibrated by GPS survey in the Khumbu region, Nepal Himalaya, 1992*-2008. Journal of Glaciology, 58(210), 648-656.

Östrem, G. (1959). *Ice melting under a thin layer of moraine, and the existence of ice cores in moraine ridges.* Geografiska Annaler, 41(4), 228–230.

Plets., G, Gheyle, W., Verhoeven, G., De Reu, J., Bourgeois, J., Verhegge, J. and Stichelbaut, B. (2012). *Three-dimensional recording of archeological remains in the Altai Mountains.* Antiquity, 86, 884-897.

Quincey, D.J., Copland, L., Mayer, C., Bishop, M., Luckman, A. and Belò, M. (2009a). *Ice velocity and climate variations for Baltoro Glacier, Pakistan.* Journal of Glaciology, 55(194), 1061-1071.

Quincey, D.J., Luckman, A. and Benn, D. (2009b). *Quantification of Everest region glacier velocities between 1992 and 2002, using satellite interferometry and feature tracking.* Journal of Glaciology, 44(192), 596-606.

Quincey, D.J. et al. (2014). *Digital terrain modeling and glacier topographic characterization.* In: *Global Land Ice Measurements from Space*. J. S. Kargel et al. (eds.) Springer Praxis Books, DOI: 10.1007/978-3-540-79818-7_1, Springer-Verlag Berlin Heidelberg 2014.

Racoviteanu, A.E., Paul, F., Raup, B., Khalsa, S.J.S. and Armstrong, R. (2009). *Challenges and recommendations in mapping of glacier parameters from space: result of the 2008 Global Land Ice Measurement from Space (GLIMS) workshop, Boulder, Colorado, USA.* Annals of Glaciology, 50(53), 53-69.

Racoviteanu, A.E., Williams, W.M. and Barry, R.G. (2008). *Optical remote sensing of glacier characteristics: a review with focus on the Himalaya*. Sensors, 8, 3355–3383.

Rana, B., Nakawo, M., Ageta, Y. and Seko, K. (1996). *Glacier ablation under debris cover: field observations on Lirung Glacier, Nepal Himalayas*. In: Proceedings of International Conference on

Ecohydrology of High Mountain Areas (24-28 March, Kathmandu), 393-403. International Centre for Integrated Mountain Development, Kathmandu, Nepal.

Reid, T. and Brock, B.W. (2010). *An energy-balance model for debris-covered glaciers including heat conduction through the debris layer.* Journal of Glaciology 56(199), 903–916.

Reid, T. and Brock, B.W. (2014). *Assessing ice-cliff backwasting and its contribution to total ablation of debris-covered Miage glacier, Mont Blanc massif, Italy.* Journal of Glaciology, 60(219), 3-13.

Reid, T. D., Carenzo, M., Pellicciotti, F. and Brock, B.W. (2012). *Including debris cover effects in a distributed model of glacier ablation.* Journal of Geophysical Research, 117, D18105

Reynolds, J.M. (2000). *On the formation of supra-glacial lakes on debris-covered glaciers*. In: Nakawo, N., Fountain, A., Raymond, C. (Eds.), Debris-covered Glaciers: IAHS Publications, 264, 153–161.

Reznichenko, N., Davies, T., Shulmeister, J. and McSaveney, M.J. (2010). *Effects of debris on ice-surface melting rates: an experimental study.* Journal of Glaciology, 56(197), 384–39.

Röhl, K. (2008). *Characteristics and evolution of supra-glacial ponds on debris-covered Tasman Glacier, New Zealand.* Journal of Glaciology, 54(188), 867–880.

Ryan, J.C., Hubbard, A.L., Box, J.E., Todd, J., Christoffersen, P., Carr, J.R., Holt, T.O. and Snooke, N. (2015). *UAV photogrammetry and structure from motion to assess calving dynamics at Store Glacier, a large outlet draining the Greenland ice sheet.* The Cryosphere, 9, 1-11.

Sakai, A., and Fujita, K. (2010). *Formation conditions of supra-glacial lakes on debris-covered glaciers in the Himalaya.* Journal of Glaciology, 56(195), 177–181.

Sakai, A., Fujita, K. and Kubota, J. (2004). *Evaporation and percolation effect on melting at debris-covered Lirung Glacier, Nepal Himalayas*. Bulletin of Glaciological Research, 21, 9–16.

Sakai, A., Nakawo, M., & Fujita, K. (1998).*Melt rate of ice cliffs on the Lirung Glacier, Nepal Himalayas, 1996*. Bulletin of Glacier Research, 16, 57–66.

Sakai, A., Nakawo, M., and Fujita, K. (2002). *Distribution characteristics and energy balance of ice cliffs on debris-covered glaciers, Nepal Himalaya*. Arctic, Antarctic, and Alpine Research, 1, 12–19.

Sakai, A., Nishimura, K., Kadota, T., and Takeuchi, N. (2009). *Onset of calving at supra-glacial lakes on debris-covered glaciers of the Nepal Himalaya*. Journal of Glaciology, 55(193), 909–917.

Sakai, A., Takeuchi, N., Fujita, K., and Nakawo, M. (2000). *Role of supra-glacial ponds in the ablation process of a debris-covered glacier in the Nepal Himalayas. Debris-Covered Glaciers (Proceedings of a workshop held at Seattle, Washington, USA, September 2000). IAHS Publ. no. 264, 2000.*

Schaner, N., Voisin, N., Nijssen, B. and Lettenmaier, D.P. (2012). *The contribution of glacier melt to streamflow.* Environmental Research Letters, 7 (034029), 1-8.

Scherler, D., Bookhagen, B. and Streckter, M.R. (2011). *Spatially variable response of Himalayan glaciers to climate change affected by debris cover.* Nature Geoscience, 4, 156-459.

Shea, J.M., Immerzeel, W.W., Wagnon, P., Vincent, C. and Bajracharya, S. (2013). *Assessing glacier sensitivity to climate perturbations in the Everest region by integrating observations and high resolution modeling.* Journal of Geophysical Research, *Submitted.*

Shrestha, A.B. and Aryal, R. (2011). *Climate change in Nepal and its impact on Himalayan glaciers.* Regional Environmental Change, 11 (suppl 1), S65-S77. doi:10.1007/s10113-010-0174-9.

Singh, P. and Singh, V.P (2011). *Snow and glacier hydrology.* Dordrecht: Kluwer Academic Publishers.

Singh, V.P., Singh, P. and Haritashya, U.K. (eds.). (2011). *Encyclopedia of Snow, Ice and Glaciers.* Springer Science+Business Media B.V.

Suzuki, R., Fujita, K. and Ageta, Y. (2007). *Spatial distribution of thermal properties on debris-covered glaciers in the Himalayas derived from ASTER data.* Bulletin of Glaciological Research, 24, 13-22.

Tangborn, W. and Rana, B. (2000). *Mass balance and runoff of the partially debris-covered Langtang Glacier, Nepal. Debris-Covered Glaciers (Proceedings of a workshop held at Seattle, Washington, USA, September 2000). IAHS Publ. no. 264, 2000.*

Topcon Positioning Systems (2009). *Topcon tools post-processing software reference manual.* , 606 (Livermore).

Triggs, B., McLauchlan, P.F., Hartley, R.I. and Fitzgibbon, A.W. (2000). *Bundle Adjustment – a modern synthesis.* In: Vision Algorithms: Theory and Practice. *Springer-Verlag. Berlin-Germany*

Van der Veen, C.J. (2013). *Fundamentals of Glacier Dynamics* (2nd ed.), Bosa Roca: Taylor and Francies Inc.

Verhoeven, G. (2011). *Software review taking computer vision aloft — archaeological three-dimensional reconstructions from aerial photographs with PhotoScan*. Archaeological Prospection, 73(18), 67–73.

Vincent, C., Ramanathan A., Wagnon, P., Dobhal, D. P., Linda, A., Berthier, E., Sharma, P., Arnaud, Y., Azam, M.F., Jose, P.G., and Gardelle, J. (2012). *Mass gain of glaciers in Lahaul and Spiti region (North India) during the nineties revealed by in-situ and satellite geodetic measurements*. The Cryosphere Discussions, 6, 3733–3755, doi:10.5194/tcd-6-3733-2012.

Wagnon, P., Vincent, C., Arnaud, Y., Berthier, E., Vuillermoz, E., Gruber, S., Ménégoz, M., Gilbert, A., Dumont, M., Shea, J.M., Stumm, D., and Pokhrel, B. K. (2013). *Seasonal and annual mass balances of Mera and Pokalde glaciers (Nepal Himalaya) since 2007.* The Cryosphere, 7, 1769-1786.

Whitehead, K., Moorman, B.J. and Hugenholtz, C.H. (2013). *Brief communication: Low-cost, on-demand aerial photogrammetry for glaciological measurement.* The Cryosphere, 7, 1879-1884.

Yao, T., Pu, J. and Liu, S. (2006). *Changing glaciers in High Asia.* In: Glacier Science and Environmental Change. Editor: Knight, P.G. Blackwell Publishing.

Zemp, M. et al. (2013). *Introduction: Global glacier monitoring – a long-term task integrating in situ observations and remote sensing.* In: *Global Land Ice Measurements from Space*. J. S. Kargel et al.

(eds.) Springer Praxis Books, DOI: 10.1007/978-3-540-79818-7_1, Springer-Verlag Berlin Heidelberg 2014.

http://ffden-2.phys.uaf.edu/211_fall2002.web.dir/Ryan_Cross/Ryancross.dir/Glacial%20flow.JPG

http://www.csa.com/discoveryguides/icecore/review.php

http://www.staff.science.uu.nl/~oerle102/site_Mort/menu_4.html\

http://www.swisseduc.ch/glaciers/glossary/supra-glacial-debris-en.html

http://support.esri.com/en/knowledgebase/Gisdictionary/

www.nikonusa.com

http://theuavguy.wordpress.com/

https://support.pix4d.com/hc/en-us/articles/202559369-Reprojection-Error

European Space Agency (ESA) Glossary. https://earth.esa.int/handbooks/asar/CNTR5-2.htm

Agisoft LLC. www.agisoft.com

Appendix

Figures

A: May 2014 ortho-mosaic of the complete scene, 10 cm resolution. The observed area of the glacier tongue is outlined in black.

B: May 2014 Digital Elevation Model, 20 cm resolution. The observed area of the glacier tongue is outlined in black.

C: Studied subset of the Lirung Glacier: May 2014 ortho-mosaic (10 cm). Rectangles denote ice cliffs, circles denote supra-glacial lakes.

D: Studied subset of the Lirung Glacier: May 2014 DEM (20 cm).

E: Surface velocity and direction over the period between October 2013 and May 2014. Arrow length indicates relative velocity

F: Difference DEM between May 2014 and October 2013.

G: Difference DEM between May 2014 and October 2013 showing only regions of surface rise or decrease within 1 m. Black areas denote >1m elevation decrease.

H: Difference DEM between May 2013 and October 2013 *(Adapted from: Immerzeel et al., 2014*)

I: Difference DEM between October 2013 and May 2013 showing only regions of surface rise or decrease within 1 m *Adapted from Immerzeel et al., 2014).*

J: Difference DEM between October 2013 and May 2013 showing only regions of surface rise or decrease between -1.75m and 1.25 m *(Adapted from: Immerzeel et al. (2014)*

K: Winter difference DEM of entire glacier. Outline of sub-debris ice is outlined in black.

A

B

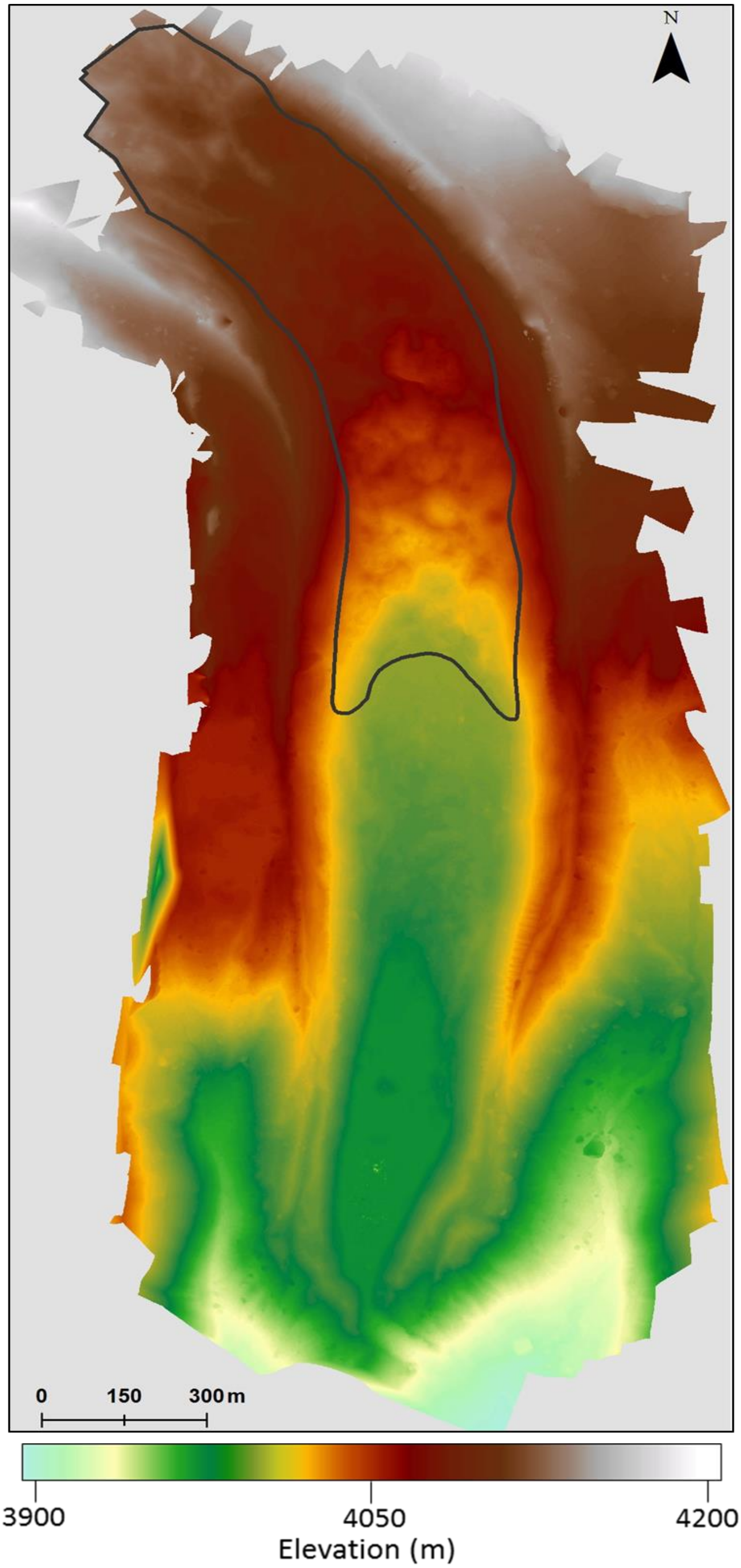

C

D

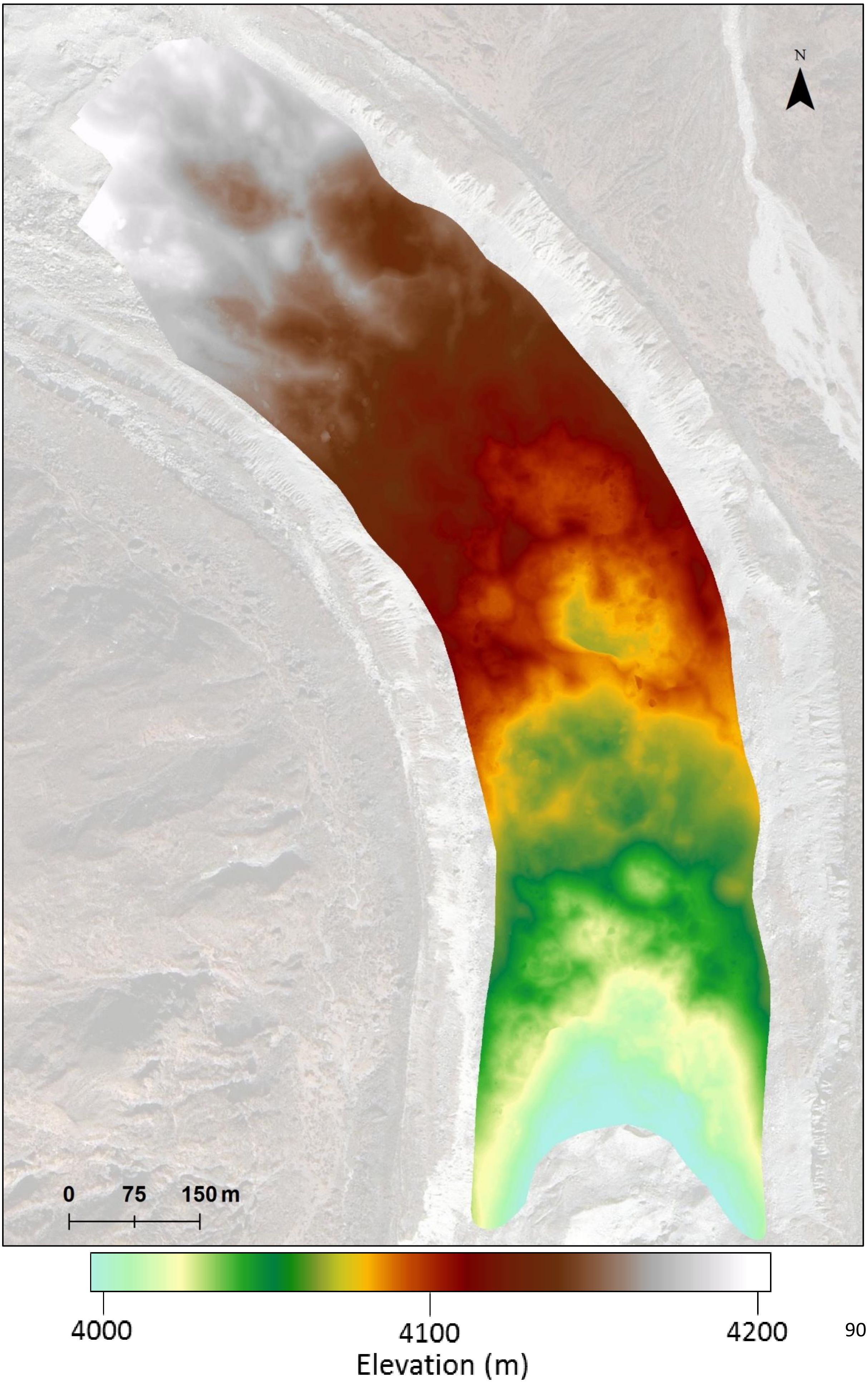

E

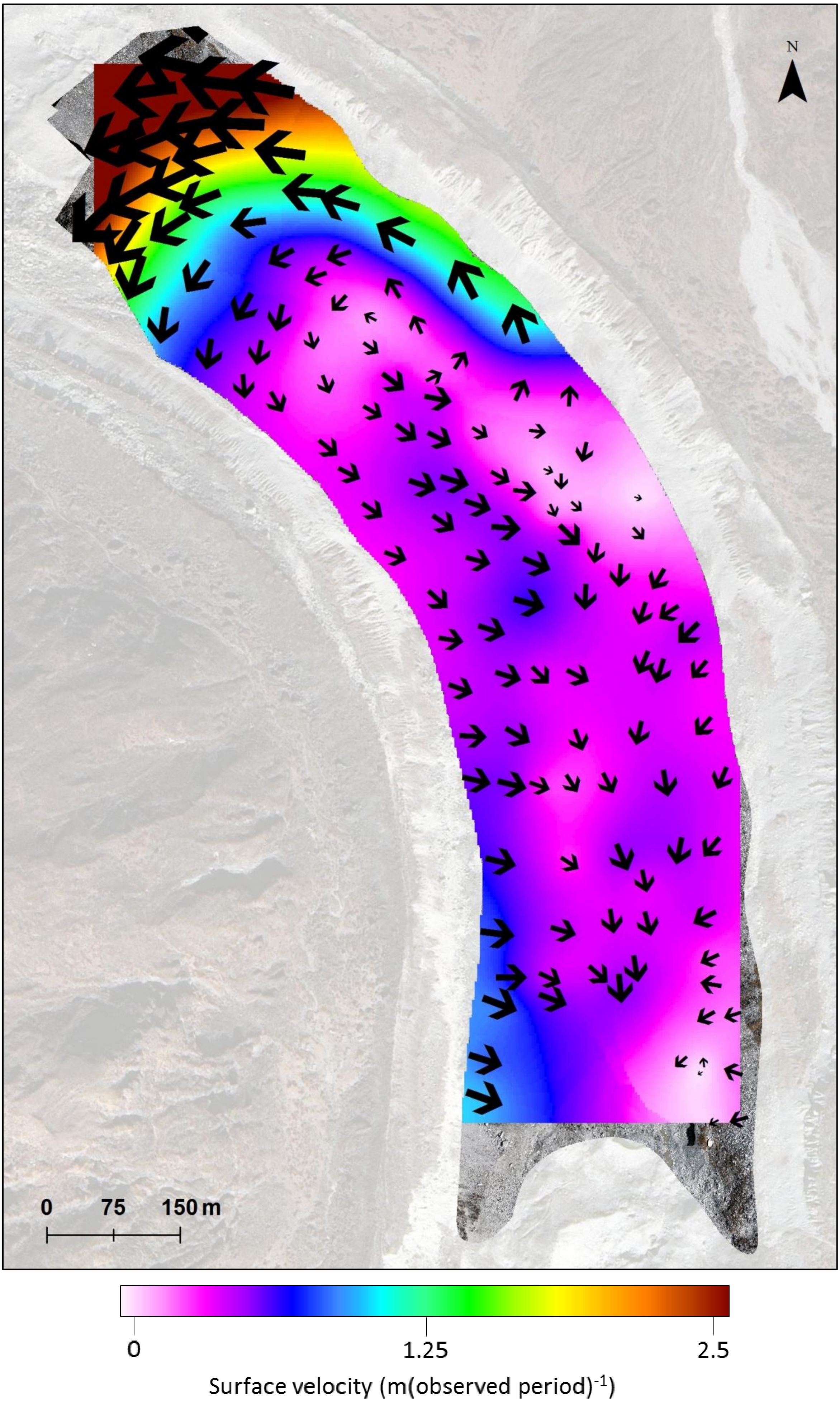

F

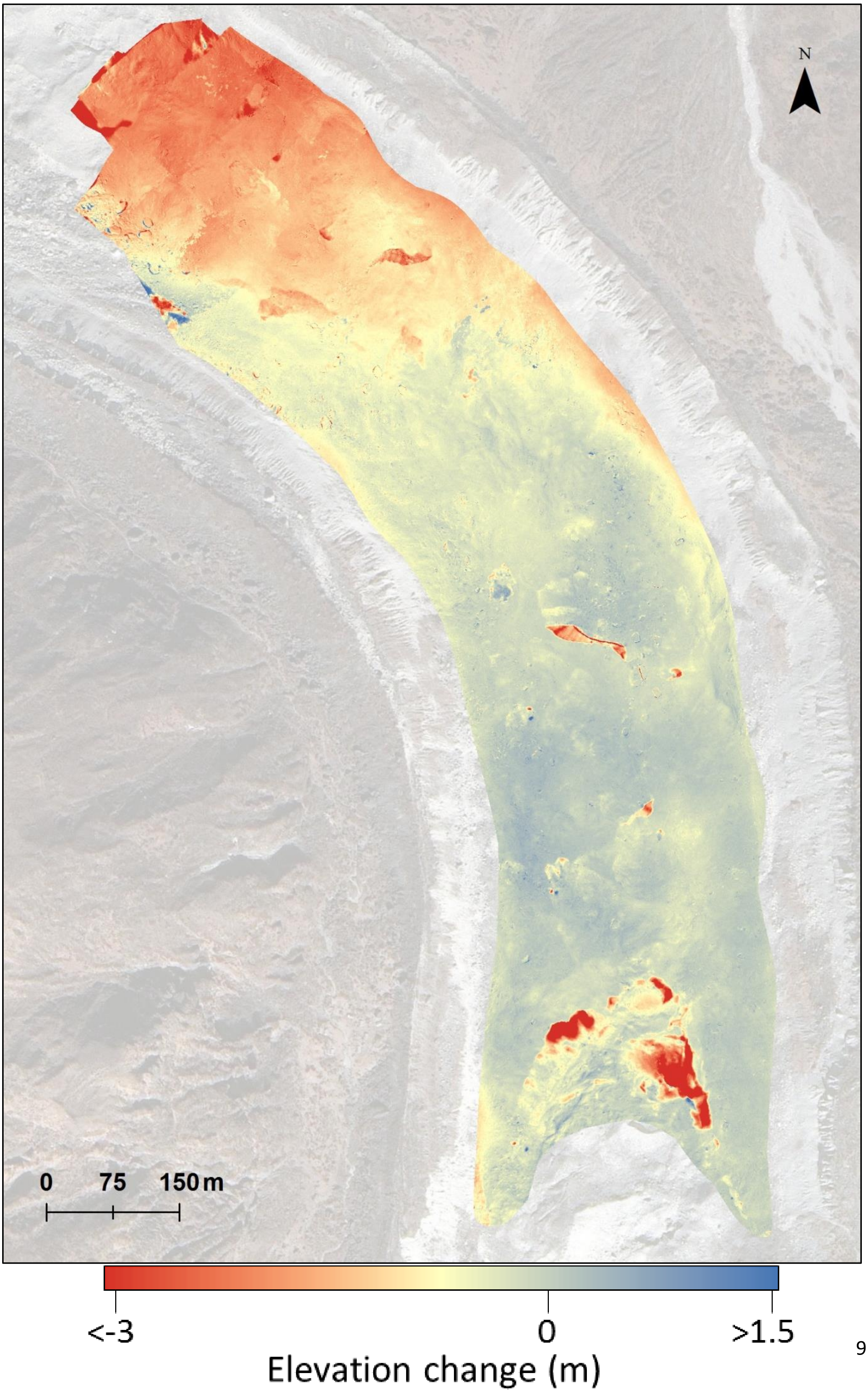

G

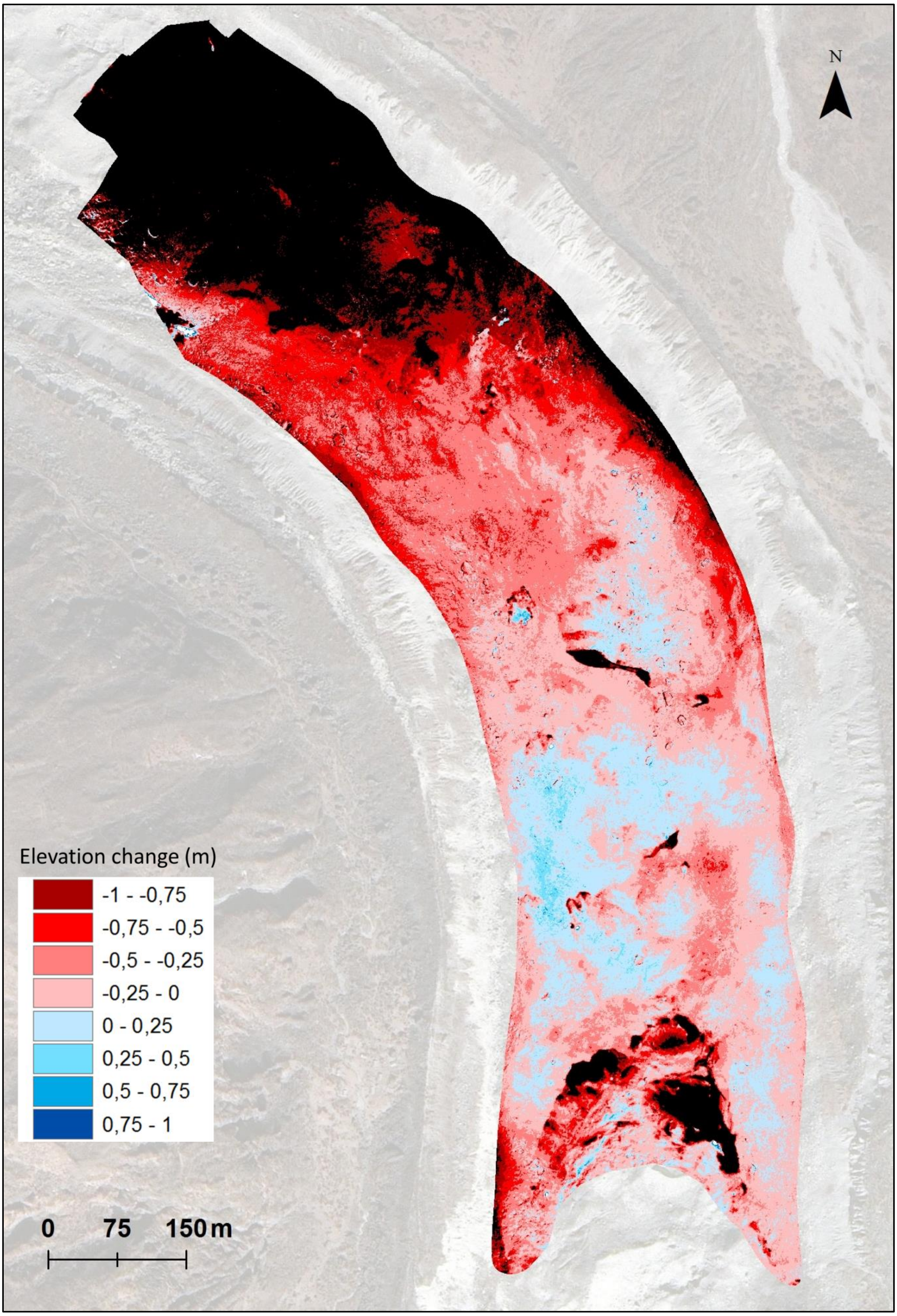
N
Elevation change (m)
-1 - -0,75
-0,75 - -0,5
-0,5 - -0,25
-0,25 - 0
0 - 0,25
0,25 - 0,5
0,5 - 0,75
0,75 - 1
0 75 150 m

H

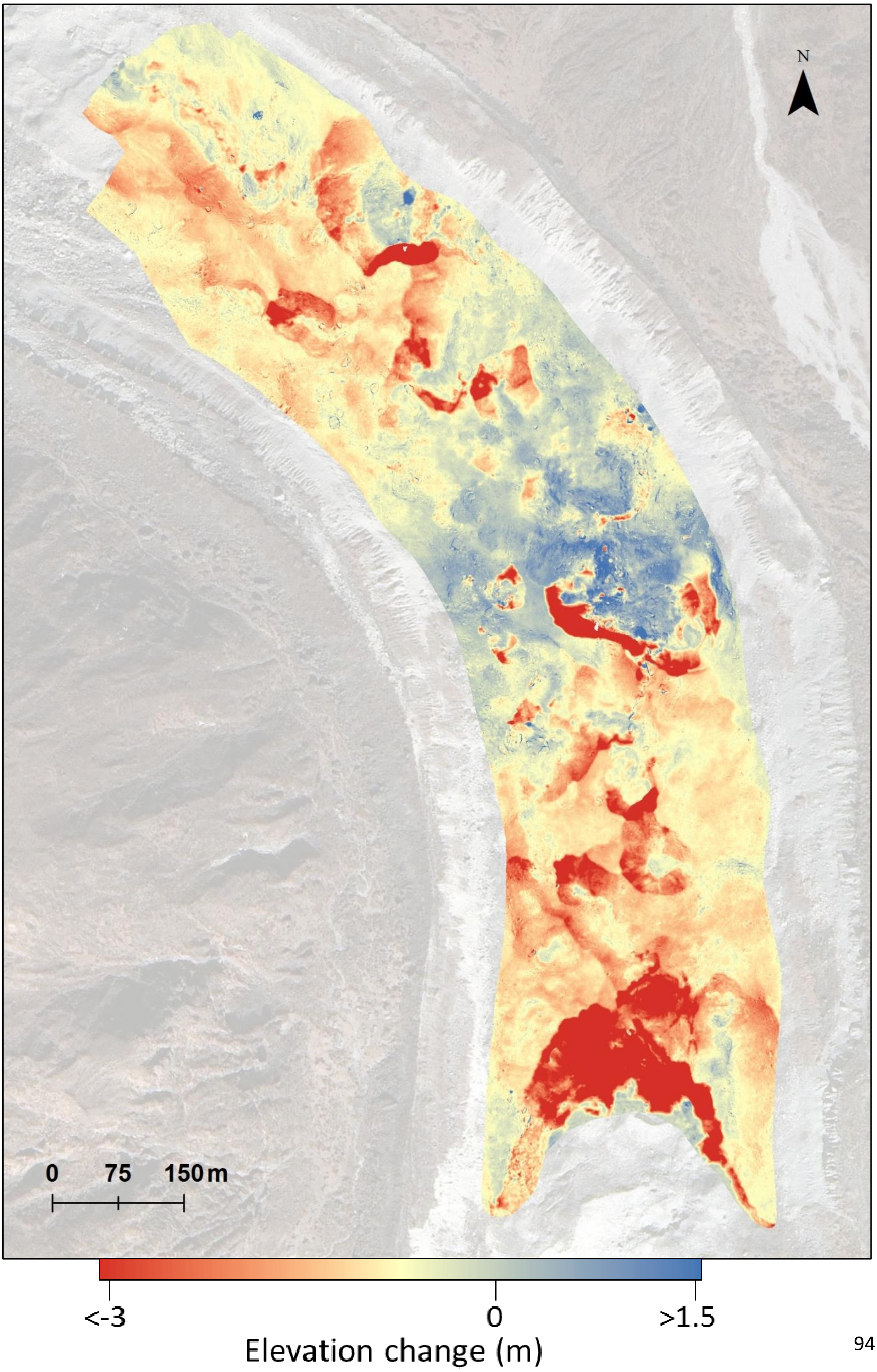

I

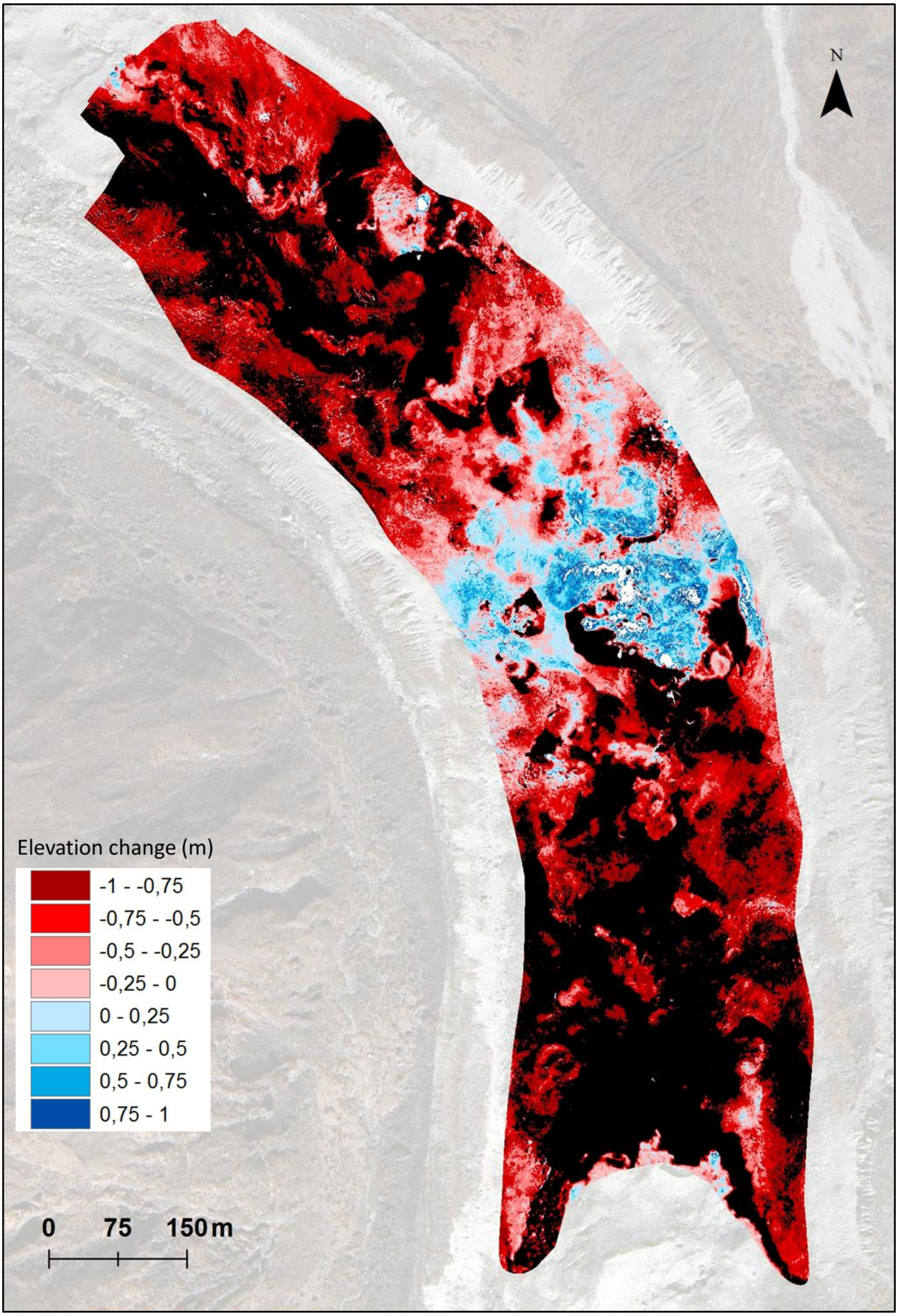
N
Elevation change (m)
-1 - -0,75
-0,75 - -0,5
-0,5 - -0,25
-0,25 - 0
0 - 0,25
0,25 - 0,5
0,5 - 0,75
0,75 - 1
0
75
150 m

J

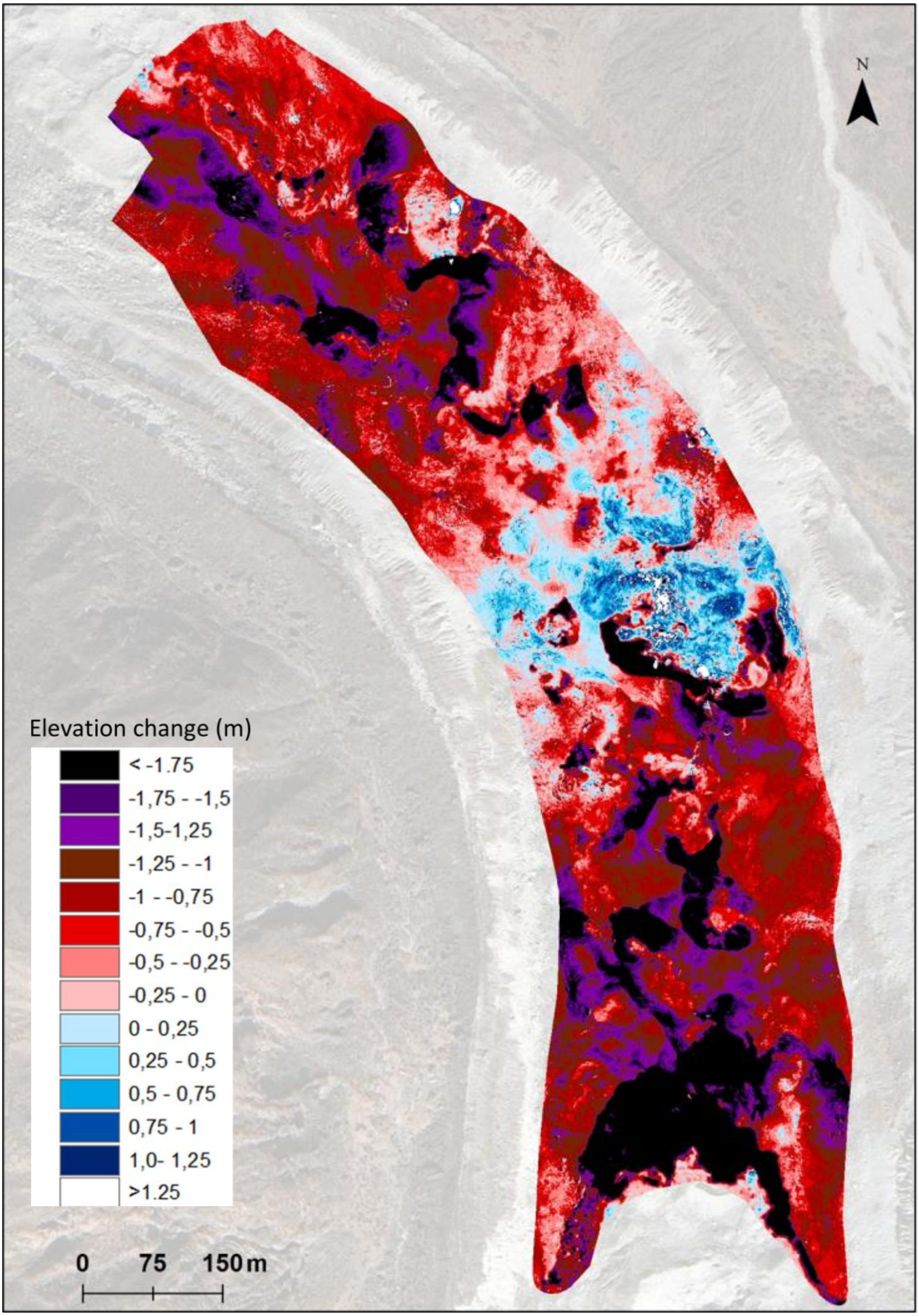

N
Elevation change (m)
< -1.75
-1,75 - -1,5
-1,5-1,25
-1,25 - -1
-1 - -0,75
-0,75 - -0,5
-0,5 - -0,25
-0,25 - 0
0 - 0,25
0,25 - 0,5
0,5 - 0,75
0,75 - 1
1,0- 1,25
>1.25
0 75 150 m

K